ARPA ORDER NO. 3363

REPORT NO. 80-1

# DEVELOPMENT OF A TABLETOP MODEL FOR THE GENERATION OF AMORPHOUS/MICROCRYSTALLINE METAL POWDERS

INTERIM TECHNICAL REPORT
TO
OFFICE OF NAVAL RESEARCH
CONTRACT NO. N00014-77-C-0373

JULY 1980

Principal Investigator:
John F. Mahoney
(213) 357-3201



Phrasor Scientific, Inc.
1536 HIGHLAND AVENUE
DUARTE, CALIFORNIA 91010
(213) 357-3201

UNCLASSIFIED

SECURITY CLASSIFICATION OF THIS PAGE (When Data Entered)

## REPORT DOCUMENTATION PAGE

READ INSTRUCTIONS BEFORE COMPLETING FORM

1. REPORT NUMBER: ONR-N00014-77-C-0373

2. GOVT ACCESSION NO.: AD-A093645

3. RECIPIENT'S CATALOG NUMBER:

4. TITLE (and Subtitle): DEVELOPMENT OF A TABLETOP MODEL FOR THE GENERATION OF AMORPHOUS/MICROCRYSTALLINE METAL POWDERS

5. TYPE OF REPORT & PERIOD COVERED: Interim Technical rept. 01 May 1978 - 30 April 1980

6. PERFORMING ORG. REPORT NUMBER: 80-1

7. AUTHOR(s): John F. Mahoney, Julius Perel, Zef Shanfield, Bernard E. Kalensher

8. CONTRACT OR GRANT NUMBER(s): N00014-77-C-0373, ARPA Order-3365

9. PERFORMING ORGANIZATION NAME AND ADDRESS:
Phrasor Scientific, Inc.
1536 Highland Avenue
Duarte, California 91010

10. PROGRAM ELEMENT, PROJECT, TASK AREA & WORK UNIT NUMBERS:

11. CONTROLLING OFFICE NAME AND ADDRESS:
Procuring Contracting Officer
Office of Naval Research/Dept. of the Navy
800 Quincy St., Arlington, Virginia 22217

12. REPORT DATE: 30 April 1980

13. NUMBER OF PAGES: 167

14. MONITORING AGENCY NAME & ADDRESS (if different from Controlling Office):
DCASMA Van Nuys-Pasadena Office
3452 East Foothill Blvd.
Pasadena, CA 91107

15. SECURITY CLASS. (of this report): Unclassified

15a. DECLASSIFICATION/DOWNGRADING SCHEDULE:

16. DISTRIBUTION STATEMENT (of this Report)

Reproduction of this report in whole or in part is permitted for any purpose of the United States Government.

DISTRIBUTION STATEMENT A
Approved for public release;
Distribution Unlimited

17. DISTRIBUTION STATEMENT (of the abstract entered in Block 20, if different

18. SUPPLEMENTARY NOTES

19. KEY WORDS (Continue on reverse side if necessary and identify by block number)

Electrohydrodynamics
Amorphous Alloys
Deposition
Rapid Solidification
Microcrystals
Powder Metallurgy
Microspheres
Splat Cooling
Rapid Cooling Rates

20. ABSTRACT (Continue on reverse side if necessary and identify by block number)

Electrohydrodynamics (EHD) has been explored for the generation and control of charged liquid droplets in order to produce micro-size particles and splat coatings. The aim of this work is the development of a Tabletop Powder Generator capable of controlled production of powder sizes that are both smaller and more narrowly distributed than those produced by conventional atomizers. This tool is being designed for use in fundamental studies of the effect of solidification variables on microstructures and the development of new alloy compositions attainable through rapid solidification processing. The EHD technique requires

DD FORM 1 JAN 73 1473 EDITION OF 1 NOV 65 IS OBSOLETE



UNCLASSIFIED

SECURITY CLASSIFICATION OF THIS PAGE (When Data Entered)

395527

the use of intense electric fields to generate liquid droplets directly from the liquid state. This is achieved by delivering a molten alloy to the tip of a fine capillary nozzle to which high voltage is applied. A variety of droplet source configurations and materials were explored on this program. Resistance heater technology was improved resulting in greater reliability and temperatures of 1800K were achieved while experiencing minimal erosion. Several modes of source operation were encountered depending upon the interaction of the molten metals with source materials. Rapid solidification and cooling rates of beam droplets in a vacuum environment have been analyzed from novel points of view. Powders smaller than 0.01 micron have been produced with calculated cooling rates of approximately $10^7$ K/s from radiation cooling alone. Several aluminum alloys were sprayed and produced small single spherical crystals, bicrystals, and adherent coatings. Amorphous powders and coatings (due to splat cooling) were formed using a Fe-Ni-B-P metallic glass alloy. Thin films were produced by EHD deposition of Si and Ge semiconductor materials. An Engineering Model is under development toward simplifying the operation of an EHD source using automation and modern computer techniques. Results of these studies will be used to design, construct, and deliver Tabletop Powder Generators for use as a research instrument for experimentation with fine powders, single and multiple crystal powders, amorphous powders, and the production of coatings and thin films, involving rapid solidification. During the course of these investigations, an innovative concept for the purification of thin sheets of materials was examined. The method involves the extraction of impurity elements in the form of ions which diffuse to the surface of liquid or high temperature solid sheets by application of electrostatic fields.

## FOREWORD

The information presented in this report was generated under ARPA Order Number 3363 and ONR Contract Number N00014-77-C-0373. The work was performed by Phrasor Scientific, Inc., Duarte, California.

This program was initiated under the direction of Dr. Edward C. van Reuth, Materials Science, Defense Advanced Research Projects Agency, and the Scientific Officer is Dr. Bruce A. MacDonald, Materials Science Division, Office of Naval Research, Arlington, Virginia.

The principal investigator for the program was Mr. John F. Mahoney (213) 357-3201 of Phrasor Scientific, 1536 Highland Avenue, Duarte, California 91010. Work on the program was also performed by Dr. Julius Perel, Dr. Zef Shanfield, Dr. Bernard E. Kalensher, Mr. J. Robert Otto, and Mr. Paul Pauls. In addition, consultation assistance was obtained from Professor Pol Duwez, Dr. Robert Mehrabian, and Dr. Carlos Levi.

CONTENTS

CONTENTS (contd)

ILLUSTRATIONS

ILLUSTRATIONS (contd)

ILLUSTRATIONS (contd)

ILLUSTRATIONS (contd)

# SECTION 1

# INTRODUCTION AND SUMMARY

## Objective

The aim of the present program is to develop a Tabletop Powder Generator capable of producing a wide range of powders and coatings in laboratory quantities for use by material scientists. Electrohydrodynamics (EHD), the technique used to generate liquid droplets, is under exploration as a viable metallurgical research tool, particularly for the investigation of rapid solidification. A wide range of alloy compositions, semiconductors, and even ceramic powders and coatings can be produced using EHD in order to investigate fundamental properties and perform applied studies of materials. The EHD process is continuous and allows for radiative and splat cooling studies by conductive heat transfer.

The initial aim of this program was motivated by the possibilities of new material structures and compositions producible by rapid solidification processing. Amorphous powders and new crystalline structures were originally anticipated and have been produced by EHD. Much more work in metallurgy is required to increase our understanding of the interrelationship between various process variables involved in rapid solidification. These variables, such as alloy composition, cooling rate, microstructure, etc., can only be obtained through careful experimentation and imaginative theoretical considerations. The Tabletop Powder Generator is potentially able to provide the controlled reproducible scientific experimentation affordable in a relatively small research laboratory. EHD opens new areas of investigation and could play a major role in studies of the rapid solidification of a wide variety of alloy compositions under controlled conditions with reproducible cooling rates. It could permit the production of fine droplets of both low and

high temperature alloys which are solidified in flight or on various substrates. It could become an important instrument for fundamental and applied studies of rapid solidification and segregation phenomena, in addition to the development of new alloy compositions sorely needed to meet the requirements of a rapidly expanding technological society.

Projected Capabilities of EHD

The projected capabilities of the Tabletop Powder Generator to produce rapidly quenched metallic powders for the materials scientist are listed below:

a. Solidification studies relating average cooling rate, prior to solidification, and particle size to the formation of amorphous and crystalline structures.

b. Rapid solidification studies performed to determine the effect of particle size and cooling rate on increases in solute solubility of alloyed elements.

c. Rapid solidification and heat transfer studies on extremely fine crystalline and glassy metal powders (Ref. 1).

d. Production of electron transparent metal powders. The direct observation using TEM of a complete casting is a unique capability heretofore not available.

e. Nucleation studies could be made that would relate particle size to the number of crystals (number of nuclei) in each particle.

f. Electron diffraction study of fine powders to establish the sequence of formation of stable and metastable phases in a given alloy system as a function of cooling rate.

g. The electron transparency of the fine powders produced permits studies of the growth morphology (plane front, cellular, or dendritic) during solidification. Effects of particle size, cooling rate, and solute content upon liquid-solid interface morphology can be studied.

Several of the above listed capabilities have been accomplished (Ref. 2 and 3); others are in process and under study. It will take a longer period of time to demonstrate other capabilities, but this is not the

primary objective of this program. The objective is the development of the Tabletop Powder Generator for use by material scientists to utilize these capabilities and other investigations not conceived of at the present time. The studies initiated in the program are intended to demonstrate the extent of the EHD process to produce amorphous powders and coatings, single and bicrystalline powders, protective coatings, etc. Some capabilities not associated with rapid solidification to produce powders, ions, and coatings are listed below:

a. High density powders could be made for laboratory type metallurgical experiments and alloy investigations.
b. Specialized chemical compounds could be formed by projection of molten droplets through various atmospheres to form, for example, carbides, nitrides, and hydrides.
c. High velocity small particle impingement on surfaces could be used to polish or mechanically alter the surface.
d. Thin coatings can be formed for a variety of applications.
e. Coatings can be made on a reactive substrate or under conditions not achievable in a bath or gaseous atmosphere.
f. Surface alteration can be obtained that yields a surface property different from the substrate so as to increase hardness, avoid corrosion, retard oxidation, lower materials cost, and increase wear resistance.
g. Ion and small droplet implantation could be used in applications toward fatigue resistance and semiconductor exploration.

## Technical Direction

The primary requirement of the droplet source component of the Tabletop Powder Generator is reliable operation in a difficult environment -- high voltage, high vacuum, and high temperature. Furthermore, the source should be constructed of materials which exhibit the maximum protection against corrosion due to molten alloys in contact with critical surfaces, along with minimum contamination of these alloys. In this program, several microparticle source designs that meet these requirements have

been developed. One source design utilized only ceramic materials (high purity alumina). Another design involving graphite is particulary amenable for the employment of induction heating techniques and is useful where the molten alloy or elements wet the graphite surfaces with minimum contamination. In addition, the graphite design extends the operating temperature of the microparticle source from 1500K (approximate upper limit of ceramic sources) to perhaps over 2300K. The upper temperature limit appears promising for the production of particle beams for rapid solidification studies of ceramic-based materials. Refractory materials such as boron nitride could also be employed which would further extend the operating temperature.

Accomplishments

A summary of materials that have been processed in ceramic sources by EHD for producing ultrafine powders in our laboratory are as follows: Pb-Sn (Ref. 4), Aℓ-Si alloys, Fe-Ni-P-B alloys, copper, tin, and germanium. Graphite sources have been used to produce droplet beams of silicon. Both the ceramic and graphite sources have used resistive heating elements to achieve the temperatures required to produce droplet beams of the above mentioned materials. This report contains technological, metallurgical, and apparatus advancements attained during the program activities. The technological achievements are primarily discussed in Section 2 which contains such topics as source development and operation, droplet beam effects and collection, and rapid solidification concepts. Metallurgical accomplishments, described in Section 3, include the various alloys tested and different structures obtained. Development of the Engineering Model instrumentation and projections of the Production Prototype are reported in Section 4. The following is a partial list of specific accomplishments performed on this program:

a. It has been successfully demonstrated that the EHD apparatus under development can generate fine and coarse particles (from less than 0.01μ to over 100μ)

b. Special techniques have been developed to carry out the analysis of fine particles;

c. It has been shown that the apparatus can produce rapidly solidified splats on various substrates;

d. Thin, adherent, rapidly solidified coatings ranging from microcrystalline to amorphous structures were produced on various substrates;

e. Production of large quantities of single crystalline particles (on the order of 1μ), generated from aluminum alloys, has been accomplished. Bicrystal powders were also produced;

f. Fine amorphous powders composed of an iron-nickel based alloy were made using radiative cooling alone;

g. Particle sources were operated near 1800K with no evidence of erosion;

h. Major advances have been made in EHD technology toward the development of the Engineering Model of the Tabletop Powder Generator.

SECTION 2

LABORATORY STUDIES

## 2.1 EXPERIMENTAL CONFIGURATION

Electrohydrodynamics, a technique for generating small liquid droplets, has been used for electric propulsion, ink jet printing, electrostatic purifiers, and electrostatic paint spray applications, to mention a few examples. It requires the application of intense electric fields to a liquid to cause jet or droplet breakup. To generate micro-size droplets or smaller, a very fine microspray is required. Particles less than one micron in diameter are generally not achievable in monodisperse hydrodynamic jets. A very fine jet in the micron range can be formed if the electric field is sufficiently intense when applied to a liquid surface. A fine capillary needle can be used to achieve this condition when the flow to the needle tip is properly controlled.

A source used to generate microparticles contains a capillary nozzle, a reservoir to contain the liquid, heaters to maintain the desired temperature, means of delivering the liquid to the capillary tip, and electrodes to form the electric field. The source and experimental configuration illustrated in Figure 1 is operated inside a vacuum chamber at a pressure of $10^{-5}$ torr or better. Either an inert gas controlled from outside the chamber or gravity feed is used to deliver the molten liquid to the nozzle. The intense electric field at the nozzle is provided by applying voltages up to 15 kV on the source. The extractor is operated at close to -1 kV to both enhance the electric field and retard the bombardment of the nozzle by electrons. The field acts to produce a continuous beam of micro-sized droplets. The droplets will solidify in flight to produce powders at appropriate cooling rate and collector

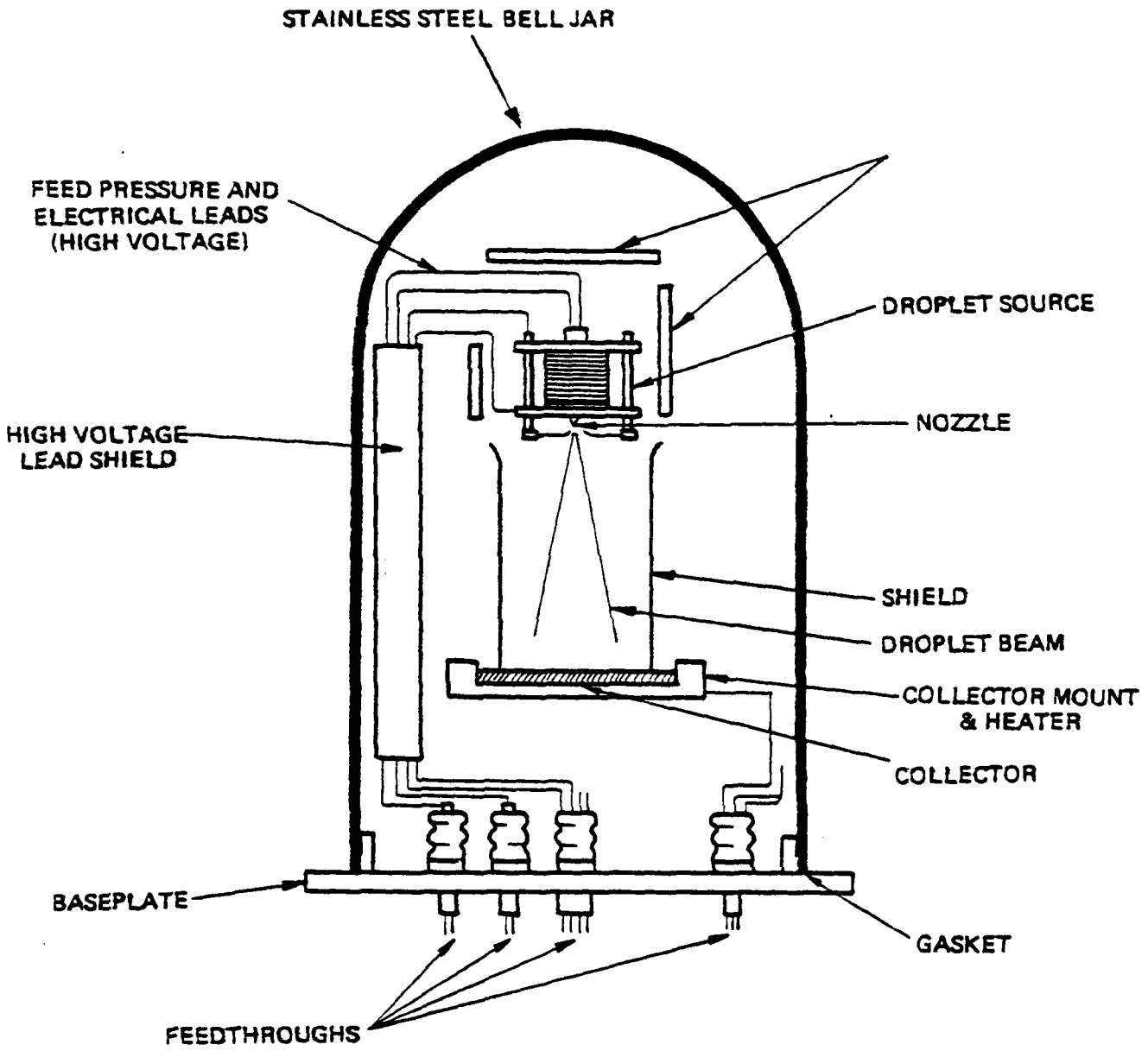


Figure 1. Experimental Design

distances. Particles are collected on various substrates including replicating tape in preparation for SEM, TEM, or other analytical techniques. When liquid droplets reach the collector before solidification, coatings and films are produced and splat cooling can be investigated. The substrate can be heated to over 1300K if desired using a special substrate resistive heater and mount. When higher temperatures are required, induction heating can be used.

As a result of several experiments in the Feasibility Model (Figure 2) and analysis on the operation of a Tabletop Powder Generator, it was determined that source operation in the vertical direction would be more advantageous than horizontal. Several more important reasons are: cylindrical symmetry in source design; gravitational symmetry; and target samples can be installed below the source (allowing for liquid collectors if desirable). The Feasibility Model was modified by attaching an antichamber to allow vertical operation, and most of the laboratory tests were performed in this chamber (shown in Figure 2). Both the horizontal and vertical chambers have a working diameter of 30 cm (1 ft.). An optical pyrometer used to measure the nozzle temperature is also visible in the photograph, along with the vertical antichamber, the high voltage safety cage, the pumping system, and the vacuum system control panel.

## 2.2 PARTICLE SOURCE DEVELOPMENT

### 2.2.1 SOURCE CONFIGURATION

The particle source under development for the Tabletop Powder Generator has undergone some significant and major changes compared with configurations reported previously (Ref. 4). The horizontal spray design tested earlier on this program was abandoned in favor of a vertical design configured to spray downward. A major advantage of the vertical source is

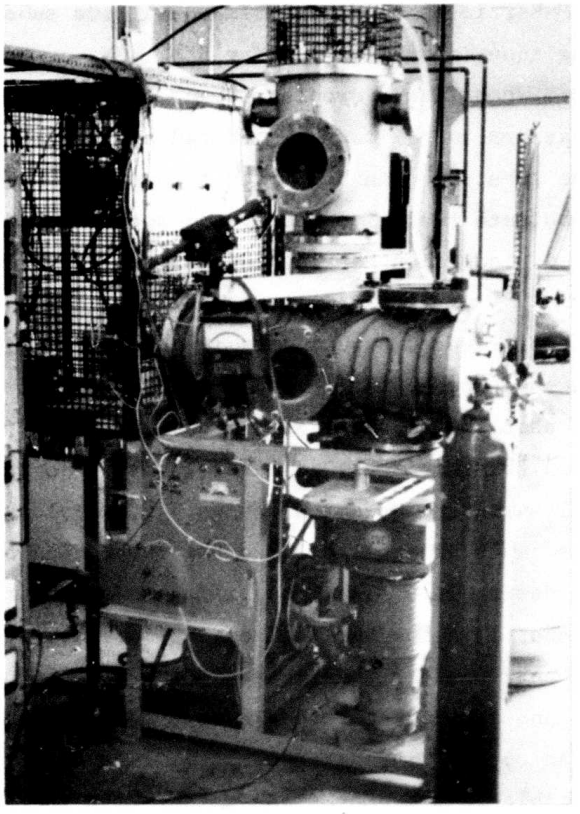

Figure 2. Feasibility Model Laboratory System in Which Basic Experiments are Performed

the use of cylindrcal symmetry in the design of individual source components and supporting hardware.

The operational and design specifications for the particle source are quite stringent. The source experiences, simultaneously, an environment consisting of high temperature (1500°C), high vacuum ($\sim 10^{-5}$ torr), and high voltage (15 kV). In addition, the source must demonstrate compatibility with molten metal alloys and introduce very little in the way of contaminates to the alloys tested. High pressures must sometimes be maintained in the melt crucible or reservoir (greater than 1 atmosphere in some cases) to force non-wetting liquids through the very fine longitudinal capillary channels in the source nozzles. This requires that the reservoir be adequately sealed in vacuum and remain leak tight at high temperatures.

During the various stages of source development, several limiting features have been identified. Of these features, perhaps the most important is the maximum nozzle temperature obtainable when using nozzle materials constructed of ceramic, such as alumina ($Al_2O_3$). Without employing high current graphite heaters or power consuming induction heating techniques, the maximum useful temperature of alumina nozzles in our design is approximately 1300°C. Nozzle temperatures in this vicinity are obtained using fine wire (0.020 inch diameter) resistive heating elements. To exceed this limit, graphite nozzles were developed and temperatures up to 1500°C have been achieved with the aid of nozzle shielding. Nozzle temperatures are discussed in more detail in subsection 2.2.2.

Early problems concerned with resistive heater reliability have been solved. The heater designs now in use are quite reliable at source temperatures near 1500°C. Turnaround times for source operation have been greatly reduced by design features which allow for fast and easy replacement of the reservoir/nozzle assemblies. The heater assemblies

or oven structure need not be replaced except for burnouts which must occur occasionally. The time between heater failures has been greatly increased, and replacement frequency can be further reduced through proper handling and operational procedures.

The overall particle source design is shown schematically in Figure 3. The numbered source components with description are listed in Table I. The alloy to be tested is loaded into reservoir (17) and melted by means of the reservoir heater (19). A separately controlled heater (13) is provided to enhance heat flow into the nozzle region. This is required in order to prevent superheating of the reservoir, so as to maintain the nonheated portion of the nozzle at the required temperature. In operation, pressure exerted by an inert gas is introduced through the sealed reservoir lid (20) and delivers the molten alloy to the capillary nozzle (12). The reservoir lid is sealed by applying torque to the support posts (21) which compresses a high temperature Grafoil gasket (not shown). The reservoir heater extends along the entire length of the reservoir body to insure that the reservoir cavity is held at a constant temperature. Large temperature gradients in the reservoir system will develop cold spots or preferred regions for the deposition of high vapor pressure constituents. To insure that depositions from the vapor state will not solidify on gas entrance holes located on the reservoir lid, thereby plugging the inlet passages preventing pressure control, the gas inlets are machined on the surfaces of the lid cover not directly facing the melt.

When the molten alloy reaches the nozzle apex centered in the extractor electrode (23), the liquid surface is dispersed under the action of electrostatic stresses (due to the applied voltage) producing a beam of molten micron and submicron particles. A substrate target located downstream intercepts the beam where the particles are collected and removed for analysis.

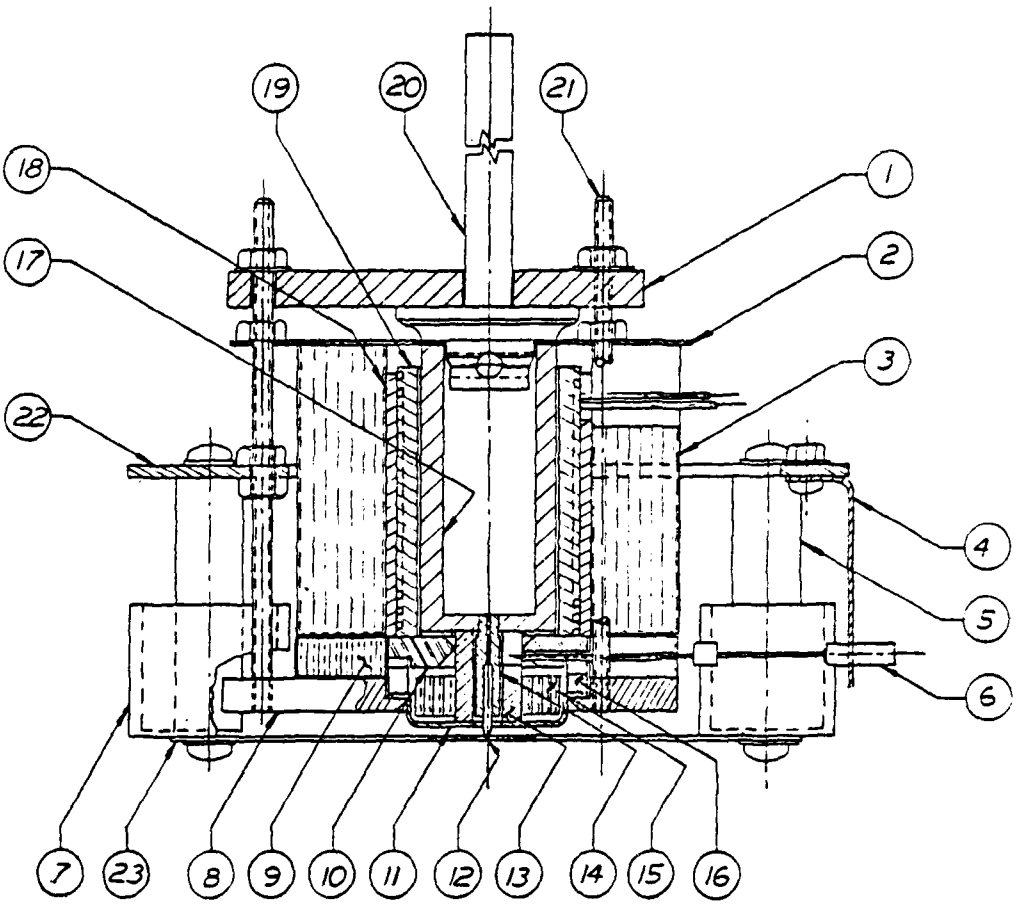


Figure 3. Tabletop Generator Microparticle Source

TABLE I

DESCRIPTION OF SOURCE PARTS

| No. | Part Name |
|---|---|
| 1 | Source Lid Clamp |
| 2 | Heat Shield Cover |
| 3 | Reservoir Heat Shielding |
| 4 | Nozzle Heater Insulator Support |
| 5 | Extractor Insulator |
| 6 | Nozzle Heater Insulator |
| 7 | Extractor Insulator Shield |
| 8 | Bottom Clamp Plate |
| 9 | Nozzle Heat Shielding |
| 10 | Reservoir Bottom Support Ring |
| 11 | Nozzle Heat Shield Cover |
| 12 | Nozzle |
| 13 | Nozzle Heater Body |
| 14 | Nozzler Holder Feed Tube |
| 15 | Nozzle Heat Shielding |
| 16 | Ceramic Spacer |
| 17 | Reservoir Body |
| 18 | Reservoir Heater Insulator |
| 19 | Reservoir Heater Core |
| 20 | Reservoir Lid and Gas Feed Tube |
| 21 | Support Post, CRES (3) |
| 22 | Support Ring |
| 23 | Extractor Electrode |

A view of an assembled droplet source without the reservoir lid (20) and source lid clamp plate (1) in place is illustrated in Figure 4(a). The view is looking directly down on the rear portion of the particle source. This view highlights the cylindrical symmetry of the source. Note the ceramic shell or liner placed between the boron nitride (BN) heater core and the tantalum heat shielding. This shell is inserted to prevent the exposed resistive heater elements from coming into direct contact with the heat shields. Both the reservoir and nozzle heater leads are brought out and attached to a mounting ring where connections are provided that extend to the feedthroughs located on the vacuum mounting flange. As mentioned previously, only the crucible and nozzle assembly need to be removed and another inserted to initiate a new test operation. Tantalum heat shields (separated by vacuum) were selected over ceramic felt, corrugated Grafoil, and graphite felt in order to avoid excessive outgassing behavior and thereby achieve clean test operation. The entire source unit is seen in Figure 5. The source diameter is approximately 10 cm.

An inclined view of the front of the particle source without the extractor electrode in place is seen in Figure 4(b). The tantalum cap serves to hold the nozzle tube heater in place and aids in supporting the nozzle heat shielding. The entire source assembly is mounted on reeds machined into a support plate. The function of the reeds is to support small displacements when the source is vibrated using a moving coil shaker. The moving coil shaker is not routinely integrated into source operation but serves as an investigatory method for flow control of non-wetting molten metals.

Several extractor electrode designs developed on this program are illustrated in Figures 6(a) and (b). Figure 6(a) depicts a graphite extractor design made from thin platelets of POCO graphite (0.005 to 0.015 inch thick). For high temperature operation approaching 1500$^{o}$C, the graphite

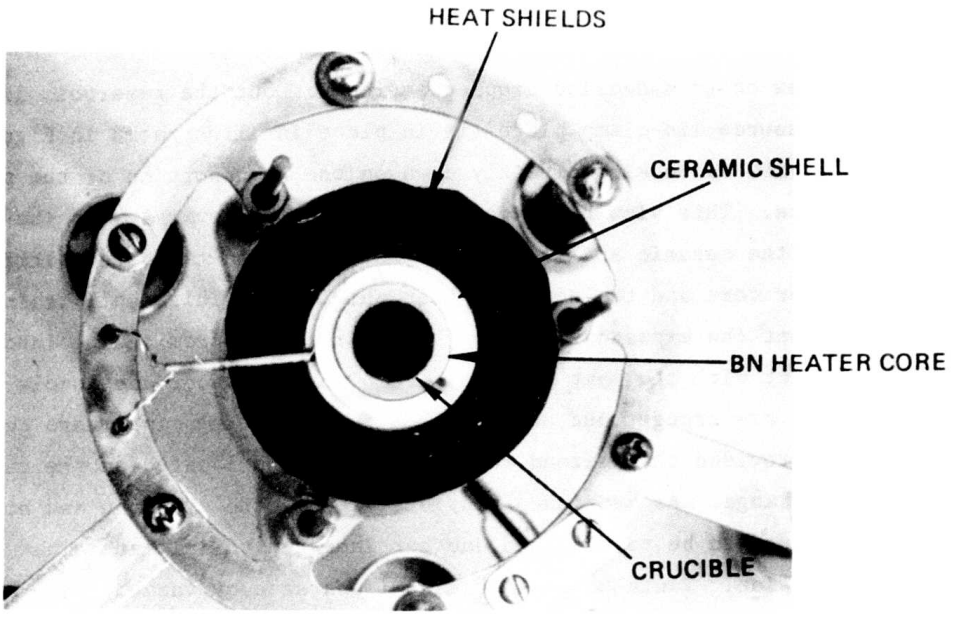


Figure 4(a). Rear View of Particle Source

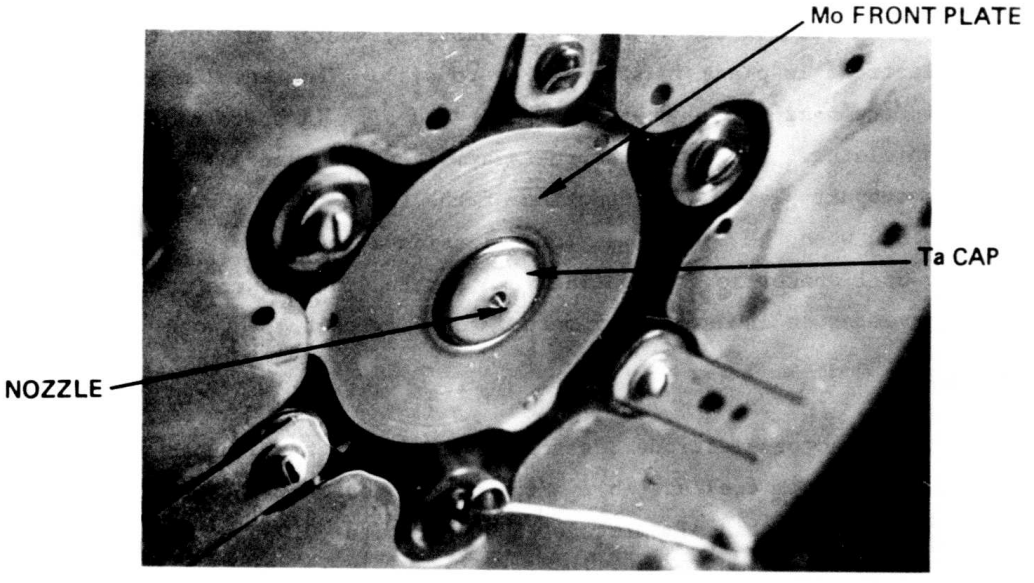


Figure 4(b). Front View of Particle Source

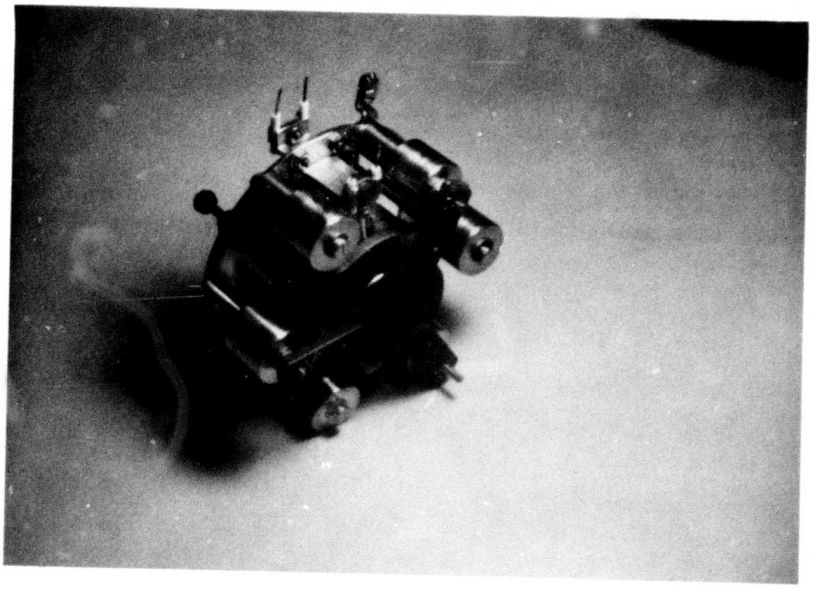

Figure 5. Microparticle Source Unit

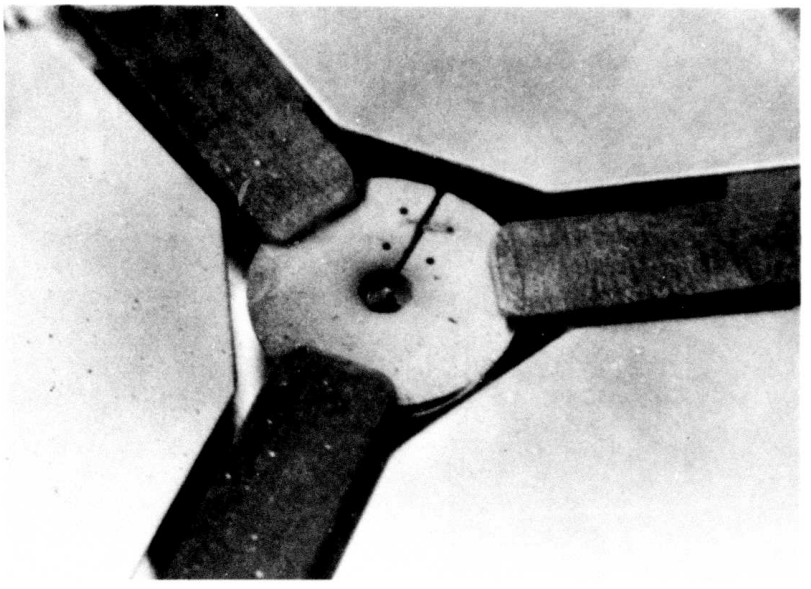

Figure 6(a). Graphite Extractor Electrode

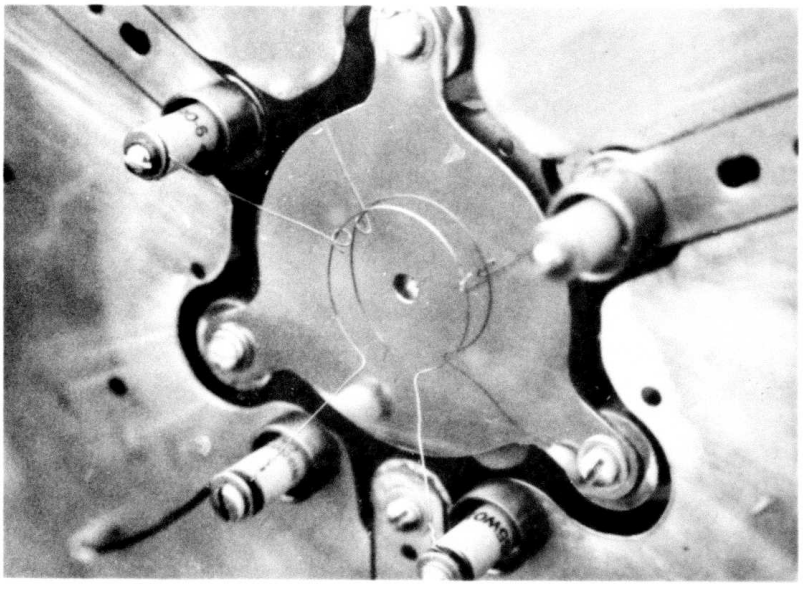

Figure 6(b) Copper Extractor Electrode

extractor is selected over the copper plate extractor electrode seen in Figure 6(b) which is used in lower temperature applications. In principle, the extractor electrode structure can be a simple metallic washer or even a wire ring. The plate in our design is advantageous, since it also serves as a single heat shield, reducing radiative heat loss from the front surfaces of the source.

The graphite extractor can also be heated by passing a current through the extractor disc. This explains the separation in the disc leading to the extractor aperture shown in Figure 6(a). Extractor heating is sometimes useful for reducing the radiation losses from the nozzle at extreme temperatures.

Source Crucible Design

The preceding represents a brief overview of particle source configuration and specifications. A more detailed description of source components will now be discussed. In order to demonstrate the variety of particle source reservoir/nozzle assemblies available to potential users, Figures 7(a) and (b) illustrate several combinations available that have been successfully tested. In Figure 7(a), a hybrid system is shown consisting of a 99.5% alumina reservoir body, POCO graphite delivery tube, and a beryllia nozzle attached. This combination was proven to be structurally compatible and performed satisfactorily without molten metal leaks at temperatures above 1000$^{o}$C. It is also useful for alloys which are compatible with graphite and BeO. A further advantage of this system is the higher thermal conductivity of these components compared to their alumina counterparts. This reduces the demand for excessive nozzle heater power required to reach desired nozzle temperatures. Several means have been found for bonding source components. The most successful joining techniques utilize high temperature ceramic and graphite cements.

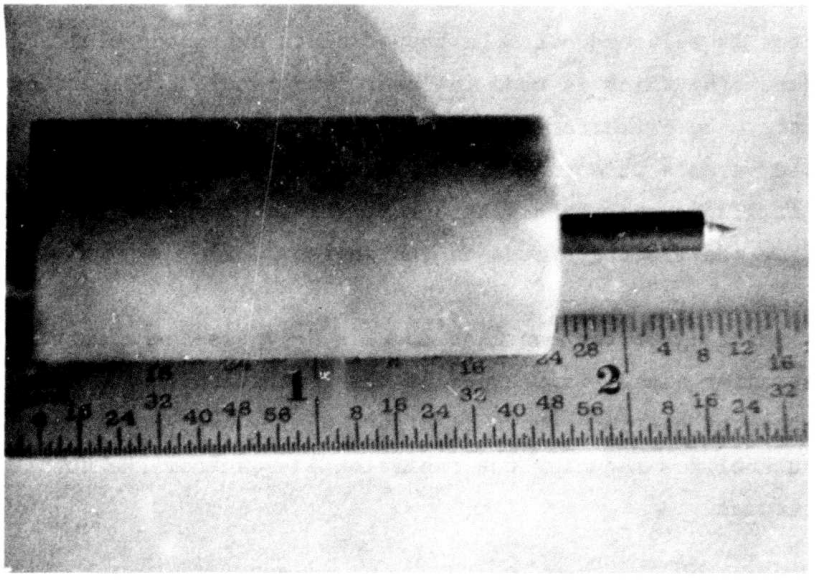

Figure 7(a). Hybrid Reservoir/Nozzle Unit

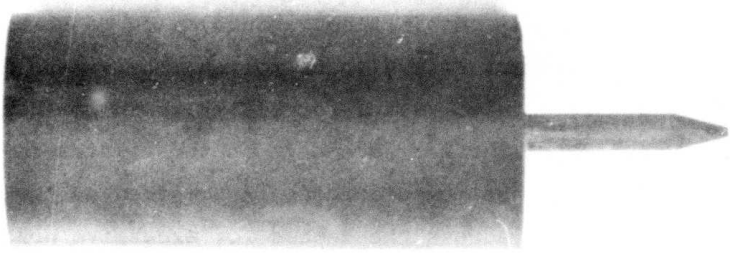

Figure 7(b). Graphite Reservoir/Nozzle Unit

A source temperature of 1500°C, used for the electrostatic dispersion of silicon, was achieved with the reservoir/nozzle system depicted in Figure 7(b). This system was fabricated using only small grained POCO graphite material. Because of the permeability of graphite to gases, the reservoir portion of the source was treated by a chemical vapor deposition (CVD) process to seal the pores in the graphite system. Ordinary untreated graphite cannot be used as a material for this application, since the reservoir must function in a vacuum environment yet remain leak-tight while internally pressurized with an inert gas. Leakage rates using conventional graphites are intolerable even for grades exhibiting minimum porosity. The nozzle tube does not require the sealing treatment, since it is protected from gas leaks by the presence of molten metal during operation.

The reservoir system used for most of the development work on this program consists of 99.5% $Al_2O_3$ material custom fabricated by a hot pressed technique and mechanically ground to final tolerances. Reservoirs fabricated in this way are expensive but required if reproducible designs are to be achieved. Tolerances associated with commercial ceramic tubing can vary significantly and are not acceptable if the reservoir is to be consistently mated to other source parts without modification.

Details of the ceramic crucible design are shown in Figure 8. The nozzle tube and reservoir body are fabricated as a single unit. Only the nozzle has to be sealed to the nozzle tube using a high temperature ceramic based cement. This design minimizes the number of seals required for source construction, thereby minimizing the possibility of molten metal leaks. When alumina nozzles are used with this design, the entire system constitutes an all-ceramic construction, and only $Al_2O_3$ surfaces are in contact with the molten alloys at any time during the source operation. Since alumina is compatible with many alloy systems, the versatility of this design is apparent. Figure 9 shows an $Al_2O_3$ ceramic reservoir, Grafoil washer seal, and reservoir gas feed lid.

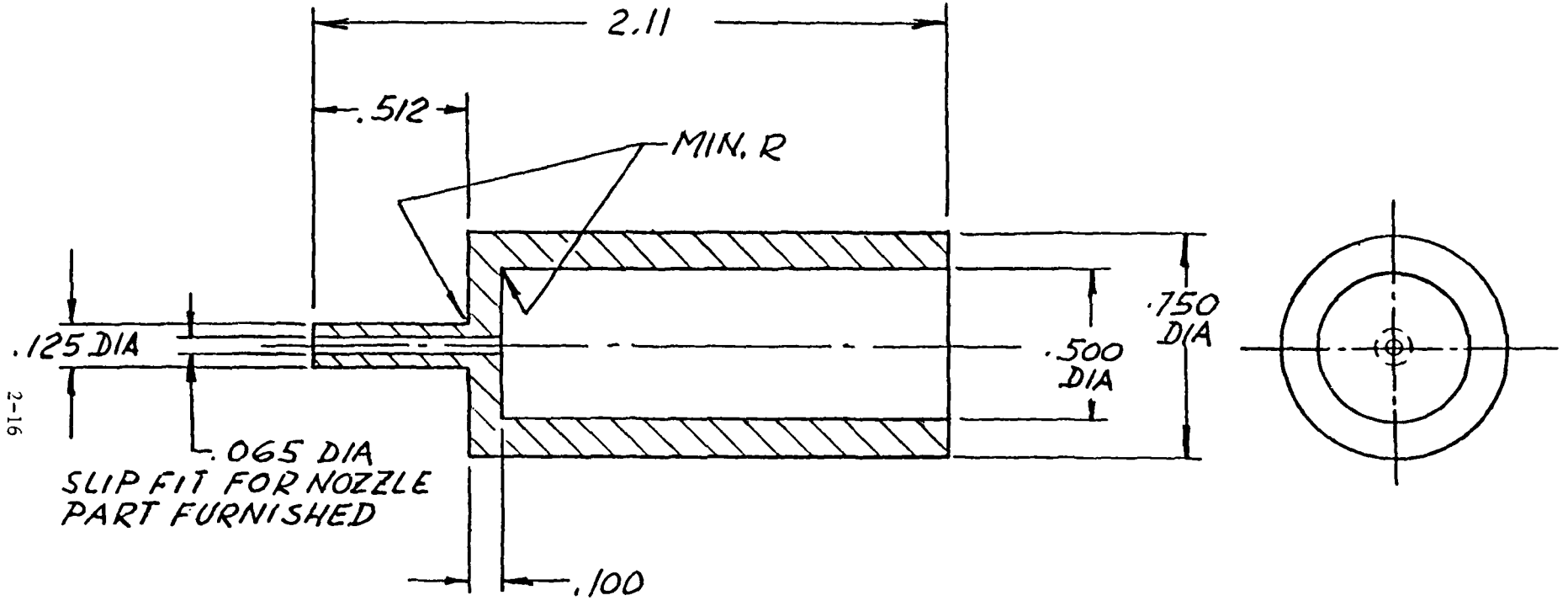


Figure 8. Ceramic Reservoir Design

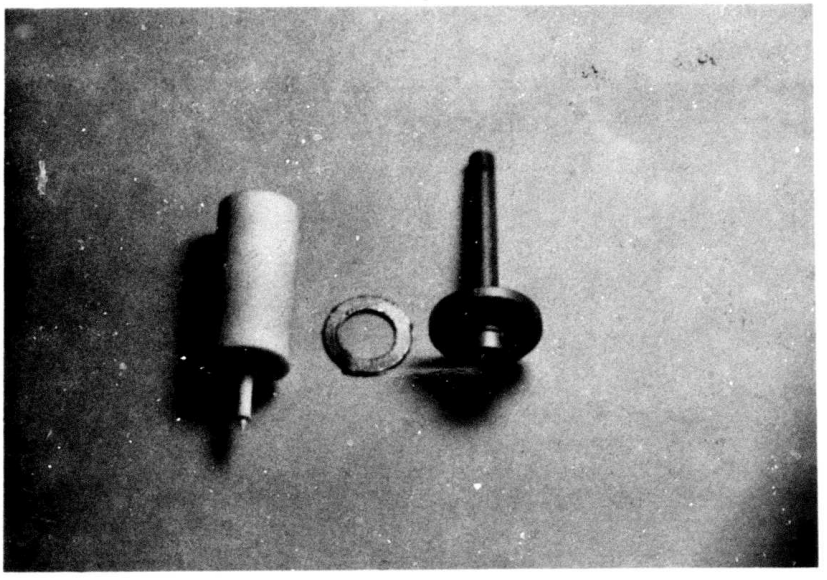

Figure 9. Ceramic Crucible Components

## Crucible (Reservoir) Heater

Figure 10(b) illustrates the reservoir heater design adapted for microparticle sources. The heater assembly consists of a thick-walled boron nitride tube with a double-threaded groove machined on the outside diameter. Resistance wire (0.020 inch diameter) made from rhenium or tantalum is wound around the core to provide the heating element. Rhenium is recommended over tantalum for continual use of source temperatures above 1200°C. It has the highest electrical resistivity and thus requires less current to achieve a given reservoir temperature, thereby minimizing joule heating losses. Also, rhenium retains ductility, even in the recrystallized condition, which reduces the problems of thermal and mechanical shock common to other refractory elements. We have not experienced any failure of this heater assembly after repeated cycling ($\sim$ 30 times). Reservoir temperatures to 1527°C at 300 watts have been obtained in tests. Details of the reservoir heater core construction are shown in Figure 11.

## Nozzle Heater Development

Problems associated with nozzle tube heater failures experienced in the past have been solved with the design depicted in Figure 10(a). Similar to the reservoir heater, a high purity boron nitride core is used to support the tantalum heating elements. It was found that rhenium elements could not be used where small bend radii are required in the heater fabrication. Rhenium cold works very rapidly and element breakage was too frequent to justify its use. Earlier designs utilized two rows of concentric heaters aligned parallel to the nozzle tube axis. The present design has three rows of heater elements to increase the heating capacity. Another essential difference is that the 0.015 inch diameter tantalum wire used previously was replaced with 0.020 inch diameter wire for enhanced structural stability. The nozzle heater is

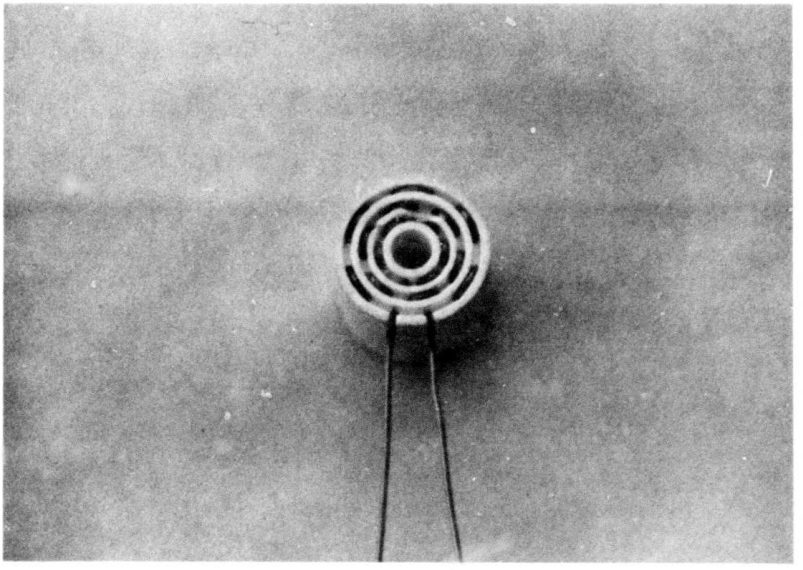

Figure 10(a). Nozzle Heater

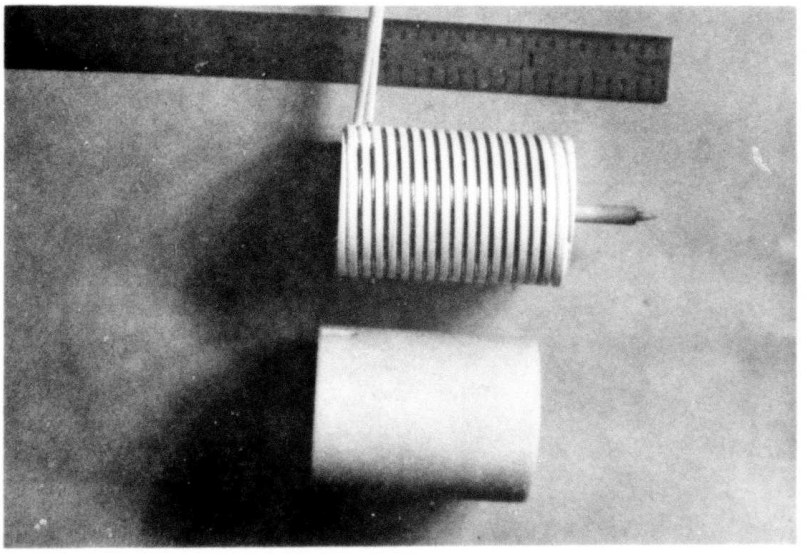

Figure 10(b). Reservoir Heater

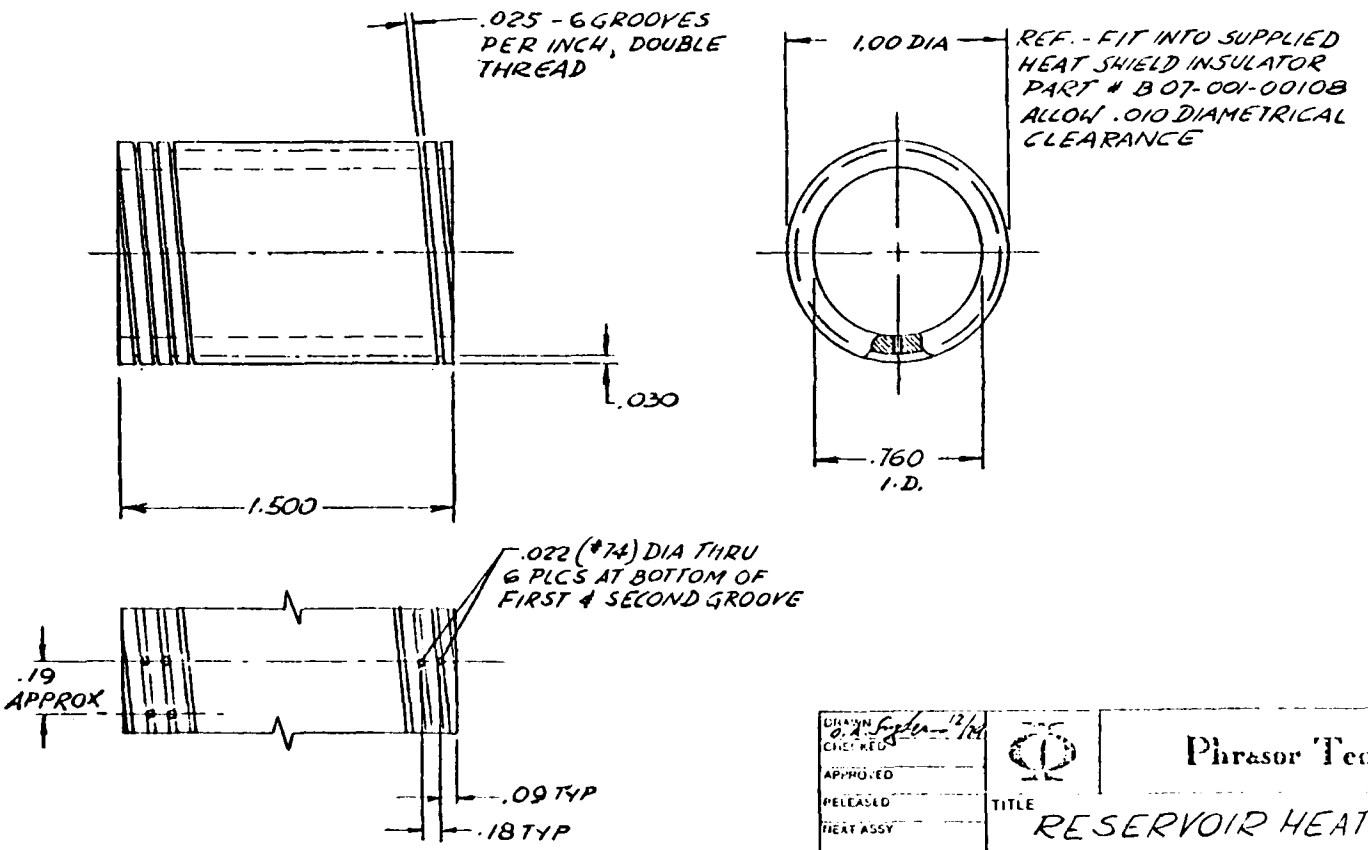


Figure 11

| | | |
|---|---|---|
| DRAWN O.A. Fuglsten 12/14 | Phrasor Technology | |
| CHECKED | | |
| APPROVED | | |
| RELEASED | | |
| HEAT ASSY | TITLE RESERVOIR HEATER CORE | |
| DIM IN INCHES | MATERIAL BORON NITRIDE GRADE HBC | |
| TOLERANCES .005 | SCALE 2:1 | DWG NO B07-001-00109 SHEET 1 REV |
| DO NOT SCALE DRAWING | CODE IDENT NO 2M923 | |

schematically illustrated in Figure 12. To improve reliability, techniques were employed to prevent the heater connections from developing hotspots by conducting heat away from these potential burnout areas in a more efficient manner. Increasing the wire diameter did introduce some fabrication difficulties using the boron nitride core. Assembling the heater by threading the heating elements through the wire channels caused frequent crumbling of the soft boron nitride. The breakdown of the structurally weak BN was avoided by designing a fixture that placed the BN under high compression during the threading operation. The performance of this heater has demonstrated a vast improvement over the previous heater.

Nozzle Configurations

Fortunately, most of the nozzles used in the microparticle source do not have to be fabricated in-house. Several nozzle configurations are available from commercial suppliers who manufacture these devices for use in the semiconductor bonding industry. Nozzle capillaries are readily available in the following materials:

a. Glass
b. Quartz
c. Tungsten Carbide
d. Titanium Carbide
e. Single Crystal Alumina (Ruby)
f. Polycrystalline Alumina
g. Beryllia
h. Tungsten

In addition to these materials, we have also fabricated nozzles from graphite. The most often used capillaries for our development work are those constructed from a polycrystalline alumina material which exhibits good resistance to corrosion for a number of alloy systems. In some cases, metallic nozzles such as tungsten or tungsten carbide may be suitable. In general, nozzle capillaries should be chosen on the basis of compatibility with the alloy and also must have a sufficiently high

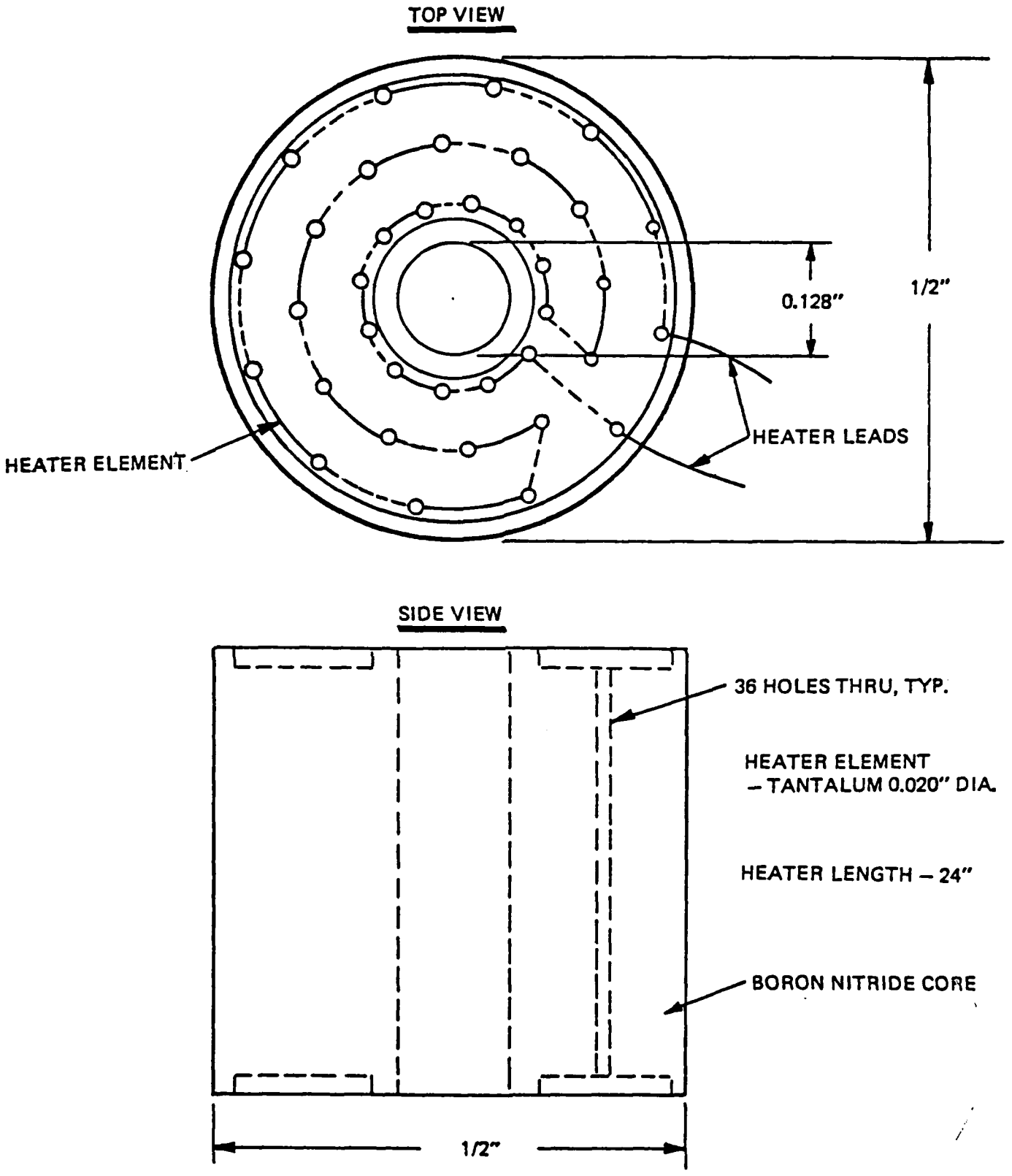


Figure 12. Nozzle Heater

melting point to resist deformation at the required operating temperatures. Figures 13(a) and (b) are photographs of alumina ceramic and graphite nozzles, respectively, used in our sources. In Figure 13(a), a single tungsten nozzle is also displayed at the lower right end.

Typically, beams of microsprayed particles are produced using nozzle capillaries having an orifice dimension of $5 \times 10^{-3}$ cm (0.002 inch) in diameter. Occasionally, orifice diameters of $2.5 \times 10^{-3}$ cm (0.001 inch) have been used but are more susceptible to clogging, owing to handling of inclusions present in the melt. Nozzles with orifices larger than $5 \times 10^{-3}$ cm generally result in throughput rates that are too large for the production of useful quantities of micron-size particles. This is especially true for non-wetting molten metals. Photomicrographs of two different ceramic capillary tip configurations are shown in Figures 14(a) and (b). The tip dimensions are approximately $2 \times 10^{-2}$ cm (0.008 inch) and $2.5 \times 10^{-2}$ cm (0.010 inch), respectively. The geometry of the contoured tip nozzle shown in Figure 14(a) provides a somewhat higher electric field at the apex compared with the flat tip design seen in Figure 14(b). Other than field strength, no significant difference in the production of particle beams has been determined from experimental investigations of the two nozzle types.

Some nozzles are mounted in potting compound and lapped for microscopic viewing of the capillary flow channel. Photomicrographs of tested ceramic capillaries are seen in Figures 15(a) and (b). Figure 15(a) shows an alumina capillary tip cemented into an alumina nozzle tube. Note the presence of a solidified non-wetting iron based alloy in the flow channel. This capillary has a $5 \times 10^{-3}$ cm (0.002 inch) orifice diameter at the tip which extends inside the nozzle distance of three to four times the orifice diameter. The hole then tapers gradually until it reaches the main capillary channel.

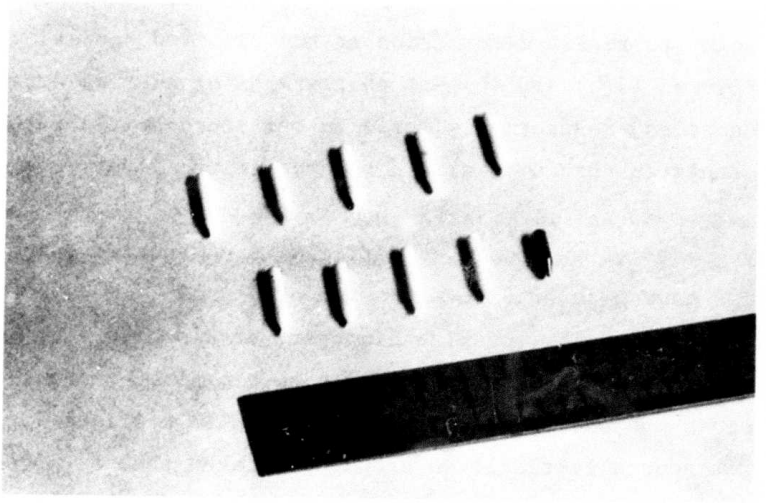

Figure 13(a). Ceramic-Tungsten Capillary Nozzles

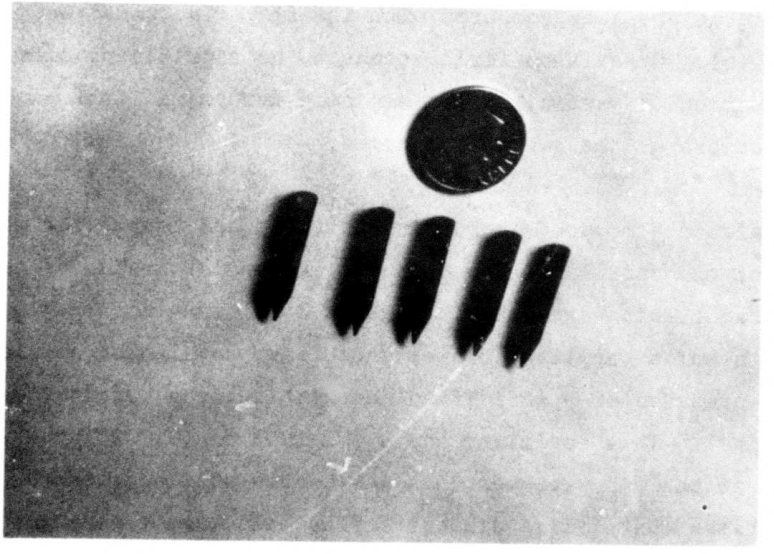

Figure 13(b). Graphite Nozzles

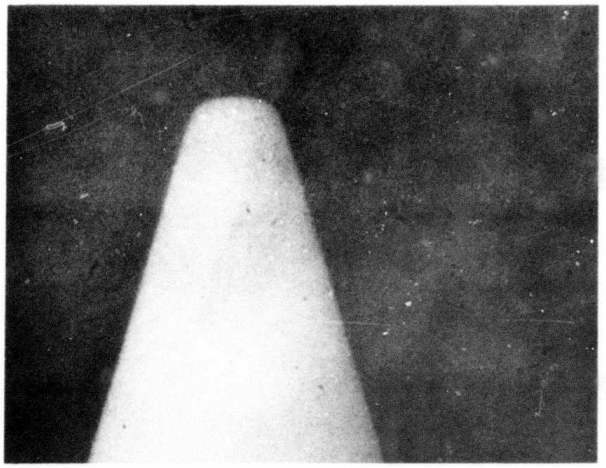

Figure 14(a). Photomicrograph of Alumina Ceramic Contoured Nozzle Tip

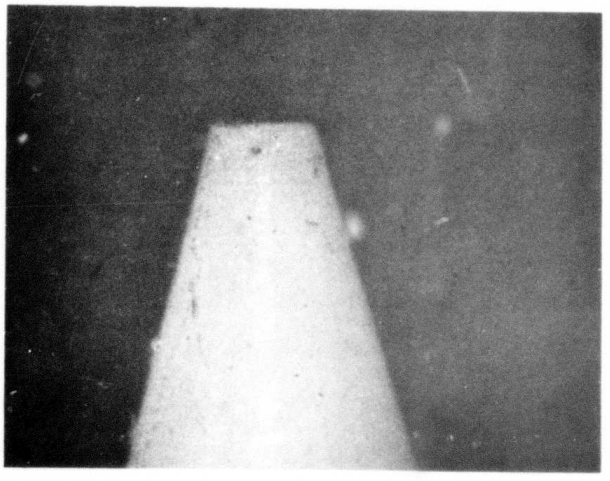

Figure 14(b). Photomicrograph of Alumina Ceramic Flat Nozzle Tip

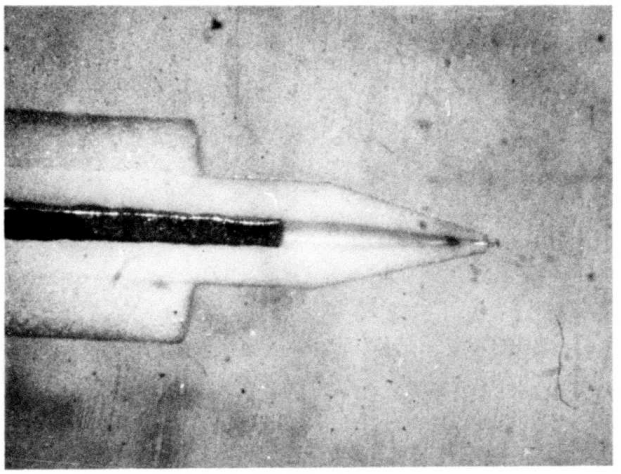

Figure 15(a). Photomicrograph of Ceramiz Nozzle Cross Section

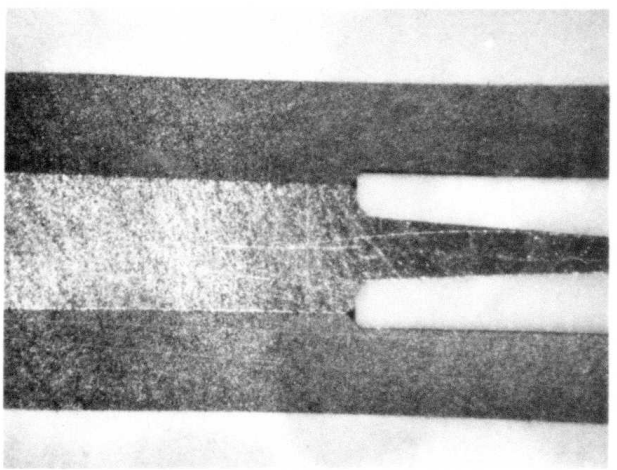

Figure 15(b). Photomicrograph of Ceramic Nozzle Cross Section (rear portion)

Similarly, Figure 15(b) is a photomicrograph showing the rear portion of an alumina nozzle cemented into a graphite feed tube. This view shows how the non-wetting alloy enters the nozzle capillary without penetrating into the region separating the nozzle from the graphite wall. This is the ideal flow condition, since the molten metal does not seep between the nozzle/nozzle tube boundary where the liquid metal can make contact with the cemented region.

### 2.2.2 HEAT TRANSFER CHARACTERISTICS OF CAPILLARY NOZZLES

Operation of the microparticle source for the Tabletop Powder Generator requires a gap of at least $7.6 \times 10^{-2}$ cm (0.030 inch) between the extractor electrode and front surfaces of the source to stand off the required voltage of up to 15 kV. The nozzle is centered coaxially in the circular aperture of the extractor electrode to enhance the electric field at the tip containing the molten alloys. A thermal analysis of the nozzle environment has provided details on the important parameters governing capillary heat transfer. The analysis also indicates the design directions one must take to optimize nozzle heating.

Even though the emissive surface area of the capillary is small, heat transfer from the nozzle base to the tip is inefficient. In actual practice, temperature differences of $\Delta T = 200^{\circ}C$ have been experienced. Thus, if solidification of the molten alloy at the tip is to be avoided, superheating the source may be necessary. This is undesirable for two reasons. First, superheating the molten alloy can accelerate reactions with any material in contact with the molten metal. Secondly, additional heat input at the nozzle tube is inefficient and, for the most part, absorbed into the source components above the nozzle due to the high thermal impedance of the capillary nozzle. This drives the heater to power levels which can jeopardize the reliability and lifetime of the heater elements.

The problems associated with nozzle heating as a function of nozzle material and design will become more apparent in the following discussion. Figure 16 shows the geometrical configuration used for the thermal analysis of the nozzle. This figure defines the length, L, of the nozzle. The source temperature used as a parameter in the graph in Figure 17 is defined as the temperature of the base of the nozzle cone as shown in Figure 16. Shown plotted in Figure 17 are nozzle tip isotherms as a function of nozzle length for source temperatures of 1200 and 1400K. Both alumina and graphite materials are displayed to demonstrate the substantial influence of thermal conductivity on nozzle temperatures. For example, consider an alumina nozzle whose desired tip temperature is 1200K. If the nozzle length is 0.25 cm, a source temperature (temperature at the base of the cone) of over 1400K would be required to achieve the stated nozzle tip temperature. At the other extreme, a graphite nozzle of equal length would only require a base temperature only $10^{o}C$ higher to achieve the same nozzle tip temperature.

If alumina nozzles are necessary for a given application, the exposed nozzle length should be kept to a minimum while maintaining a safe gap between the extractor electrode and front surface of the particle source.

The effect of capillary emissivity on the required source temperature to maintain the nozzle tip at $1450^{o}C$ is shown in Figure 18. Four isotherms ($1450^{o}C$) are depicted with various emissivities for a material having the thermal conductivity of POCO graphite (Grade DFP-1). For a given exposed nozzle length, the effect of emissivity on the source temperature required to maintain a nozzle at $1450^{o}C$ is immediately apparent. If we select a nozzle length of 0.25 cm, a material with $\varepsilon = 0.9$ requires a source temperature close to $1600^{o}C$. By comparison, a material with $\varepsilon = 0.3$ would require a source temperature of approximately $1480^{o}C$ to maintain a tip at $1450^{o}C$. Consequently, we examined possible ways for effectively reducing the emissivity of nozzle materials. Without resorting to the difficult problem of high temperature coatings, a

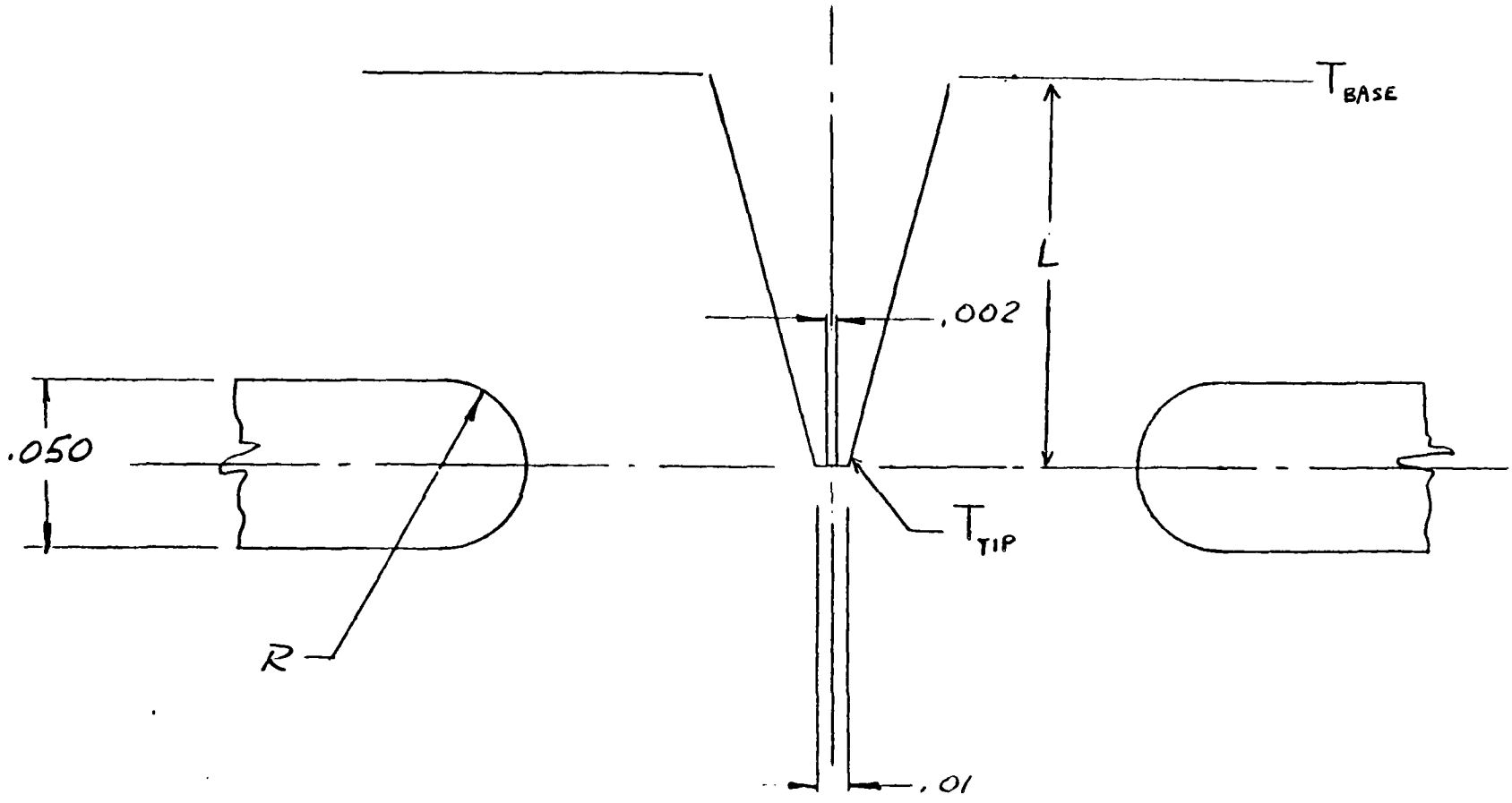


Figure 16. Nozzle Configuration For Thermal Analysis

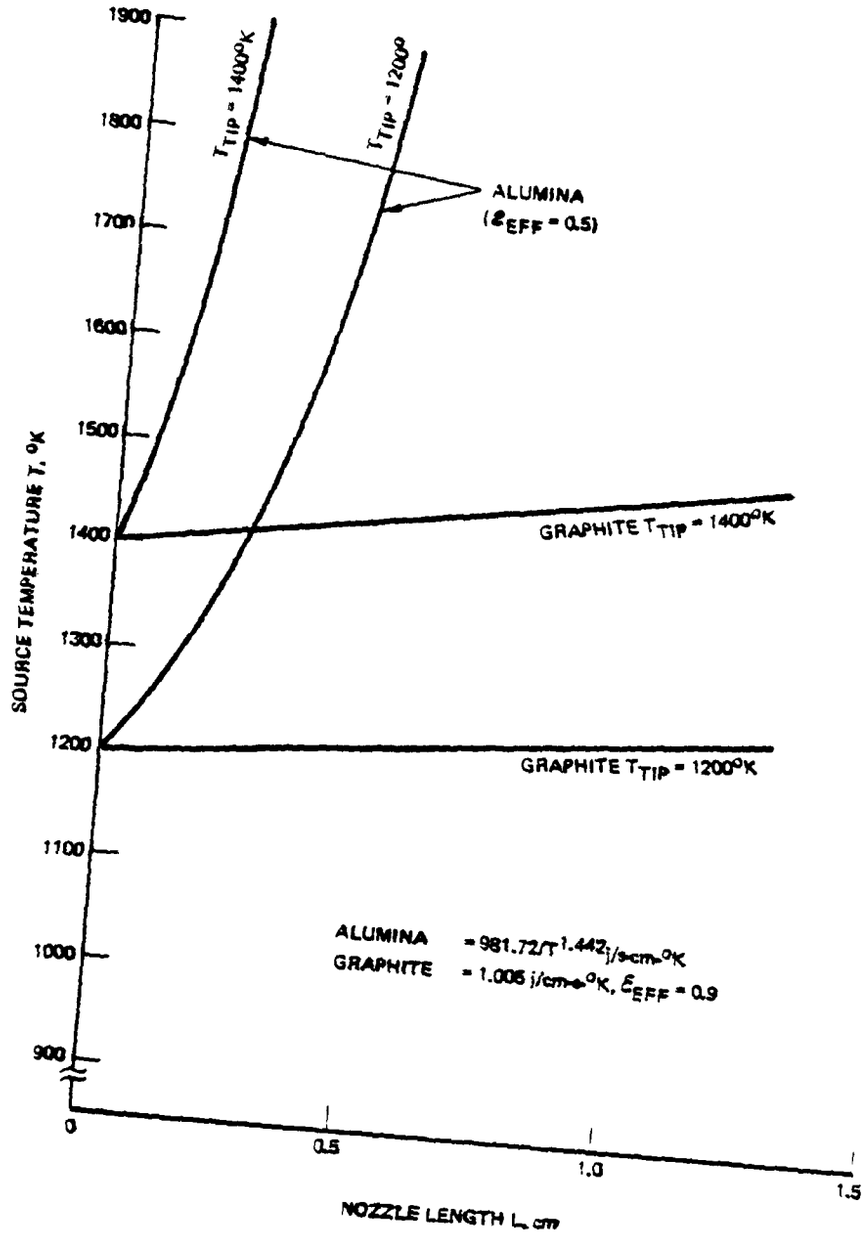


Figure 17. Minimum Source Temperature for Specified Nozzle Tip Temperature

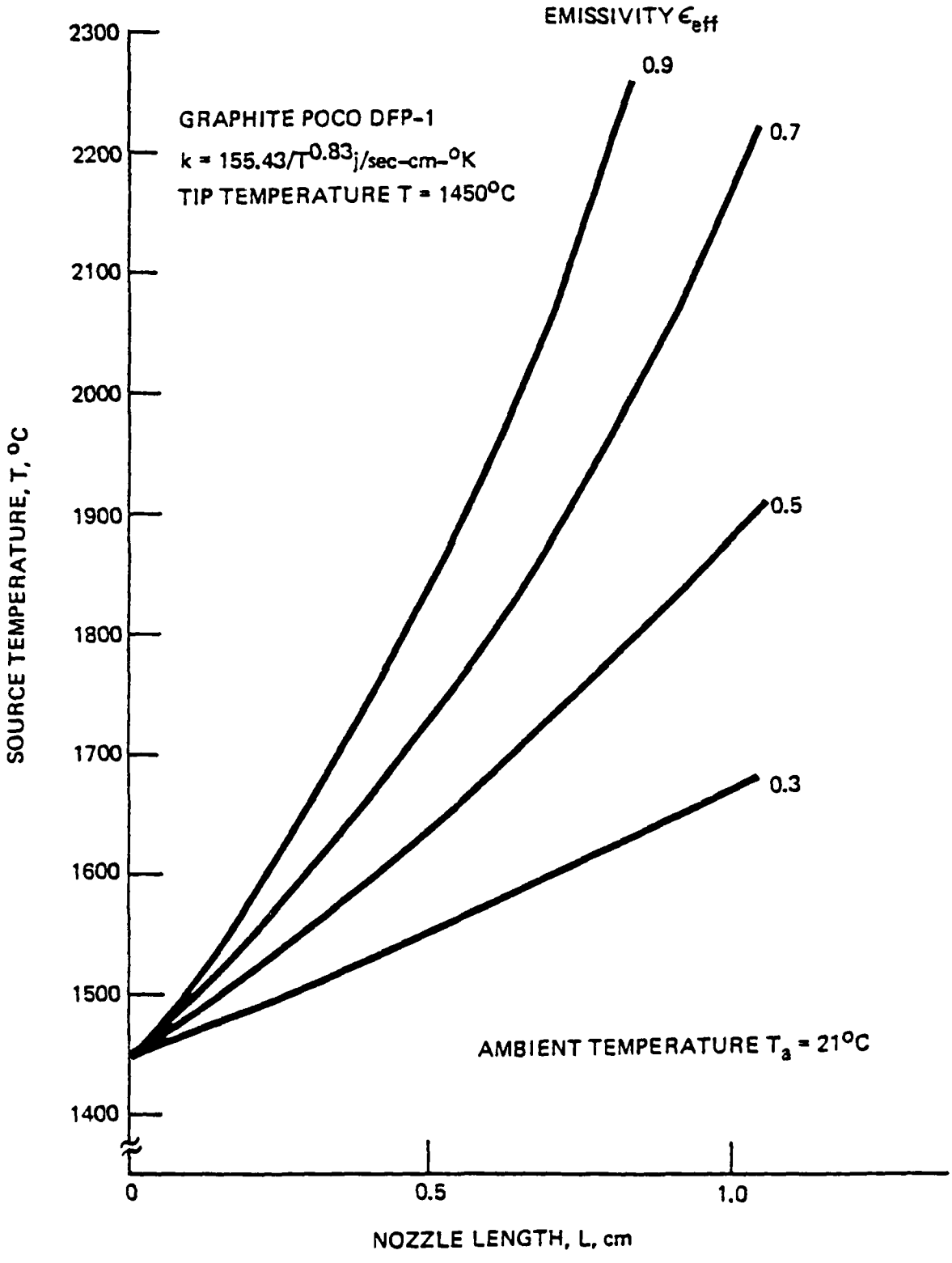


Figure 18. Effect of Emissivity on the Required Source Temperature

single "cone-shaped" shield to overlay the nozzle was considered. The shield material should have a high melting temperature, low vapor pressure, and exhibit the lowest emissivity possible at the operating source temperature.

The effect of a single shield surrounding the nozzle is illustrated in Figure 19. The emissivity of the shield material varies along the abscissa, and the effective emissivity of the nozzle/shield structure is plotted on the ordinate axis. Several curves are shown for nozzle materials having emissivities of $\varepsilon_n$ = 0.9, 0.6, 0.5, and 0.4. Results of installing a single shield are determined from the plots in the following manner. Find the shield emissivity on the abscissa and proceed upward to the curve displaying the emissivity of the nozzle material without a shield. The effective emissivity of this combination is read directly from the ordinate scale. For example, if one places a shield of $\varepsilon_s$ = 0.3 around a nozzle of emissivity $\varepsilon_n$ = 0.9, the effective emissivity of this combination is reduced to approximately $\varepsilon_{eff}$ = 0.15.

In our studies, we have selected tantalum as a shield material. The results of tests employing the shield technique have verified the thermal model, and nozzle temperatures of 1450°C can be routinely achieved using graphite without superheating the source. The fact that $\varepsilon_{eff} < \varepsilon_s$ is a consequence of the radiative heat transfer between the nozzle and the shield. Application of a high temperature coating with an emissivity of 0.3 to the graphite nozzle would result in an emissivity of 0.3 for this combination - provided the coating strongly adhered to the nozzle material. Figure 20 shows a graphite nozzle cone with a tantalum shield attached.

### 2.2.3 CAPILLARY NOZZLE CALIBRATION FOR MASS THROUGHPUT ANALYSIS

A useful means for the direct measurement of mass flowrate during the operation of the EHD microparticle source has not been devised to date.

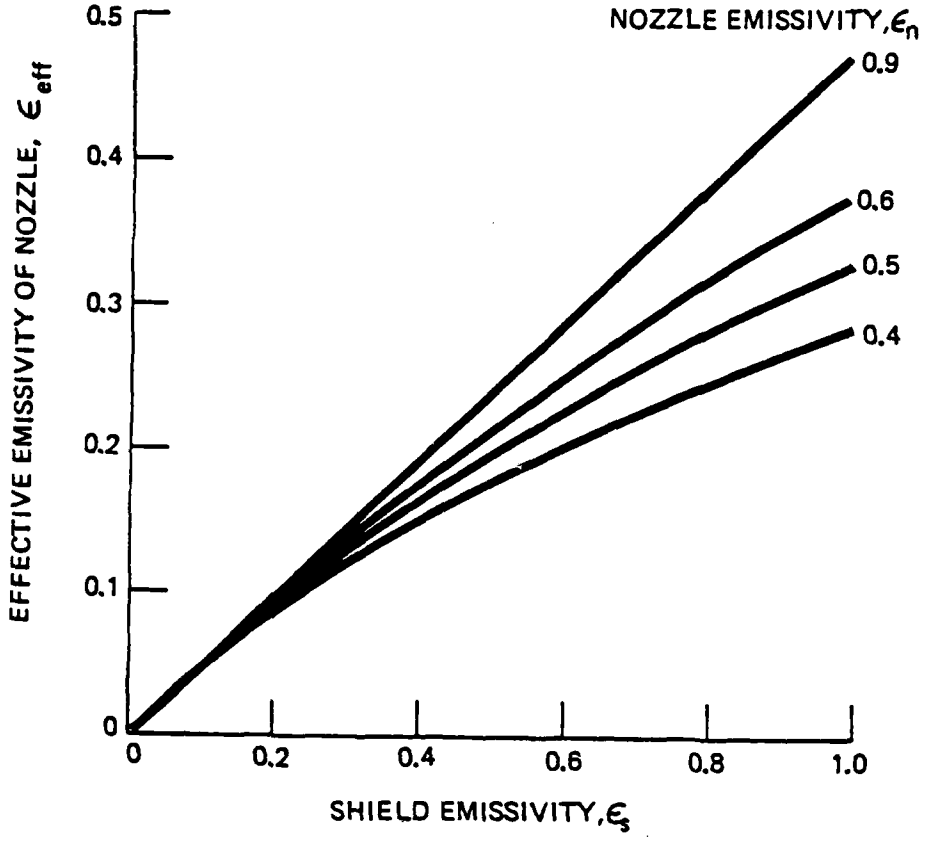


Figure 19. Effective Emissivity of Shielded Nozzle

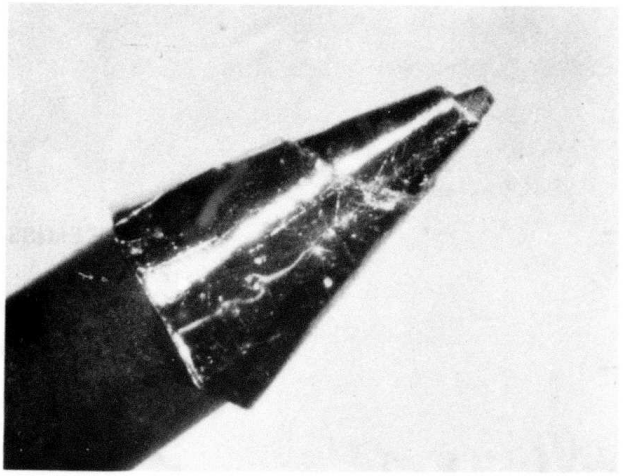

Figure 20. Graphite Nozzle with Tantalum Shield Attached

A rather simple way of arriving at the average mass throughput for a typical test run has been used by weighing the reservoir before and after the run and dividing the mass sprayed by the test period (beam-on time).

A more useful technique, which allows one to compute the instantaneous throughput, employs a method based on a pretest flow calibration of the capillary nozzle. We have constructed a calibration apparatus from which an effective conductance, $K_{eff}$, can be determined for flowrate calculations. The apparatus consists of a container filled with a test fluid, a means of adjusting the container height to vary the pressure forcing the liquid through the capillary nozzle, and a precision bore calibration tube. The nozzle calibration apparatus is depicted in Figure 21. The container (not shown) is raised to a height, h, above the nozzle plane producing a head pressure of $\rho gh$, where $\rho$ = density of the fluid and g = the acceleration due to gravity. The fluid leaving the nozzle enters the calibration tube where the distance traversed between two selected fiducial markings is carefully timed. Flow measurements to determine $K_{eff}$ are made on each nozzle tested in the microparticle source. This must be done since $K_{eff}$ varies from nozzle to nozzle. The variations are due to dimensional differences introduced in the nozzle manufacturing process. This has been verified by the capillary nozzle manufacturer.

The value of $K_{eff}$ is given by

$$K_{eff} = \frac{\eta \dot{m}}{\rho (\Delta P)^n} \qquad (1)$$

where $\Delta P$ is equivalent to $\rho gh$ in the calibration apparatus, $\eta$ is the test fluid viscosity, $\dot{m}$ is the measured flow rate (g/s) and the exponent n is determined from the experimental measurements of mass flow rates.

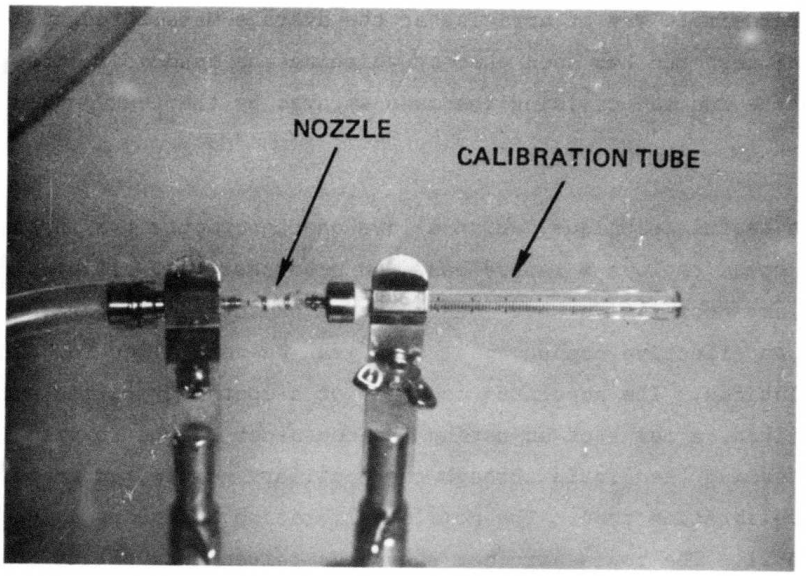


Figure 21. Nozzle Calibration Apparatus

In Eq. (1), $\dot{m}$ is the flow rate measured with the aid of the calibration tube and is given by

$$\dot{m} = \pi \rho r_t^2 v_t \qquad (2)$$

where:

$r_t$ = radius of the calibration tube

$v_t$ = velocity in the calibration tube

Substitution of $\dot{m}$ from Eq. (2) into Eq. (1) yields

$$K_{eff} = \frac{\pi r_t^2 \ell}{(\Delta P)^n t}$$

where $v_t = \ell/t$ and $\ell$ is the distance traversed by the test fluid in the calibration tube in time, t.

By plotting several measurements of mass flow rates against $\Delta P$ or h on log-log paper, it is found to be a straight line over the fluid velocity range encountered in our measurements. A typical plot of calibration data is shown in Figure 22. The value of the exponent n in Eq. (1) is determined from the slope of the linear plot. The pressure exponent was determined from the nozzle data in Figure 22 as n = 0.92. For a standard test fluid of isopropyl alcohol and a calibration tube of 0.020 inch radius, an average value of $K_{eff}$ was determined from Eq. (1) to be $K_{eff} = 1.27 \times 10^{-9}$. The calibration tube radius is selected so that the conductance introduced by this flow element is much larger than the nozzle conductance.

Once $K_{eff}$ and n have been determined from calibration tests, the instantaneous flow rate for the microparticle source can be obtained from the expression

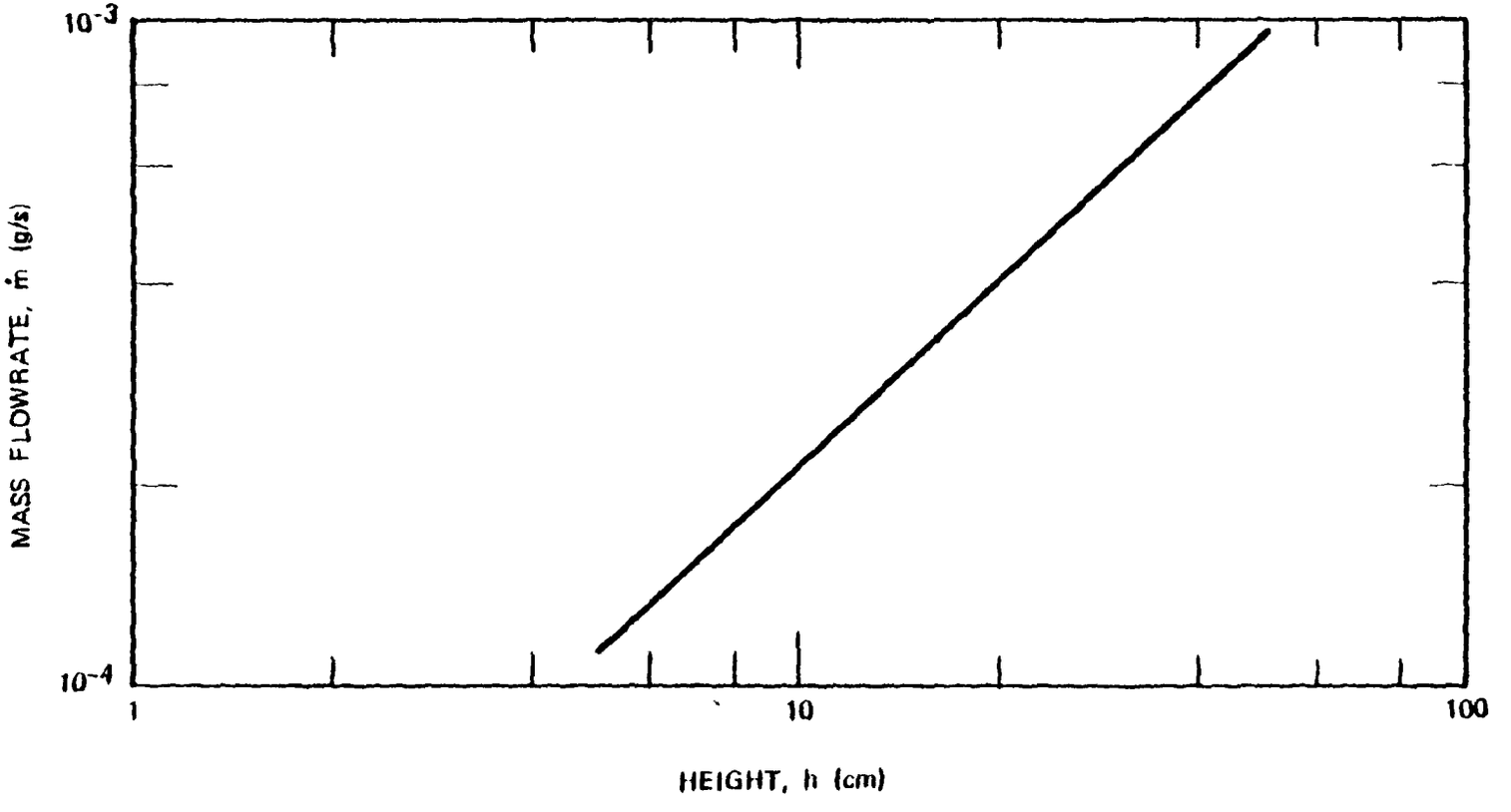


Figure 22. Nozzle Calibration Data

$$\dot{m} = \frac{\rho}{\eta} K_{eff} (P_a)^n \qquad (3)$$

where $\rho$ and $\eta$ are now the density and viscosity of the molten alloy, respectively, and $P_a$ is the applied pressure. The molten metal velocity, v, as it exits from the nozzle orifice is then

$$v = \frac{K_{eff}}{\pi r^2 \eta} (P_a)^n \qquad (4)$$

where r is the radius of the nozzle orifice. Note that Eqs. (3) and (4) are valid only when the actual fluid viscosities in electrostatic spray tests are similar to those of the fluid in the calibration apparatus. Work on characterization of nozzle conductances, both experimental and theoretical, will continue in order to develop models that predict molten metal flowrates in the Tabletop Powder Generator.

The mass throughput $\dot{m}$ and fluid velocity, v, were calculated at the onset ($\dot{m}_o$,$v_o$) and cutoff ($\dot{m}_c$,$v_c$) for Cu, Aℓ, and Sn for a nozzle characterized by the n and K parameters given above. These values, determined from Eqs. (3) and (4), are listed in Table II.

TABLE II

CALCULATED VALUES FOR MASS FLOWRATE AND VELOCITY FOR ELECTROSTATICALLY SPRAYED Cu, Aℓ, and Sn

| Element | $\dot{m}_o$ (g/s) | $v_o$ (cm/s) | $\dot{m}_c$ (g/s) | $v_c$ (cm/s) |
|---|---|---|---|---|
| Cu | $7.39 \times 10^{-2}$ | 407 | $4.24 \times 10^{-2}$ | 234 |
| Aℓ | $3.9 \times 10^{-2}$ | 715 | $8.92 \times 10^{-3}$ | 163 |
| Sn | $5.5 \times 10^{-2}$ | 375 | $3.34 \times 10^{-2}$ | 226 |

These calculations do not include any effects of voltage on mass throughput. There is experimental evidence that the source voltage increases the flowrate, but a quantitative description of this dependence is not yet available.

## 2.3 DISPERSION OF MICRO-SIZE DROPLETS IN THE EHD SPRAY OF NON-WETTING MOLTEN METALS

In the Tabletop Amorphous Powder Generator, several monotomic metals and alloy systems may be processed by metallurgical investigators. The behavior of many metallic systems available to the researcher in the Tabletop apparatus requires an examination of the expected results in terms of the physical properties of the materials and process parameters. The desired result, independent of material processed, is the generation of micro-sized droplet beams or micro-spray for rapid solidification, nucleation, and alloy studies. In order to predict the operating requirements that will enable a variety of metallic systems to produce micro-sprays, several useful criteria have been established to determine the processing of different materials. In the following analysis, the characteristics of non-wetting molten metal systems will be considered primarily. This condition is desirable to prevent unwanted contamination of the processed material in contact with droplet source components.

### 2.3.1 DISPERSION CRITERIA

When the molten material is delivered to the nozzle tip as shown in Figure 23, the electrostatic stress acting on the liquid meniscus must provide sufficient force to disrupt the surface, thereby "atomizing" or dispersing the material which then forms a micro-size droplet beam. If the electrostatic stress is too low, a columnar liquid jet of undispersed molten material may form, provided the orifice exit velocity satisfies the minimum velocity criteria for jet formation.

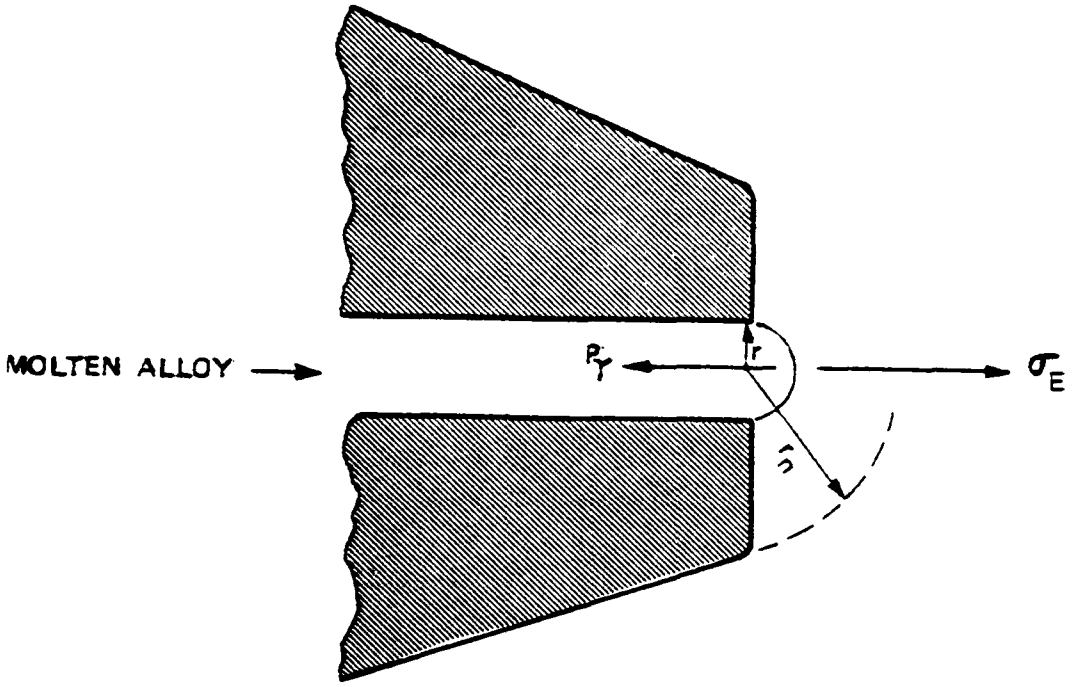


Figure 23. Nozzle Tip Showing Forces Acting on Liquid Surface

The $\sigma_e$ stress acting at a conducting surface under the application of a field, E, is given by:

$$\sigma_E = \frac{1}{8\pi} (E/300)^2 \text{ dyne/cm}^2 \tag{5}$$

The stress is directed outward from the liquid meniscus, tending to pull the surface away from the nozzle. The negative pressure provided by the meniscus forces, as depicted in Figure 23, opposing the electrostatic stresses can be expressed as:

$$P_\gamma = \left| \frac{2\gamma\cos\theta}{r} \right| \qquad (\theta > 90°) \tag{6}$$

where $\gamma$ is the surface tension, $\theta$ is the contact angle, and r is the radius of the meniscus, assumed equal to the nozzle orifice radius. For an electrostatic spray to be initiated, we postulate that the dispersion criteria

$$\sigma_E > P_\gamma \tag{7}$$

must be satisfied.

For a typical nozzle configuration used in sources for the Tabletop Generator, the electric field at the nozzle tip is related to the applied voltage, V, by the relation:

$$E_o = \frac{V}{kr_n} \tag{8}$$

The constant k in Eq. (8) is the field reduction factor to account for the conical shank geometry of the nozzle. The value of k is estimated from the relation (Ref. 5)

$$k = \tfrac{1}{2} \ln (4x/r_n) \tag{9}$$

where x is the radius of the extractor electrode orifice and $r_n$ is the radius of the nozzle. For nozzles and electrode geometries presently in use, k = 2.62.

As shown in Figure 23, the meniscus as illustrated protrudes one orifice radius in front of the nozzle. If we assume the meniscus initially reaches the position depicted before disruption, the field at the meniscus surface would be higher than the field $E_o$ averaged over the nozzle tip. The field E at a hemispherical boss on a plane surface has been computed to be enhanced according to $E = 3E_o$. Substituting of the modified field factor into Eq. (8) and using Eqs. (5), (6), and (9), the electrostatic dispersion condition becomes:

$$D_s \equiv \frac{10^{-4} r_m}{16\pi\gamma\cos\theta} \left(\frac{V}{kr_n}\right)^2 > 1 \qquad (\theta > 90^o) \tag{10}$$

A more rigorous analysis to determine the minimum voltage required to initiate spraying is given by Hendricks et al (Ref. 6). Our result is for a slightly modified condition but compares favorably with their analysis.

As long as the inequality in Eq. (10) is satisfied, the molten metal arriving at the nozzle tip should disperse to produce a beam of charged particles. If $D_s$ is less than unity, a jet of partially or non-atomized material may issue from the orifice. This has, in fact, been observed with $Fe_{75}Si_{15}B_{10}$ alloy when the applied voltage resulted in $D_s < 1$. It can be seen from Eq. (10) that the dispersion relation depends not only on the process parameters such as the nozzle voltage, V, but is also dependent on geometric factors associated with the design of the nozzle and the material property of surface tension.

Various modes for the electrostatic dispersion of molten metals are observed with the Tabletop Powder Generator microparticle source. With the

aid of Figure 24, the more important modes experimentally observed will be defined for use in the following discussion. In Figure 24(a), the microspray mode is illustrated. This mode is typical of the spray observed with the electrostatic dispersion of aluminum, aluminum alloys, and tin. In general, the microspray mode is generated when the following conditions are satisfied:

a. Low surface tension molten metals are used with $\gamma < 1100$ dyne/cm.
b. Low mass flowrates are achieved.
c. The dispersion relation $D_s > 1$.

The microspray condition characterized by a high yield of low micron and submicron particles is considered ideal for the production of rapidly solidified particles. The mode depicted in Figure 24(b) is typical of what is observed when the voltage is increased over that which is required to produce a stable microspray. The beam is characterized by a microspray mixed with visible large droplets. Increasing the voltage even further results in an increase in particle size, which is an indication that voltage affects the flowrate. In this latter condition, large pendant drops can form on the nozzle, perhaps, precipitated by large flow rates and low fields due to space charge shielding of the nozzle tip by the larger droplets. When the pendant drop forms, electrostatic dispersion ceases, which is caused by reduced nozzle fields and partial solidification on the underside of the massive drop attached to the nozzle.

The dispersion modes seen schematically in Figures 24(c) and (d) are typical modes ovserved under the following conditions:

a. High surface tension molten metal with $\gamma > 1300$ dyne/cm.
b. High mass flow rates.
c. The dispersion relation $D_{s,} < 1$.

(a) MICROSPRAY

(b) MICROSPRAY MIXED WITH LARGE DROPLETS

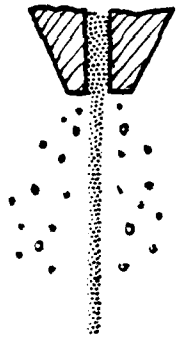

(c) LIQUID METAL STREAM MIXED WITH LARGE DROPLETS

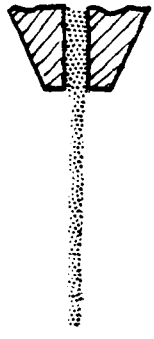

(d) LIQUID METAL STREAM

Figure 24. Experimentally Observed Disperion Modes

Even with an applied voltage of 10 kV on the nozzle, an undispersed liquid metal jet (Figure 24(d)) was observed with an $Fe_{75}Si_{15}B_{10}$ alloy whose surface tension was estimated to be 1600 dynes/cm. By increasing the nozzle voltage, the dispersion mode in Figure 24(c) was induced. Further increase in voltage resulted in the mode of Figure 24(b), but a complete microspray mode was never obtained in these tests. The achievement of the required dispersion voltage for high surface tension materials is under investigation.

A class of aluminum alloys including pure Aℓ, Aℓ-3%Si, Aℓ-6%Si, and Aℓ-4.5%Cu has been thoroughly explored in the Tabletop Powder Generator Apparatus. For all these alloys, the dispersion relation (Eq. (10) is satisfied and stable microspray of droplets is produced. As an example, let us compute the value of $D_s$ for pure aluminum using typical values encountered in actual operation as follows:

$r_m = 2.54 \times 10^{-3}$ cm
$\gamma = 850$ dynes/cm
$\vartheta = 143^{\circ}$
$V = 10$ kV
$r_n = 1.02 \times 10^{-2}$ cm
$k = 2.62$

Insertion of these values in Eq. (10) yields the result $D_s = 1.04$, indicating that an electrostatic spray should be initiated. A value of $D_s = 0.526$ was calculated for the iron alloy mentioned previously which did not form a stable microspray at a voltage of 10 kV. Rather,a molten cylindrical jet was formed. The iron alloy should produce a microspray when the onset of the spray is initiated at a voltage level that satisfies the dispersion criteria, provided the mass throughput is not too high.

Since the above calculated values for the dispersion criteria are relatively close to unity, they are only an indication as to whether the microspray or jet mode will result in actual operation. This is due primarily to the uncertainty in the values used for the electric field and contact angles. As the values of $D_s$ depart significantly from unity, the behavior predicted by the dispersion criteria should be correspondingly more reliable.

The critical field required to initiate the meniscus disruption is subsequently altered when the microspray condition is established. The field is modified by the space charge provided by the presence of positively charged droplets. Local fields existing at micro-filaments, small compared to the orifice dimensions, could exceed the average field required for initiating dispersion.

The dispersion criteria for molten Cu, Aℓ, and Sn are listed in Table III for a nozzle voltage of 8 kV. These values are calculated from Eq. (10) using nozzle dimensions of $r_n = 1.02 \times 10^{-2}$ cm and $r = 2.54 \times 10^{-3}$ cm.

TABLE III

DISPERSION VALUES FOR MOLTEN COPPER, ALUMINUM, AND TIN

| Metal | Surface Tension (dyne/cm) | Contact Angle, $\theta$ | $D_s$ |
|---|---|---|---|
| Cu | 1360 | $138^\circ$ | 0.448 |
| Aℓ | 850 | $116^\circ$ | 1.22 |
| Sn | 544 | $121^\circ$ | 1.62 |

At 8 kV, both Aℓ and Sn satisfy the dispersion condition $D_s > 1$ and were observed to produce microsprays under these conditions. Copper did not disperse into the desired mode at 8 kV. The required voltage for copper can be estimated from Eq. (10) by setting $D_s = 1$ and solving for the

voltage. The required dispersion voltage is determined to be 12 kV. Although this value is estimated to be necessary, it may not be sufficient to produce the desired microspray. The increase in the molten metal flowrate and in the space charge shielding is expected to influence the nature of the electrostatic spray process. The contact angles used in the above calculations were measured in the Tabletop Powder Generator apparatus as discussed in the next subsection.

### 2.3.2 ESTIMATE OF CONTACT ANGLES

Contact angle values are required in the calculation of the dispersion criteria. A measurement of the contact angle for non-wetting molten metals in contact with capillary nozzle materials can be made in-situ. This is done in the Tabletop Powder Generator by making use of the relation

$$P_\gamma = \frac{2\gamma\cos\theta}{r} \tag{11}$$

The pressure $P_\gamma$ exerted by the fluid meniscus contained in a capillary nozzle opposes liquid motion when a positive pressure is applied to the fluid. When the applied pressure P exceed $P_\gamma$, the fluid will then move in the direction of the applied pressure. The onset pressure $P_o$ measured for the initiation of the microspray is assumed equal to the pressure $P_\gamma$ for the non-wetting meniscus configuration. Thus, the contact angle for non-wetting molten metals ($\theta > 90^o$) can be determined from the relation

$$\cos\theta = - \frac{r\,P_o}{2\gamma} \tag{12}$$

when the surface tension $\gamma$ of the metal or alloy system is known. Once the onset condition is established, the microspray will continue even through the pressure is reduced until the cutoff pressure is reached, when the microspray ceases. The continuation of the microspray

condition at pressures below onset is attributed to the influence of the electrostatic stresses on the liquid surface. Table IV lists onset pressure, cutoff pressures, wetting history, and contact angles calculated from Eq. (12) for an aluminum alloy at 700°C with a nozzle voltage of 8.5 kV. The capillary nozzle employed in these tests was composed of alumina with an orifice radius of $r = 2.5 \times 10^{-3}$ cm. The surface tension of aluminum used in the calculations was taken as $\gamma = 850$ dynes/cm.

TABLE IV

CONTACT ANGLES FOR MOLTEN ALUMINUM MEASURED IN THE TABLETOP POWDER GENERATOR

| Onset Pressure (torr) | Cutoff Pressure (torr) | Nozzle Wetting History | Contact Angle, $\theta$ |
|---|---|---|---|
| 400 | 43 | Unwetted | 143° |
| 252 | 51 | Wetted | 120° |
| 200 | 41 | Wetted | 113° |
| 233 | 46 | Wetted | 117° |

The initial contact angle (143°) is higher than those in subsequent measurements. This is expected, since nozzle surfaces were previously unwetted by the molten aluminum. Measurements after wetting has occurred show reasonable consistency and yield an average value for the contact angle of 116°. Measurements of the contact angle of aluminum on alumina (single-crystal) by the sessile drop technique are reported in the literature over a temperature range of 900 to 1200°C (Ref. 7). The measurements of these investigations were extrapolated to 700°C (shown in Figure 25) in order to compare with our measurements. The extrapolated results yield a value of 143.5°, in good agreement with our estimate of 143° for the previously unwetted nozzle condition.

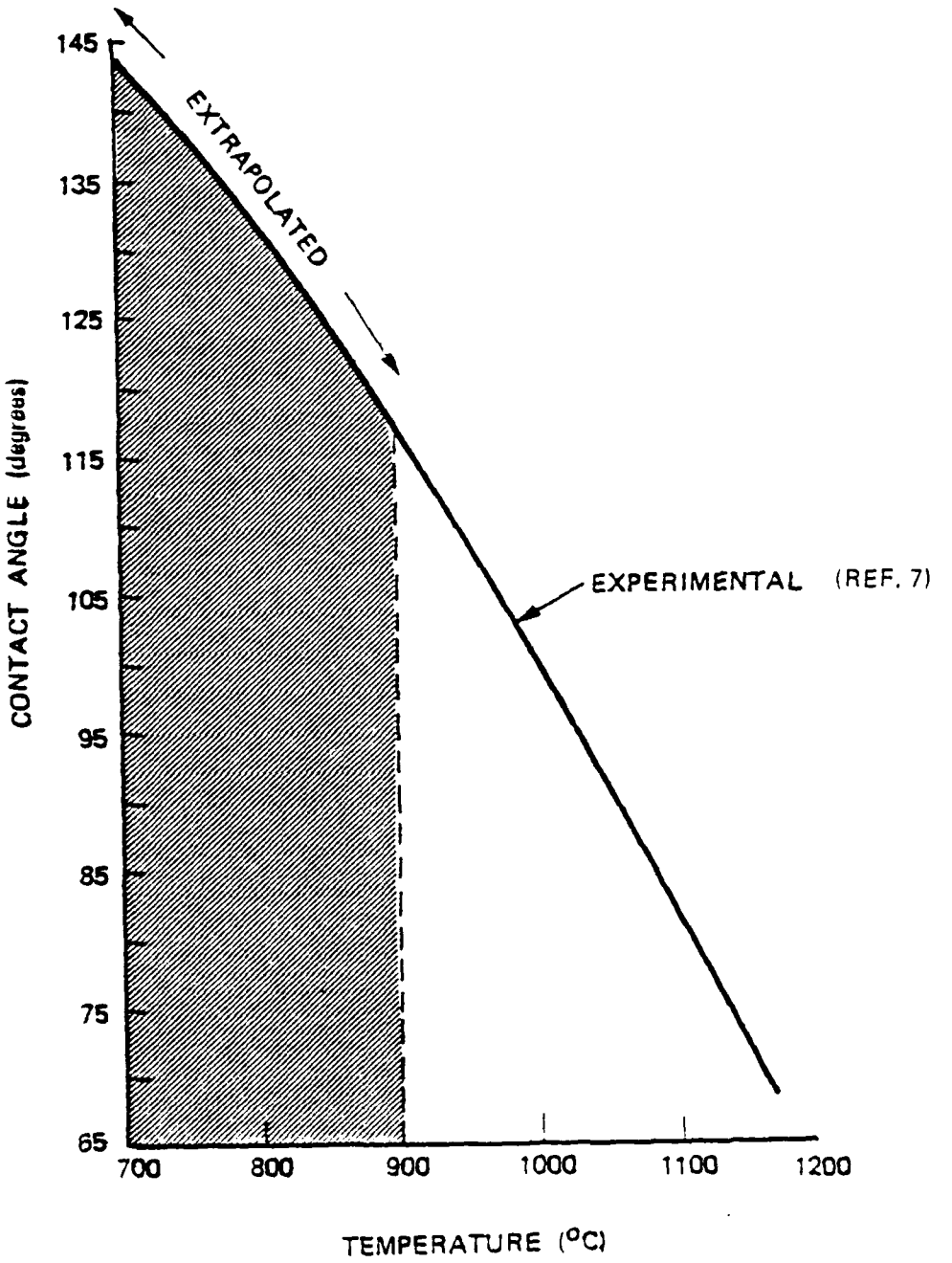


Figure 25. Contact Angle for Aluminum as a Function of Temperature

Table V summarizes the experimental data used to calculate contact angles from Eq. (12) for molten copper, aluminum, and tin with $A\ell_2O_3$ nozzles ($5 \times 10^{-3}$ cm diameter orifice). The alumina data is repeated from Table IV for onset and cutoff pressures for copper. It is based on an average of 21 measurements of onset and cutoff pressures. For tin, average values of onset and cutoff pressures were determined from 10 measurements.

TABLE V

CONTACT ANGLES FOR MOLTEN METALS MEASURED IN THE TABLETOP POWDER GENERATOR

| Metal | Onset Pressure $P_o$ (torr) | Cutoff Pressure $P_c$ (torr) | $\Delta P = P_o - P_c$ | Cos$\theta$ | $\theta$ |
|---|---|---|---|---|---|
| Cu | 587 | 321 | 266 | -0.743 | $138^o$ |
| A$\ell$ | 228 | 46 | 182 | -0.438 | $116^o$ |
| Sn | 166 | 96 | 70 | -0.515 | $121^o$ |

Figure 26 shows a photomicrograph of a copper sessile drop which had solidified inside the $A\ell_2O_3$ ceramic crucible. This drop was used to estimate the contact angle of copper with the aluminum crucible for comparison with the calculated value using the onset pressure or capillary technique. The contact angle measured with the drop was approximately $138^o$, in good agreement with that calculated from Eq. (22). In Table V, the calculated values of the contact angle $\theta$ were made using surface tension values of 1360, 850, and 544 dyne/cm for Cu, A$\ell$, and Sn, respectively.

The pressure difference $\Delta P$ between the onset and cutoff pressures for Cu, A$\ell$, and Sn are also listed in Table V. The significance of the difference is not understood at present, but may be related to the electrostatic pressure exerted on the liquid by the intense fields in the nozzle orifice region.

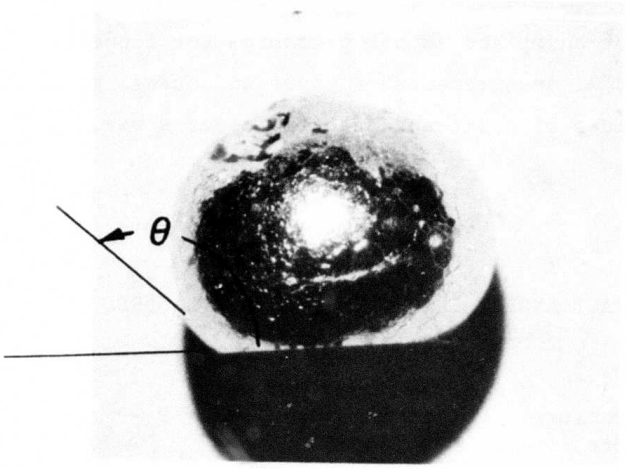


Figure 26. Cu Sessile Drop Used for Contact Angle Measurement

### 2.3.3 CONDITION FOR LIQUID JET FORMATION

The formation of a liquid jet will occur if the velocity of the molten metal exceeds a critical value upon exiting the capillary orifice. This critical velocity is given by (Ref. 8)

$$v_j = 2 \left(\frac{\gamma}{r\rho}\right)^{1/2} \tag{13}$$

where r is the orifice radius. Values of $v_j$ were computed using this expression for molten Cu, Aℓ, and Sn and compared with the calculated fluid velocities from the relation

$$v_o = \frac{K_{eff}(\Delta P)^n}{\pi r^2}$$

discussed in subsection 2.2.3, where $\Delta P$ is assumed equal to the measured onset pressure. The results are listed below:

| Metal | $v_j$ (cm/s) | $v_o$ (cm/s) |
|---|---|---|
| Cu | 489 | 407 |
| Aℓ | 704 | 715 |
| Sn | 342 | 375 |

The results indicate that the molten metal has sufficient velocity to form a liquid jet at the onset pressure, if no voltage were applied to the nozzle. With voltage applied at the onset pressure, the jet does not form in the case of Aℓ and Sn due to the dispersion process occurring at the nozzle tip. For these metals, it is apparent that the electrostatic field can convert the mass throughput into an atomized microspray. This was not observed with the $Fe_{75}Si_{15}B_{10}$ alloy at 10 kV. An undispersed liquid jet was formed. As discussed previously, it is postulated this is due to the high mass throughput at the onset pressure for this

alloy and the high surface tension ($\sim$ 1600 dyne/cm) of the melt. Copper disperses more readily than $Fe_{75}Si_{15}B_{10}$, but the best results were obtained only after nozzles with an orifice radius of $5 \times 10^{-3}$ cm were replaced with nozzles having a radius of $2.5 \times 10^{-3}$ cm to decrease the flowrate.

### 2.3.4 CURRENT-VOLTAGE CHARACTERISTICS

When the microparticle source is tested, the source current is monitored using a strip-chart recorder. The source current is a measurement of the positive charge leaving the source and negative charge arriving at the source. Positive currents contributing to the source current include:

a. Liquid metal ion currents
b. Charged droplet currents
c. Impurity ions emitted from hot surfaces
d. Leakage currents

Negative currents, flowing in the opposite direction, contributing to the recorded source current,are due to secondary electrons generated at electrode surfaces and chamber walls. If the amount of source current due only to the charged droplet emission, $i_d$, could be simply determined, then the average charge-to-mass ratio, q/m, of the droplets could be determined when the mass flowrate is known using the expression

$$\langle q/m \rangle = \frac{i_d}{\dot{m}}$$

It is assumed that the mass loss due to ion emission can be neglected. Once $\langle q/m \rangle$ is known, an average particle size can be calculated. This value of $\langle r \rangle$ can then be used to estimate a mean cooling rate for the distribution.

The component of source current due to droplet emission is difficult to measure in the presence of other currents contributing to the total current. For this reason, we have attempted to define or eliminate current sources other than the charged droplet component.

Positive currents emitted in the form of impurity ions from hot surfaces can be considerably reduced after high voltage conditioning over a period of time. In addition to conditioning, source materials of high purity are selected to reduce the effect of thermionic ion emission. For source temperatures of 1200°C and below, these ion currents are reduced to tolerable levels during each test run after allowing for a suitable conditioning period before the particle beam is initiated.

Leakage currents caused by the increase in electrical conductivity of high voltage insulators at high temperatures were significantly reduced through the proper selection of insulator material. If we specify that the total leakage current from insulators should not exceed 10 μA at 15 kV, then the required insulator resistance is $R = V/I = 1.5 \times 10^9$ ohms. This resistance is easily met by high purity alumina, boron nitride, and beryllia ceramics at temperatures of 500 to 600°C. In terms of cost and ease of handling, we have selected high purity alumina. In addition, the insulators are located on the source in regions where the insulator temperatures do not exceed 500°C.

Ion currents originating from liquid metal surfaces cannot be simply detected at the source - nor can they be eliminated. Diagnostic techniques would have to be implemented that could selectively measure their magnitude in the beam. It is likely that the liquid metal ions produced in the electrostatic spray process are quickly removed from the center of the beam by space charge effects.

Secondary electron currents produced at chamber walls, shutters, etc., can be prevented from arriving at the nozzle tip by applying a negative

bias to extractor electrodes. However, electrons generated at electrode surfaces near the source cannot be simply eliminated.

Source currents, typically 1 to 3 mA, are measured at the output of the high voltage power supply when the background currents are minimized and/or measured. A one megohm resistor is placed in series between the power supply and the source to provide a voltage drop and stability. When the current increases, the voltage drop across the resistor increases, causing a decrease of high voltage at the source in the form of a negative feedback.

The variation of the source current with voltage and pressure is illustrated in Figure 27. The mass flowrate is related to the source feed pressure, but is also affected by the voltage. Two sets of data are shown for the case of Aℓ 4.5%Cu spray from a 50 μm $Aℓ_2O_3$ nozzle and Si spray from a 125 μm graphite nozzle. The aluminum alloy data shows that the current increases with both increasing feed pressure and voltage.

Because of the larger nozzle used in the Si spray, a higher voltage is required to provide a comparable field at the nozzle tip. Since the Si wets the nozzle material, positive pressure was not required, and the liquid silicon flowrate was controlled by capillary feed and the applied voltage. Increasing the voltage increased the current in the steep fashion shown. The silicon flowrate also increased with additional voltage, as determined by a deposition rate process.

## 2.4 DROPLET BEAM AND COLLECTION

### 2.4.1 BEAM CONFIGURATION

Figure 1 of subsection 2.1 shows the general schematic for droplet generation, beam configuration, and particle collection. In the present

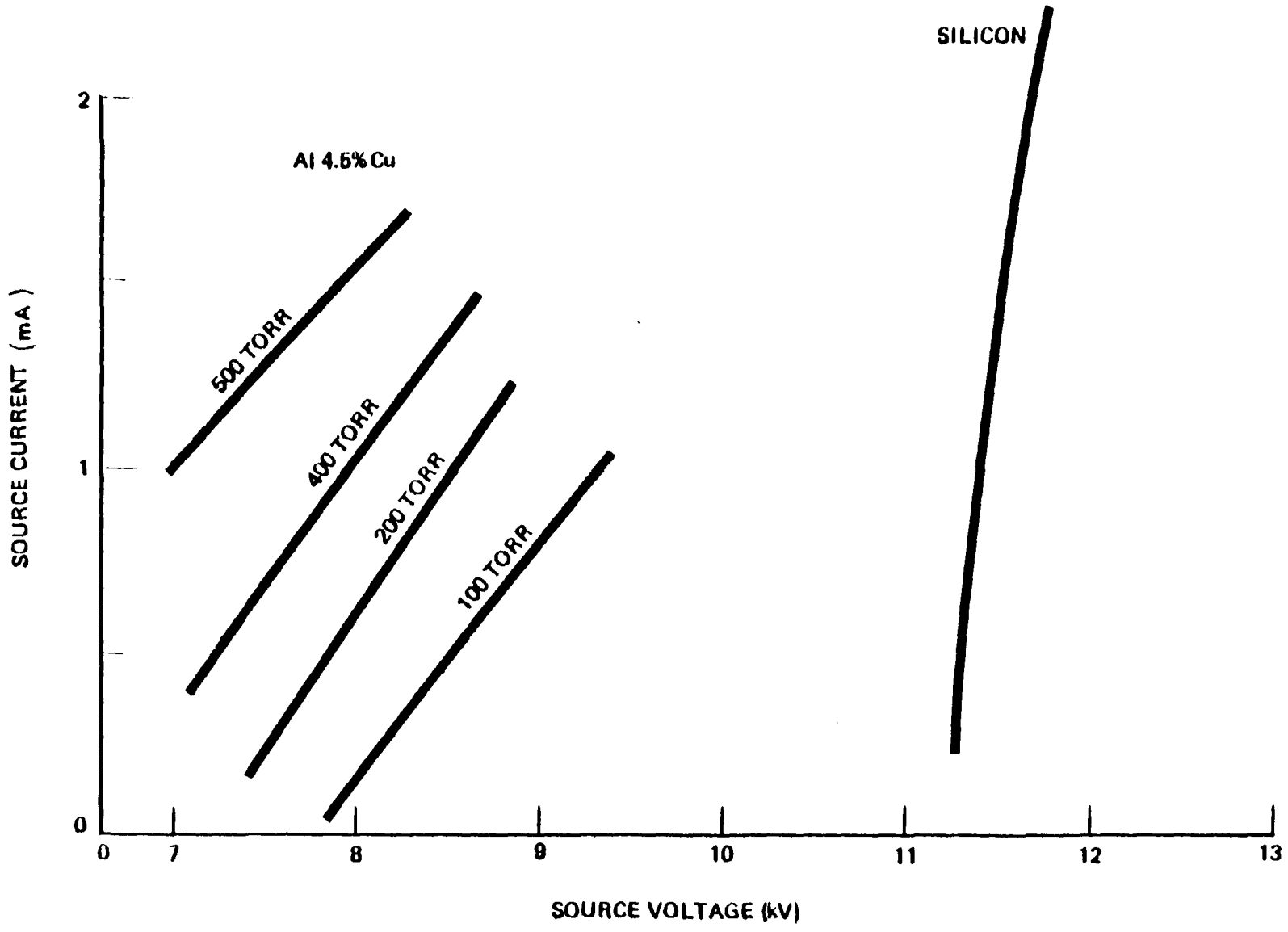


Figure 27. Source Current-Voltage Characteristics for Wetting (Si) and Non-wetting (Al 4.5%Cu) EHD Spray

subsection, beam dynamics and particle interactions will be considered along with various collection schemes. The modes of beam generation for non-wetting molten metals are discussed in greater detail in subsection 2.3. The general appearance of spray for a wetting metal is illustrated in Figure 28. The nozzle typically composed of alumina, beryllia, or graphite is so shaped to produce, with the application of several kilovolts, an electric field in the range of $10^5$ V/cm. These fields are generally sufficient to apply forces to the liquid to produce a liquid spike whose diameter is at least an order of magnitude below that of the nozzle orifice. At the tip of the spike is an intense glow signaling the production of droplets and/or a discharge plasma. The plasma can be composed of microdroplets, ions, and electrons. When the larger droplets pass through the plasma, they interact with the particles which alter their charge. It was found that droplets will absorb electrons from a plasma and the change in charge will depend upon the droplet size, the plasma density, and the time spent in the plasma. This will be discussed in greater detail in the following subsection.

### 2.4.2 DROPLET TRAJECTORY

The droplets travel from the nozzle to the collector during a period called the time-of-flight (TOF). Depending upon the TOF, the droplet size, temperature, and other properties, the droplet could arrive at the collector totally liquid, totally solid, or any combination between the two extremes. Powders are produced when the combination of droplet size and droplet source/collector separation is appropriate to insure solidification in flight by radiation. When the combination is such that little or no solidification has occurred, the droplets are splat cooled at the collector and coatings are formed. For conditions between these two, the partially solidified droplets are generally splat cooled or deformed spheres forming a rough coating whose roughness is dependent upon droplet size. A more detailed description of the degree of solidification and the conditions of the particle flight is given in the next subsection.

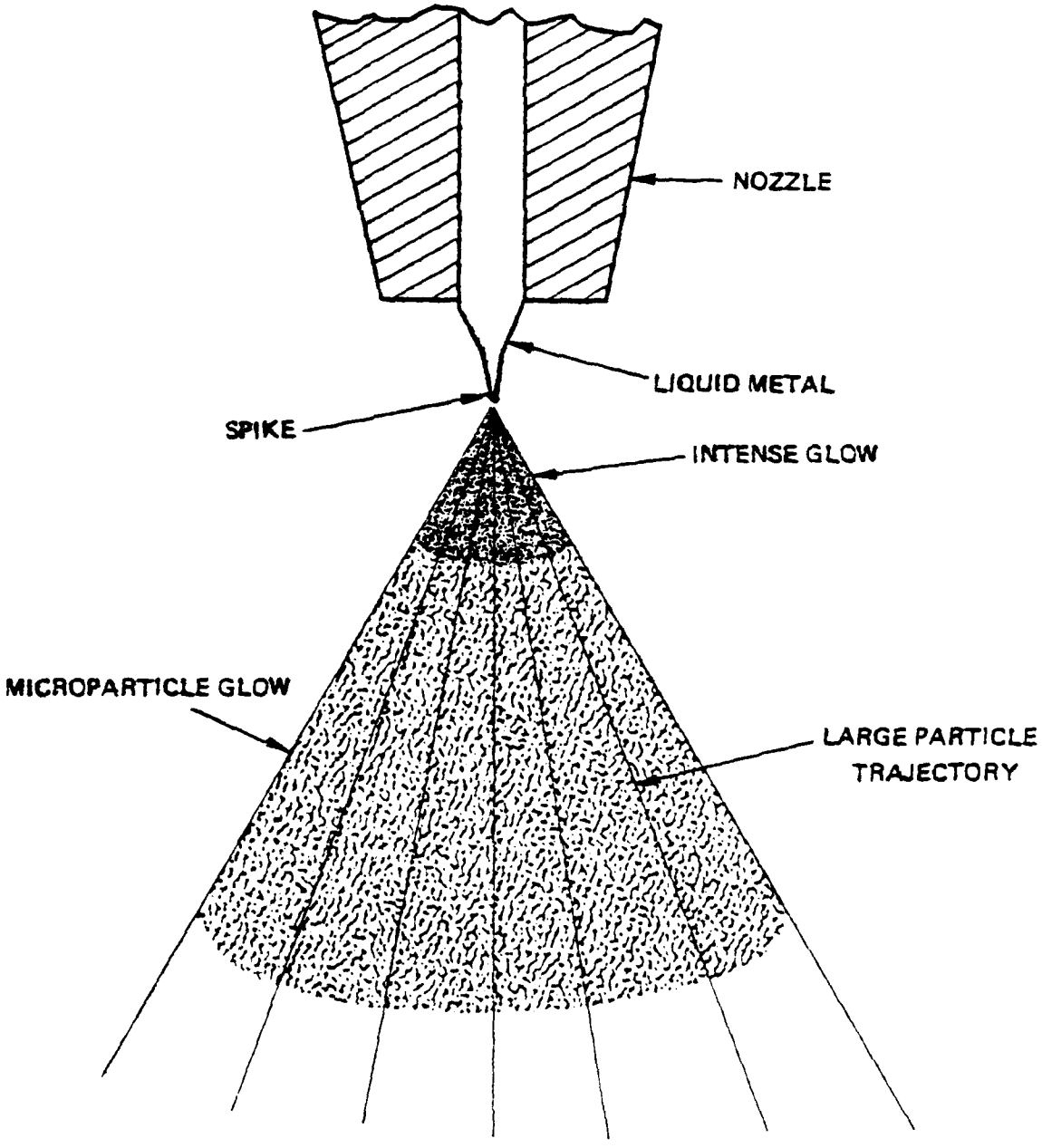


Figure 2-28. Schematic of the Process of Electrohydrodynamic Droplet Generation

The TOF is given by the ratio of the distance of travel to the particle velocity. Assuming no change in charge occurs to the droplet during acceleration, the velocity, v, is determined by the energy equation

$$qV = \tfrac{1}{2} mV^2$$

where q is the droplet charge, V is the applied source voltage, and m is the droplet mass. The velocity for a 10 kV source voltage is typically $10^4$ m/s for droplets having a diameter of $10^{-2}$ μm, 200 m/s for micron size droplets, and 40 m/s for 100 μm droplets. Typical source-to-collector distances for powder collector are 0.5m, and for coating and splat cooling, 0.1m. Thus, TOF for $10^{-2}$ μm droplets are 0.05 ms and 0.01 ms for powder and coating cases, respectively, and for $10^2$ μm droplets, 1.3 m/s, and 2.5 m/s, respectively. These numbers will vary somewhat with various materials, but these generalizations provide the ranges of operation. Detailed calculations are easily made, depending upon the material properties, the applied voltage, and the flight dimensions.

When the particles impact upon the collector, some of the kinetic energy is converted to heat. This heating could remelt a solidified particle or cause partial remelt. In any case, it should be taken into account to determine the conditions of solidification. For example, a droplet could solidify in flight at one cooling rate, only to be remelted upon impact and splat cooled at an entirely different cooling rate. The conversion of kinetic energy into heat which affects the particle was discussed in a previous report (Ref. 4). It will be briefly reviewed in this section for the sake of completeness.

The transformation of kinetic energy into thermal energy of the particle will depend upon the particle properties, spray dynamics parameters such as voltage, and the collector material. In general, the larger the

particle the less the chance for remelt, since the energy of fusion increases with the cube of the radius, and the kinetic energy increases with the three halves power of the radius. In addition, the kinetic energy increases with the applied voltage. But only a fraction of the kinetic energy is transformed to thermal energy and that fraction depends upon the impact surface. Plastic collector materials appear to cause little heating of the particles and virtually no impact distortion as observed with impact upon metal collectors. If we assume all the kinetic energy is converted to thermal energy and absorbed by the particle, then at 10 kV solid particles at the melt temperature having diameters less than 0.35 μm will be remelted upon impact. The small particles observed on plastic type collectors show no impact distortion and so indicate that only a small fraction of the kinetic energy goes into particle thermal energy. It appears that a great deal of the kinetic energy and particle heat goes into distortion of the plastic collectors.

Particle Charge Alteration

An additional deceleration at the collector has been employed to slow down the particles before impact. But it was found that the particles arriving at the collector did not always have the appropriate charge obtained from theory. It was further found that some of the particles were negative, although they all were produced from a positively charged nozzle. A more thorough investigation was performed, and it was determined that charged particles traversing a plasma will undergo alteration of their initial charge state (Ref. 9). The effect is due to capture of electrons in the plasma, near the nozzle tip, mentioned in the previous subsection, and this could result in neutralization and even negative charging.

Appendix A contains a copy of the paper, based upon this investigation and submitted for presentation at the Electrostatic Spraying of Liquids session at the IEEE/IAS 1980 Annual Meeting, September 1980. It can be assumed with favorable results that the droplet charging characteristics can be determined using spherical Langmuir probe theory. Since the positively charged droplets travel at much lower speed than even the slowest electrons, they can be considered at rest with respect to the electron gas. The electrons are attracted to the positive charge and some orbit then escape and others are captured by the sphere. The rate of charge capture will depend upon the particle size and the electron density and temperature. The time taken to completely neutralize a positively charged sphere is inversely proportional to the radius and the electron density. Thus, the larger particles will discharge more rapidly than the smaller ones. For example, a 10 μm aluminum droplet will neutralize in tens of microseconds in the typical plasma generated during operation of EHD sources. Plasma densities and temperatures were determined by Langmuir probe experiments discussed in subsection 2.5.2 These results preclude the use of the charge state of the particle downstream to clearly determine such parameters as the particle size, in order to obtain the cooling rates. Another method will be discussed later. Instead, in application of this phenomena, it is seen that a charged particle fired through a plasma could act as a probe for measuring the plasma electron density and temperature.

Gas Coating During Droplet Production

Of the several species that can generally be found within the residual gases inside the vacuum chamber, the major ones are the molecules of hydrogen and water. While traveling from the emitter to the collector, molten metal droplets may accumulate molecules of gas on their surfaces. The time taken for an Al droplet to acquire only one monolayer of $H_2$ and $H_2O$ molecules will be calculated and this will be compared with the solidification time.

According to Dushman (Ref. 10), the number of gas molecules striking unit area per second inside a vacuum chamber is

$$\nu = \frac{P_T}{(2\pi mkT)^{\frac{1}{2}}}$$

where $P_T$ = chamber pressure (newtons/meter$^2$) due to the gas molecules; m = mass (kg) of a gas molecule; k = Boltzmann's constant = $1.38 \times 10^{-23}$ joules/K; and T = temperature (K) of the chamber gas. In the above equation, it is assumed that all the gas molecules in the chamber are identical. Since this is not the case, therefore, $P_T$ must represent the fraction of the total chamber pressure that is due to a particular gas. According to the percentages estimated in the chamber, we have

$$P_H = 0.1243\ P_T$$
$$P_W = 0.3980\ P_T,$$

where H and W denote hydrogen and water, respectively, and $P_T$ denotes the total chamber pressure. Let $p = 10^{-5}$ torr $= 1.33 \times 10^{-3}$ N/m$^2$ and T = 293K. Also, $m_H = 3.35 \times 10^{-27}$ kg, and $m_W = 3.01 \times 10^{-26}$ kg. Then the above equation yields: $\nu_H = 1.8 \times 10^{19}$ molecules/m$^2$ second, and $\nu_W = 1.9 \times 10^{19}$ molecules/m$^2$ second.

We shall assume that the accommodation coefficient is unity and so all the molecules striking the surface of a droplet adhere to the droplet. Now, the number of hydrogen and water molecules per unit area that constitute a monolayer are, respectively, approximately $4 \times 10^{19}$ and $10^{19}$ molecules/m$^2$. Hence, the times taken to form a monolayer of hydrogen and water, respectively, are:

$$t_H = \frac{4 \times 10^{19}}{\nu_H} \qquad t_W = \frac{10^{19}}{\nu_W}$$

However, since the $H_2$ and $H_2O$ molecules are striking the droplet simultaneously, the time taken to form a monolayer consisting of both $H_2$ and $H_2O$ molecules is

$$t = \frac{t_H \, t_W}{t_H + t_W} = 0.42s$$

How does the above time compare with the solidification time of Aℓ droplets? The solidification time is given by, $\tau = mH/P$, where, m = mass of droplet, H = heat of fusion of droplet, and P denotes the total power released by the droplet through radiation. If it assumed that the total emissivity is unity and that the ambient temperature in the chamber is 293K, then for a spherical aluminum droplet initially at its melting temperature (933K), the solidification time becomes

$$\tau = 3.67 \times 10^{-3} d, \; s$$

where d = diameter of droplet in microns. Typical droplet diameters produced in the chamber are d = 10 microns. For this diameter, $\tau = 3.67 \times 10^{-2}$ second, which is less than one-tenth of the time taken to form a single monolayer of $H_2$ and $H_2O$ molecules. Hence, only a relatively small amount of coating will form on the droplet before it becomes solidified or during the entire time-of-flight. This analysis represents the worst case, i.e., the accommodation coefficients are taken as unity.

### 2.4.3 COLLECTORS AND SAMPLE PREPARATION

The particle collector can be composed of various materials and maintained in different configurations, depending upon the desired results. Figure 29 shows a collector which is a substrate heater module capable of heating to 1300K and holds a substrate as large as 5 cm square (25 $cm^2$). The heating is used to maintain coatings in the liquid state such as Aℓ on Ti (subsection 3.3) or to heat up samples during purification investigations

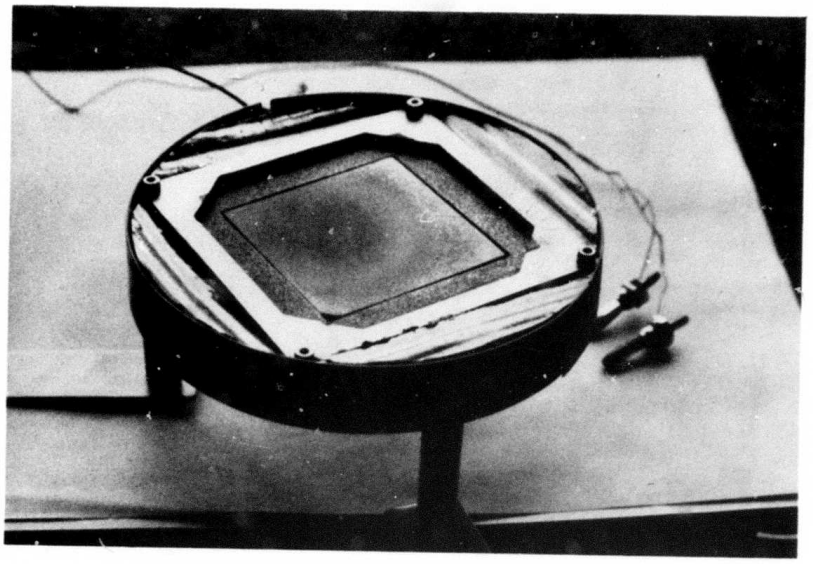

Figure 29. Substrate Mount Collector with Heating Capabilities to 1300K. Substrate size is up to 5 cm by 5 cm.

as described in subsection 2.6. The basic design consists of a structure utilizing two graphite plates with a flat spiral wound resistive heater sandwiched between the two. The temperature is measured by both a thermocouple in the substrate holder and an optical pyrometer observing the sample face. Existing substrate designs and hardware are being modified to accommodate higher temperature operation. In order to effect these changes, Phrasor Scientific, Inc., has invested in a major capital equipment purchase involving a Lepel 2.5 kW Bench Model induction heater unit. The unit recently under test achieved 1200°C at the sample surface using specially designed working coils and the high vacuum feedthrough shown in Figure 30, along with graphite substrate mount (Figure 31). This unit should allow sufficient flexibility to cover a wide range of substrate temperatures up to 1700K, and could also be used in nozzle heating applications.

Various metal substrates such as Aℓ, S.S., Cu, and Ti were used to collect particles. The larger particles were sometimes found to reflect off the substrate and remain distorted in shape. In other cases, splats occur and coatings are made. Metal substrates are much better coating collectors than powder collectors, and good results were obtained in thin film adhesive films, thick films, and sometimes thick coatings. Powders are best collected on plastic type tapes such as replicating tape which dissolves in acetone. Tapes have been coated with a low density of very fine droplets for the study of microparticle rapid solidification.

Collection and Handling of Powders

It has been shown that atomization method by EHD can produce metal powders in the electron-transparent size range (< 1 μm in diameter for Aℓ at 200 keV) (Ref. 3). Methods of collecting and handling this ultrafine materials are being considered so that a representative sample

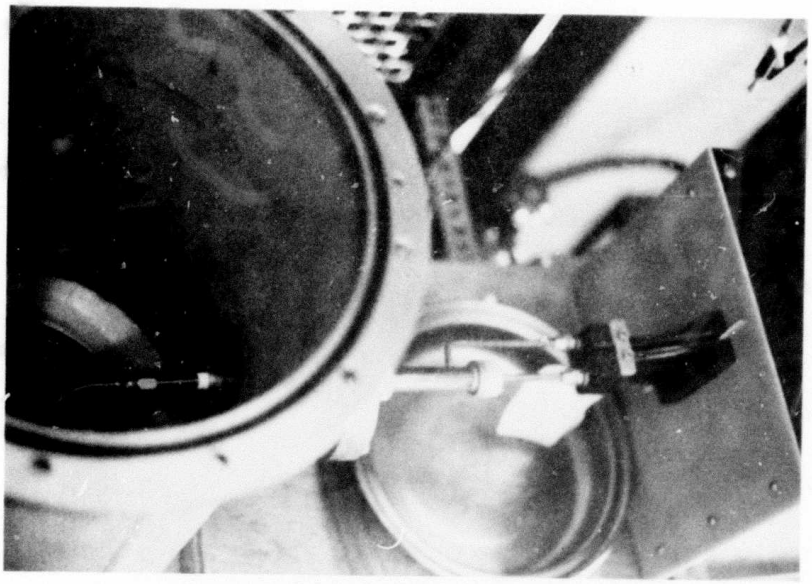

Figure 30. Photograph Showing Induction Heater Transformer (right), Vacuum Feed-through, and Flat Coil

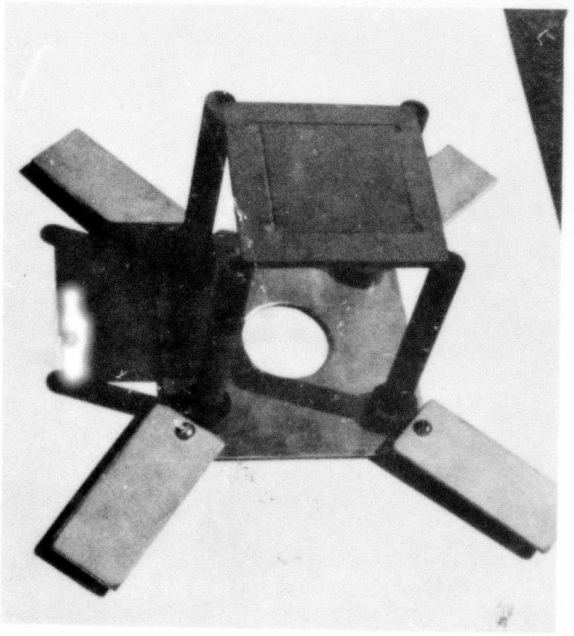

Figure 31. Substrate Mount Made of Graphite and Used with Flat Induction Coil

for transmission electron microscopy (TEM) can be readily prepared. In addition, a technique is discussed for the collection of larger quantities of powder for X-ray analysis.

The method chosen for the TEM investigation involves the direct deposition of the powders on 125 μm thick plastic tape (normally used to prepare electron microscope replicas). The tape is later cut into 3 mm diameter discs and coated on the deposition side with a ~ 200Å film of evaporated carbon (see Figure 32(a) (Ref. 11)). The tape is then dissolved in acetone and the powders remain attached to the carbon film. The film is later rinsed and carefully placed on a 3 mm, 400 mesh copper grid as illustrated in Figure 32(b). An SEM of such a sample usable for TEM is shown in Figure 33, in which submicron particles are discernable.

The advantages of using replicating tape for the collections of these powders are:

a. It is a relatively soft plastic and the powders are easily embedded into it with little or no plastic deformation, if they arrive at the target in the solid state.
b. It dissolves readily in acetone with minimum dimensional change (swelling) and so the carbon films are not disrupted during the dissolution process.
c. It provides a large number of samples of fairly uniform characteristics, a situation rather uncommon in TEM sample preparation.

The same method of collection can be further applied to the preparation of X-ray diffraction specimens, where a substantial amount of material is needed (a few milligrams). One dissolves the pieces of tape with the embedded powders without coating with carbon, and centrifugres the liquid to separate the powders. Using only one tube or vial to successively centrifuge and decant the liquid residue, sufficient material can be gathered for an X-ray sample. An ultracentrifuge necessary for

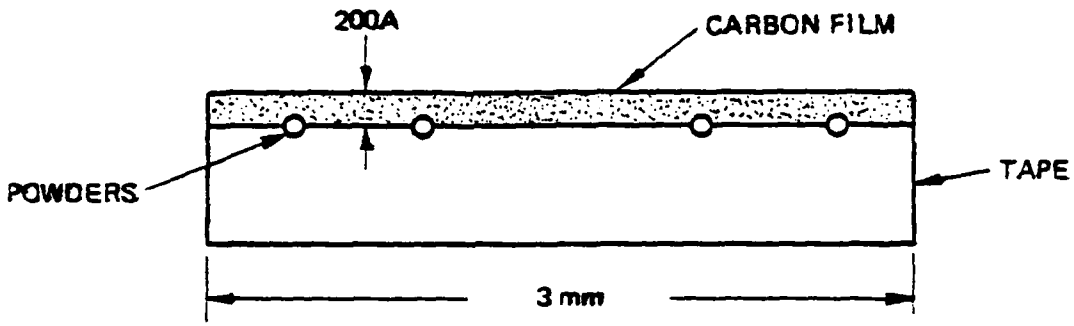


Figure 32(a). Illustration of Carbon Coated Disc Tape

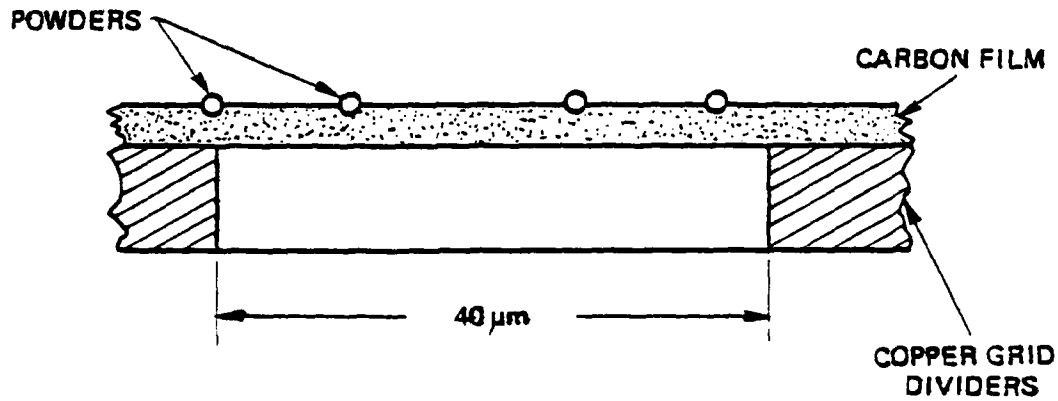


Figure 32(b). The Carbon Film Containing the Powder is Mounted on the Copper Mesh and is Ready for TEM

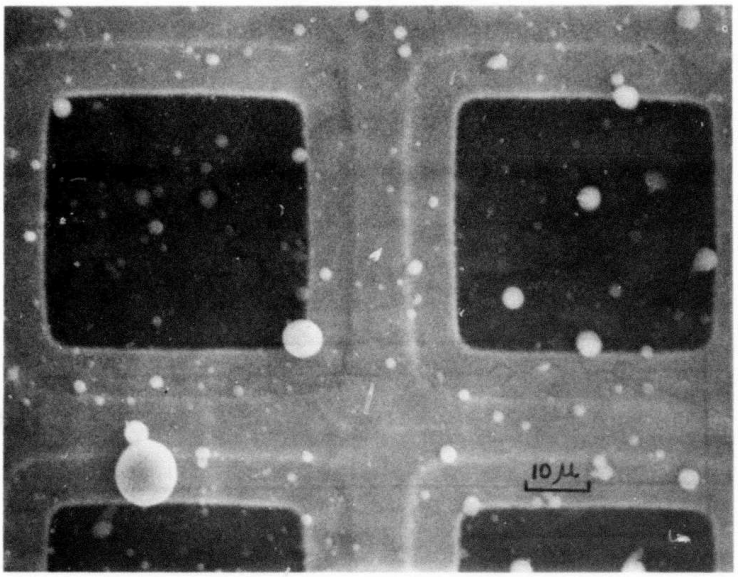


Figure 33. SEM at 1000X of Aℓ 6%Si Powders on a 200Å Carbon Film Mounted on a 400 Mesh Copper Grid

this operation has been obtained and is presently being tested. The instrument is a Beckman Ultracentrifuge capable of attaining 178,000g.

This latter approach will be especially useful when dealing with amorphous metals or dense (high atomic number) alloys, where the range of electron transparency is substantially reduced (e.g., < 1 μm in diameter for Fe-based alloys), and one must turn to ultrahigh voltage microscopy or X-ray diffraction to obtain information on the degree of crystallinity. Furthermore, since lattice parameter measurements via electron diffraction are not accurate enough for the determination of increases in solute supersaturation in the primary phase, one must turn to X-ray diffraction for this information.

## 2.5 RAPID SOLIDIFICATION AND COOLING RATES

It was initially evident that, since EHD could be used to produce fine powders, it could also be a way of making amorphous powders in a vacuum. Calculations showed that micro-size droplets of a wide variety of alloys would have sufficiently high cooling rates to assure that their structure would be amorphous. Both TEM and X-ray diffraction techniques have been used to demonstrate that fine powders produced by EHD processing are amorphous (see subsection 3.2).

Rapid cooling during solidification has also shown important influences upon segregate spacing and the distribution of secondary phases of crystalline structures. It was also found that rapid solidification promotes undercooling to nucleation and can produce metastable crystalline phases and increased solid solubility of solute elements in the base metal. Solute distribution and the morphology of dendrites are affected by undercooling prior to solidification of crystalline structures. Solute rich dendritic cores have been correlated to undercooling before nucleation. Since undercooling affects the morphology of dendritic structures, it then becomes dificult to correlate

dendrite arm spacing with cooling rates. In these cases, leaf-like dendrites tend to become more cylindrical in structure at low undercooling. Beyond critical undercooling, a sharp decrease in grain size occurs with the appearance of a more spherical grain structure.

Increasing cooling rates have been known to extend solid solubility of solute elements and metastable phase formation as evident in the measurement of lattice spacing using X-ray diffraction. Of interest here is the increase solubility of, for example, silicon in aluminum with increasing cooling rates. Such a study could aid in correlating cooling rates with reported solid solubility to determine relationships between process variables, cooling rates, and crystalline structure. The Aℓ-Si alloy study was launched for these reasons. This study is discussed briefly in subsection 3.1.

### 2.5.1 COOLING RATES AND SOLIDIFICATION

As the droplet travels the distance between source and collector, the flight distance, they will lose energy by radiation, assuming no convective cooling gas is present. The droplets will arrive at the collectors either liquid, partially solid, or completely solid, depending upon the material properties and operational conditions. To assure complete solidification before collection, the source nozzle is usually maintained close to the melt temperature, small droplets are generated, and the flight distance is maximized. For particles collected in a complete molten state used for splat cooling, the flight distance is minimized, large droplets are produced, and the source superheated so that time-of-flight cooling does not result in appreciable solidification. Some of the equations and curves to help determine the desired operating conditions will be reviewed here.

If the initial temperature of the droplets is greater than their melting temperature, they will approach solidification in two stages. First,

the droplet temperature will fall from its initial value, $T_1$ to the melting temperature, $T_M$ ($T_M < T_1$), and the cooling rate during this temperature drop is

$$\frac{dT}{dt} = \frac{-P_R}{mC_p} \tag{13}$$

where $P_R$ = power lost by radiation, m = mass of a droplet, $C_p$ = specific heat of droplets. Here

$$P_R = A\varepsilon\sigma\ (T^4 - T_o^4) \tag{14}$$

where A = surface area of a droplet, $\varepsilon$ = total hemispherical emissivity of a droplet, $\sigma$ = Stefan-Boltzmann constant = $5.67 \times 10^{-8}$ watts/meter$^2$ K$^4$, T = droplet temperature, and $T_o$ = ambient temperature. Since T is time dependent, therefore, dT/dt will also be time dependent. Of particular interest is the value of dT/dt when $T = T_M$. Since $m = (\pi d^3/6)\ \rho$, where $\rho$ and d are the droplet density and diameter, respectively, and $A = \pi d^2$, the absolute value of dT/dt is then given by

$$\frac{dT}{dt} = \frac{6\varepsilon\sigma\ (T_M^4 - T_o^4)}{C_p \rho d} \tag{15}$$

Table VI shows several liquid metal parameters, including $T_M$, $C_p$, and $\rho$, for Aℓ, Cu, Fe, and Si. Figure 34 shows dT/dt as a function of d for these same four metals, where $\varepsilon = 1$ and $T_o = 293$K.

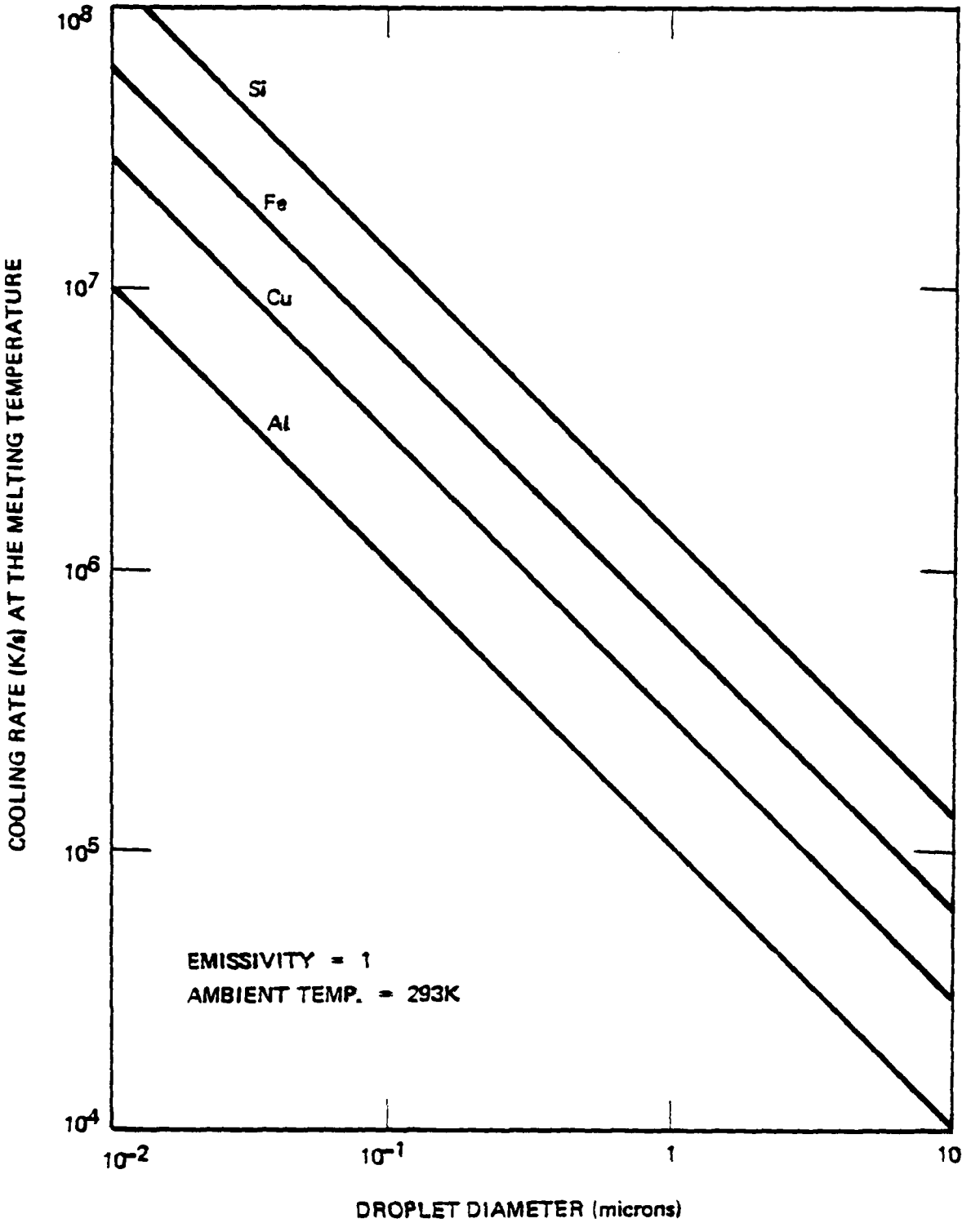


Figure 34. Cooling Rate versus Droplet Diameter for Radiative Cooling

TABLE VI

LIQUID METAL PARAMETERS

| Metal | Melting Temp. $T_M$ (K) | Specific Heat $C_p$ (J/kg K) | Density $\rho$ (kg/m$^3$) | Heat of Fusion H (J/kg) | Surface Tension $\gamma$ (N/m) | Thermal Conductivity k (watts/m K) |
|---|---|---|---|---|---|---|
| Aℓ | 933 | 1046 | 2382 | $3.934 \times 10^5$ | 0.84 | 237 |
| Cu | 1356 | 494 | 7900 | $2.051 \times 10^5$ | 1.30 | 398 |
| Fe | 1808 | 825 | 7000 | $2.720 \times 10^5$ | 1.70 | 80 |
| Si | 1693 | 879 | 2400 | $1.660 \times 10^6$ | 0.73 | 84 |

After reaching the melting temperature $T_M$, the droplets will begin to solidify. During solidification in this simplified analysis, the temperature will remain constant at $T_M$, and the total energy released per droplet will be:

$$E_T = P_R t_S,$$

where $t_S$ = time taken for a droplet to become completely solidified, i.e., the solidification time. It is also true that

$$E_T = mH,$$

where H = heat of fusion of the droplet. Consequently, the solidification time is given by

$$t_S = \frac{mH}{P_R} \tag{16}$$

where $P_R$ is given by Eq. (14), in which $T = T_M$.

When a droplet arrives at the collector, it will be in one of the following final states: (1) liquid, (2) partially solidified, (3) completely solidified. The final state of a droplet depends on its composition, diameter, initial temperature, velocity, and the distance between source and collector. Of primary interest is the determination of this final state, and a procedure for doing so is given below.

Determining the final state of a droplet is made easier by the fact that the droplet diameter is small enough so that the droplet experiences Newtonian cooling, i.e., no temperature gradients occur within the droplet, so that it cools uniformly throughout. The criterion that must be satisfied is that the Biot number, hd/2k, must be less than 0.01. Here, h = heat transfer coefficient at the surface of a droplet, and k = thermal conductivity of the droplet. For radiative cooling only, h is given by

$$h = \varepsilon\sigma\ (T + T_o)(T^2 + T_o^2) \tag{17}$$

Table VI shows the values of k for the metals under consideration. The maximum Biot number that can be expected for these metals will correspond to T $\approx$ 2000K, k $\approx$ 80 watts/meter K, and d = 10 microns = maximum droplet diameter under consideration. Letting $T_o$ = 293K and $\varepsilon$ = 1, we then obtain hd/2k = $3.3 \times 10^{-4}$, which is well below 0.01.

Let $t_M$ denote the time taken for the droplet temperature to fall from its initial value $T_1$ to the melting temperature $T_M$, and let $t_F$ denote the time of flight, i.e., the time taken for a droplet to go from the source to the collector. From Eqs. (13) and (14),

$$t_M = \frac{C_p \rho d}{24\varepsilon\sigma T_o^3}\left[\ln\frac{(T_M + T_o)(T_1 - T_o)}{(T_M - T_o)(T_1 + T_o)} + 2\tan^{-1}\left(\frac{T_M}{T_o}\right) - 2\tan^{-1}\left(\frac{T_1}{T_o}\right)\right] \tag{18}$$

and

$$t_F = L\left(2V\frac{q}{m}\right)^{-\frac{1}{2}}\ . \tag{19}$$

In Eq. (19), L = distance between source and collector, V = potential difference through which the charged droplets are accelerated, and q/m = droplet charge-to-mass ratio, which, if no charge alteration occurs, is

$$\frac{q}{m} = \frac{6\ (2\gamma\varepsilon_o)^{\frac{1}{2}}}{\rho d^{3/2}} \tag{20}$$

where $\gamma$ = surface tension of the droplets and $\varepsilon_o$ = permittivity of free space = $8.854 \times 10^{-12}$ farad/meter. It can be shown that the degree of solidification, S, of a droplet when it arrives at the collector is given by

$$S = \frac{t_F - t_M}{t_S} = \frac{t_F}{t_S} - \frac{t_M}{t_S} \tag{21}$$

Thus:

If $S < 0$, the droplet will be in a liquid state;

If $0 < S < 1$, the droplet will be S x 100 percent solidified;

If $S > 1$, the droplet will be completely (100%) solifified.

Figure 35 shows a graph of the quantity, $(1/L)(t_F/t_S)$, as a function of the droplet diameter, for Aℓ, Cu, Fe, and Si, and Figure 36 shows a graph of the ratio, $t_{M/}t_S$, as a function of the initial droplet temperature, $T_l$, for the same four metals. In calculating these curves, it was assumed that $\varepsilon = 1$, $T_o = 293K$, and V = 10 kV. From these two figures, it is possible to determine the value of S given the particular metal, droplet diameter, source/collector separation, and initial droplet temperature. Thus, given the droplet metal, diameter, and source/collector separation, one can determine the ratio $t_F/t_S$ from Figure 35, and given the initial temperature, one can determine the ratio $t_M/t_S$ from Figure 36. The value of S can then be readily calculated from Eq. (21).

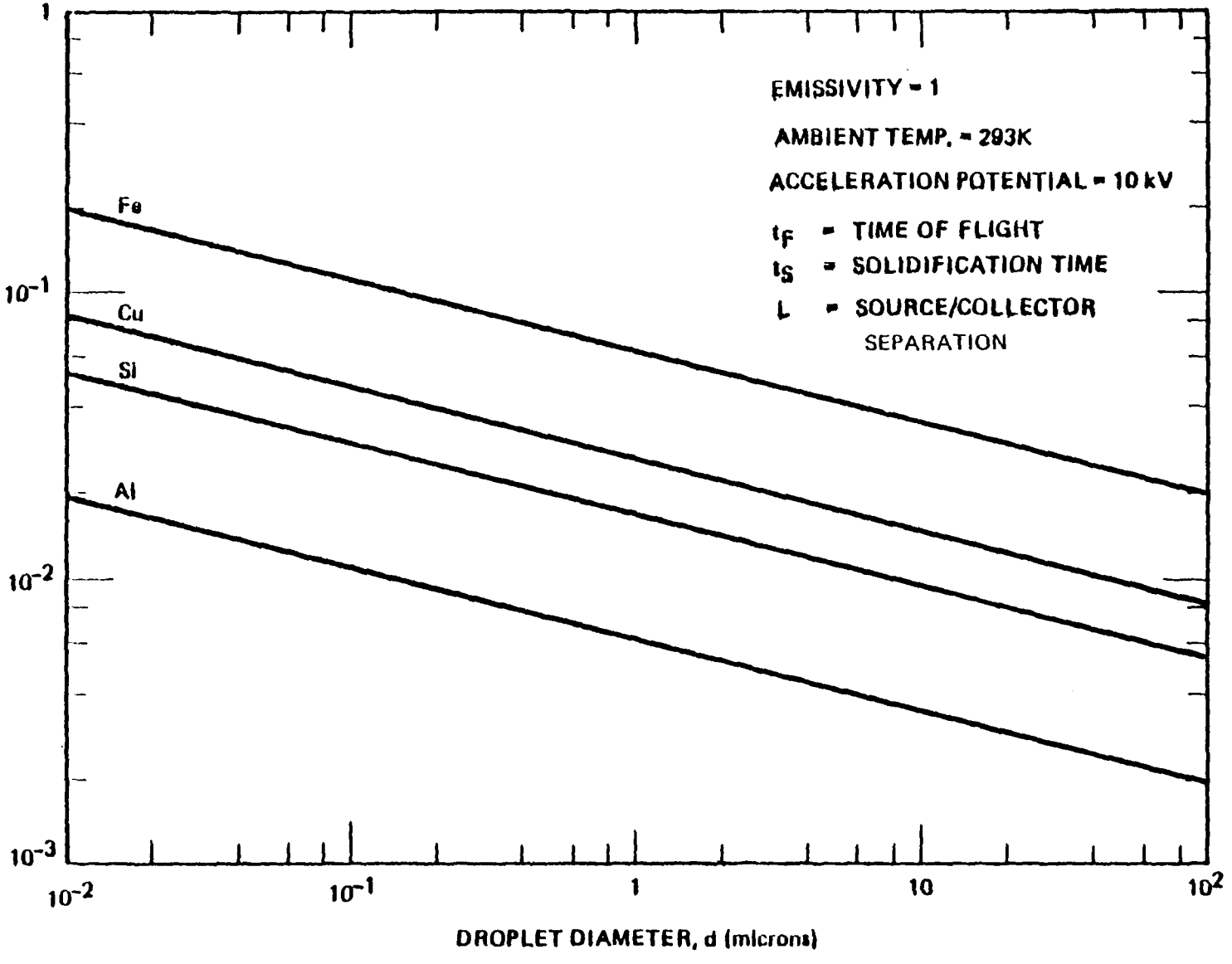


Figure 35. Plot of $(t_{,,}/t_{,,})/L$ versus Droplet Diameter

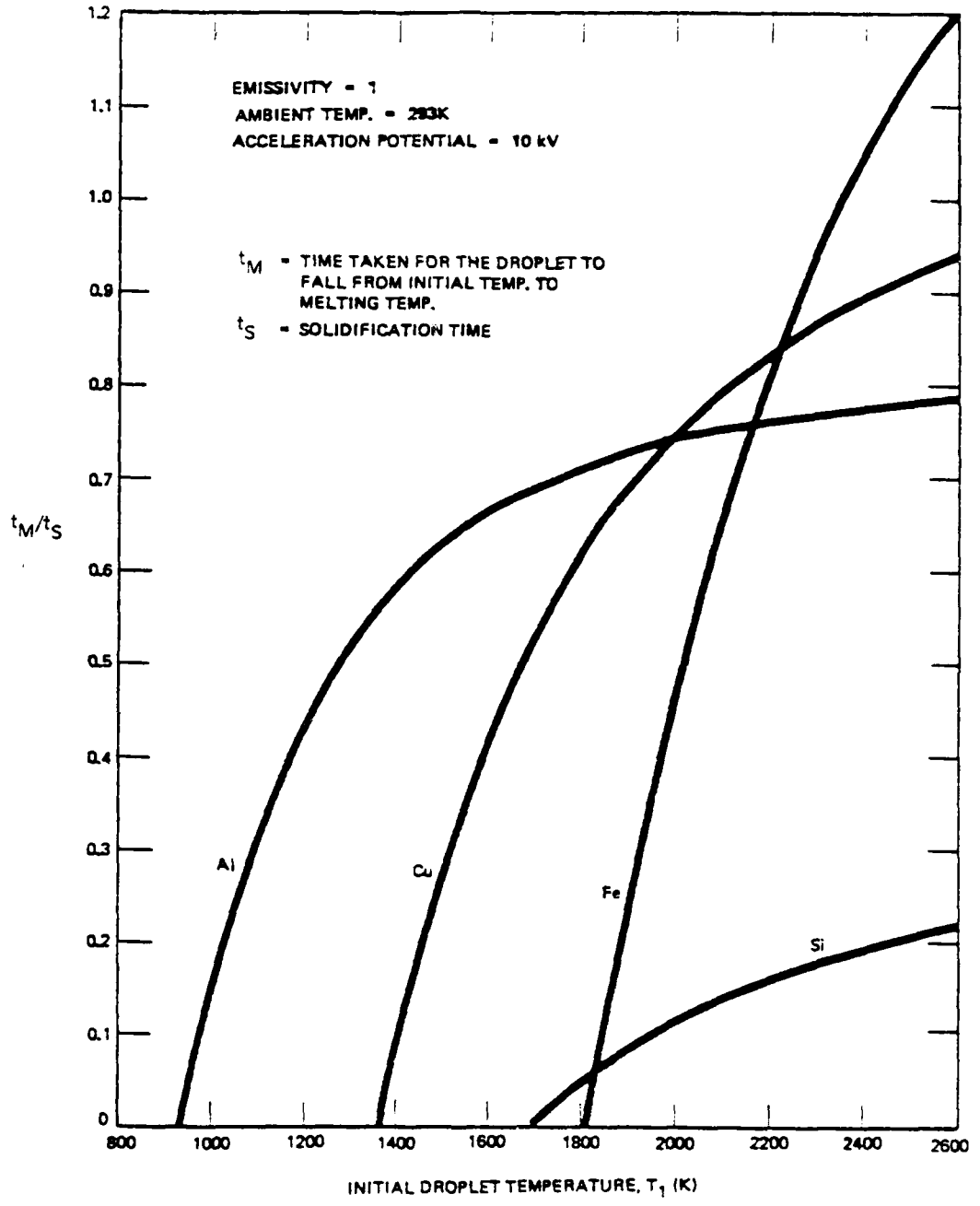


Figure 36. Plot of $t_M/t_S$ versus Initial Droplet Temperature, $T_1$

For example, consider a 10 micron diameter Aℓ droplet that is initially at 1100K and let L = 10 cm. From Figure 35, $(1/L)(t_F/t_S) = 3.5 \times 10^{-3}$ $cm^{-1}$, so that, $t_F/t_S = 3.5 \times 10^{-2}$, and from Figure 36, $t_M/t_S = 0.325$, therefore yielding S = -0.29. Hence, the droplet will be in the liquid state when it arrives at the collector. This would be a good candidate for splat cooling. If, however, L = 1 meter, then we see that S = 0.025, and the same droplet would then be 2.5 percent solidified on reaching the collector, still a likely candidate for splat cooling. Finally, consider a 0.1 micron diameter Fe droplet that is initially at 1900K and let L = 20 cm. Then, $S = 1.1 \times 10^{-1} \times 20 - 0.25 = 1.95$, so that, in this case, the droplet will be completely (100%) solidified on arriving at the collector. This would be a useful condition for making powders.

However, if one wished to determine the optimum conditions for making powders or splats, a slightly different approach can be taken using this method. For example, suppose one desires to splat cool 10 μm Aℓ droplets on a surface 10 cm away from the source. For zero percent solidification, one could determine the initial droplet temperature, or the temperature selected for the source nozzle. From Figure 35, for a 10 μm droplet of Aℓ $(1/L)(t_F/t_S) = 3.5 \times 10^{-3}$. Using the value of L given above and S = 0, then from Eq. (21) one obtains $(t_M/t_S) = 0.035$. From Figure 36, $T_1$ = 948K so the nozzle should therefore be operated only 15K above the melting temperature of Aℓ. On the other hand, if one wanted iron powders of $10^{-1}$ μm diameter, generated at the melting temperature, and 100% solidified, what distance is required? Since the solidification time is to be minimized, then $t_M = 0$, and from Eq. (21), $(t_F/t_S) = 1$. From Figure 35, a $10^{-1}$ um Fe particle gives $(1/L)$ $(t_F/t_S) = 1.1 \times 10^{-1}$. Therefore, solving the above two equations gives L = 9.09 cm as the required distance for 100% solidification.

There yet remains the question as to whether powder collection requires 100% solidification or splat cooling, 0% solidification. Some fraction

of the particle kinetic energy is converted into heat upon impact, as discussed earlier. This, depending upon particle size and velocity and the substrate material, can result in the remelting of a partially solidified particle. Nevertheless, it is possible that a 50% solidifield particle having a solid shell may continue solidifying on the substrate surface by radiation heat transfer alone, or at least primarily. The solidification time would then be longer than the time-of-flight, yet undistorted powders might be collected. It is not known how much below the 100% solidification level that undistorted particles can be collected. A determination can be made by examining a wide range of particles to observe the largest size spherical powder. For example, suppose powders of Cu collected at 50 cm were examined and 50 μm particles were found to be the largest spheres. Droplets larger than this are found to be splatted and so distorted. From Figure 35, the value of $(1/L)(t_F/t_S) = 10^{-2}$ and so $(t_F/t_S) = 0.5$. If the droplet initial temperature was 44K above the melting point, then from Figure 36, at $T_l = 1400K$, then $(t_M/t_S) = 0.1$. Using Eq. (21), we find the value of $S = 0.4$, which means that droplets 40% solidified complete the rest of their solidification at the collector.

Similar considerations can be made concerning splat cooling and the production of coatings. These considerations can have a profound effect upon the experimental parameters selected for various operating conditions in the production of powders and coatings. This helps to extend the capabilities of the Tabletop Powder Generator beyond the stringent conditions previously considered limitations.

### 2.5.2 PROBES

To determine cooling rates and particle sizes generated, several probes were examined, tested, and considered for incorporation into the system. Time-of-flight techniques originally considered for determination of

particle size distribution were found to give disappointing results. The currents arriving at the TOF collectors were too low and did not correlate with the measured source currents. It has since been found that droplets passing through the plasma just outside the nozzle experience charge alteration, particularly for the larger droplets (discussed in subsection 2.3.2). Thus, the charge at the collector is not indicative of the particle size or the charge attained during the droplet generation process.

Langmuir Probe

A Langmuir probe was fabricated and installed in the chamber to measure current-voltage characteristics from which electron temperatures and densities of the plasma in the droplet beam were deduced. Interest in the determination of the electron density and temperature was motivated by the observed alteration of charge on droplets when traversing a plasma. This was discussed in subsection 2.4.2 and examined in detail in Appendix A (Ref. 9).

The Langmuir probe has a sensitive area of $8 \times 10^{-2}$ $cm^2$ which is surrounded by a metal shield to minimize the deposition of the droplets on the surface of the probe. It can be traversed axially and radially in the chamber to measure the geometrical distributions of electron density and temperature in the chamber. A voltage was applied to the probe and the current versus voltage was plotted on an X-Y recorder.

Under the present operating conditions, both the characteristic dimension of the probe and the sheath thickness near the surface of the probe are estimated to be much smaller than the electron mean free path in the chamber. The electron current density, j, as a function of the probe potential then can be expressed as

$$j = \tfrac{1}{4} eNv \exp\left(\frac{-eV}{kT}\right), \qquad (22)$$

where e is the electronic charge; N the electron density of the plasma; v, electron velocity; V, probe potential with respect to plasma potential; k, the Boltzmann constant; and T, electron temperature. The electron energy distribution in the plasma is assumed to be Maxwellian. Taking logs and differentiating with respect to V, we have, from Eq. (22)

$$\ell nj = \ell n(\tfrac{1}{4}eNv) - \frac{eV}{kT}, \tag{23}$$

$$\frac{d(\ell nj)}{dV} = \frac{-e}{kT} . \tag{24}$$

A straight line is obtained by plotting $\ell nj$ against V. The electron temperature can then be calculated from the slope of the straight line by using Eq. (24). When V is equal to zero, then the probe potential is equal to plasma potential, the relation Eq. (22) should suddenly change into a less steeply sloping function. The kink in the curve indicates where the electron current density can be expressed as

$$j_o = \tfrac{1}{4}eNv. \tag{25}$$

Therefore, N can be obtained by knowing $j_o$ and v in Eq. (25). The value of v can be calculated by using the expression

$$v = \left(\frac{8kT}{\pi m}\right)^{\frac{1}{2}}$$

where m is the mass of the electron.

A typical result of the measurement is depicted in Figure 37. The electron density and electron temperature, taken from similar data, are

$$N = 1.01 \times 10^{13}\ m^{-3}$$

$$T = 5.62 \times 10^{5}\ K = 48.4\ eV.$$

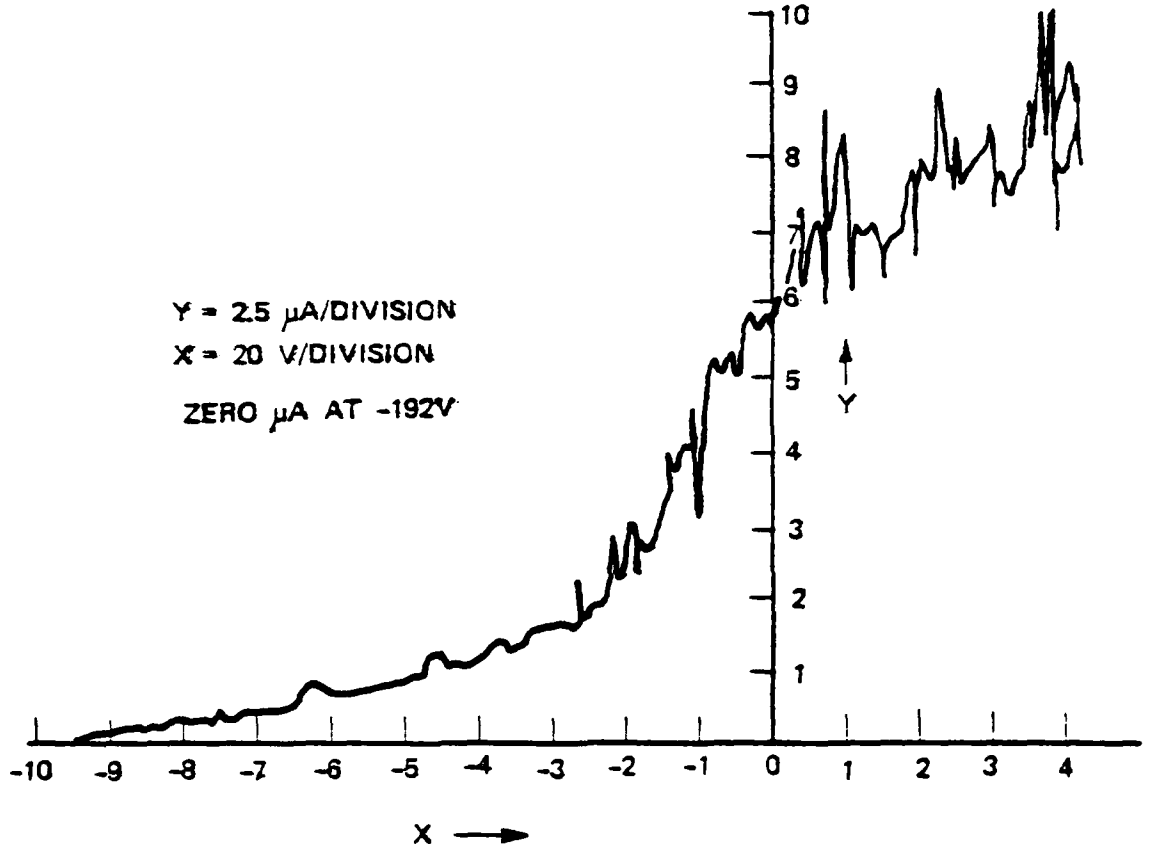


Figure 37. Current-Voltage Characteristics for Langmuir Probe Measurement

These measurements of the electron densities and temperatures in EHD beams are of sufficient magnitude to account for large alteration of droplet charge (Ref. 9 and Appendix A).

Particle Count Probe

A new commercial probe made by Extranuclear Corporation is being tested in our laboratory. It is a particle count device utilizing surface ionization as a method to generate an electrical signal when a heated wire is bombarded by a particle. There are several elements that will be ionized on a heated surface and be emitted in the presence of an electric field. These elements are commonly found in virtually all metallic and dust particles. The probe was developed to measure dust particles in air, but we determined that it could be used to detect metallic particles with only trace amounts (a few PPM) of the alkali metals, aluminum, etc.

A laboratory test of this probe was made during a run spraying Aℓ (Aℓ 4.5%Cu). Approximately 8000 counts per second were measured at a thin wire which indicated that about $10^8$ or $10^9$ total particles per second were generated. This is well within the numbers calculated, considering particle sizes generated and mass flowrates obtained. Figures 38(a) and (b) are photographs of the probe head and the electronic controller. The probe has a $1.3 \times 10^{-2}$ cm diameter wire exposed by a 3 mm orifice. Work on this technique as a standard diagnostic tool will continue.

Deposition Rate Probe

A Sloan Digital Thickness Monitor is being evaluated for use in measuring deposition rates and determination of throughput. The instrument is an all solid state model used to measure vacuum deposition of thin

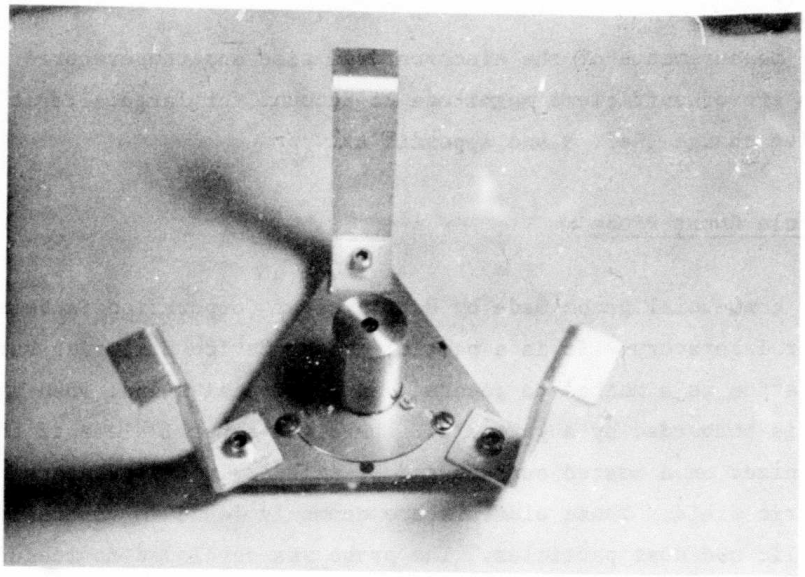

(a)

(b)

Figure 38. Particle Count Probe Head (a) and Electronic Controller (b)

films. The change in period on a sensor crystal, resulting from deposition of material, is measured and, using the material density, the film thickness is determined. The crystal is mounted in a sensor head containing a hermetically sealed electronic oscillator to operate the crystal. The instrument provides a continuous signal proportional to the thickness deposited or, for our purposes, the mass deposited per unit area. The instrument has thermal and capacity (maximum reading) limitations which must be overcome to be a useful instrument in the Engineering Model. We are presently testing this deposition gauge and examining methods to adapt it to measure droplet mass flowrate. Results will be discussed in the next report.

A combination of the particle count and deposition rate probe will be used to measure the particle count rate, to determine the particle distribution, and to measure the mass deposition rate. The ratio of mass deposition rate to the particle count rate will provide the average particle mass and, therefore, the particle size. With the determination of the average particle size and the distribution, which could be obtained using the count rate meter discrimination level, the entire population will be known. The further exploration of this technique will be made with the development of the Engineering Model. The advantage of using these probes is that the uncertain particle charge is not a parameter used in the measurements..

## 2.6 PURIFICATION STUDIES

### 2.6.1 BACKGROUND

During the process of droplet source development as discussed previously, it was observed that materials heated to high temperatures emitted charged particles. When an electric field was applied to the heated surface, currents were generated which increased with the voltage and

with the temperature of the surfaces. It was also noted that the currents decayed with time, indicating a diminishing of the source of the current. During one series of tests at high temperatures, most of the current flowed between the droplet source body and the extractor electrode mounted directly in front of the source (see Figures 5 and 6). The initial current was in the range of 500 μA when the source was maintained close to 1100°C with an applied voltage of 10 kV. After a couple of hours, the current dropped to 50 μA. During another series of tests at 10 kV, the current went from nearly 400 μA at a temperature of 1100°C to 10 μA when the temperature dropped to 800°C. Thus, the current appears to depend upon the temperature, the applied voltage, and time exposed to the field.

### 2.6.2 TECHNICAL DISCUSSION

Emission of ions has been studied for many years, going back to the work of J. J. Thomson in 1908 who observed atomic mass 27 ions (aluminum) emitted from heated platinum (Ref. 12). Lloyd P. Smith, in 1929, observed ions of sodium, potassium, aluminum, and molybdenum itself emitted from a heated molybdenum surface (Ref. 13). In the late twenties and early thirties, Langmuir and co-workers did an extension study of the surface ionization of cesium on tungsten, a phenomenon closely related to ion emission from heated solids (Ref. 14). Dobrezow showed the effect of electric fields on surface ionization analogous to the Schottky effect in thermionic electron emission (Ref. 15). Much more recently, field effects were calculated by Hiskes and Karo in an attempt to explain unexpectedly high surface ionization production of $H^-$ ions at cesiated surfaces (Ref. 16).

Emission of ions from non-metals also has been reported. Blewett and Jones, for example, made a summation of the emission of alkali ions from a variety of aluminosilicates such as β-eucryptite, β-spodumene,

and other minerals (Ref. 17). R. G. Hills and P. Gibbs have studied the impurity ion emission from quartz (Ref. 18).

The ions can be emitted from the surfaces of heated solids by thermal excitation or by the influence of a high electric field at the surface. The ion emission phenomenon observed is undoubtedly due to the interaction of both these mechanisms. It is interesting to note that, in the references listed above, no data were reported on the effects of "high" surface fields involving the application of large potentials, say V > 1000 volts. Certainly, for high surface fields, emission is expected to be enhanced above that for thermionic emission alone. This area of ion emission, and in particular from semiconductor surface, has not been sufficiently explored.

The fact that the degree of ionization can be influenced by the application of high surface fields is known. The Saha equation relating the ratio of the number of ions $n^+$ and atoms $n^o$ in "zero" field leaving a surface is

$$\left(\frac{n^+}{n_o}\right)_0 = \frac{\exp}{2}\left[\frac{-e(I-\phi)}{kT}\right] \tag{26}$$

where, I is the ionization potential of the emitted ion; $\phi$ is the work function of the surface; k is the Boltzmann constant; e is the charge on the electron; and T is the absolute temperature.

The modified expression from Ref. 15, taking into account the application of a field, E, at the surface is given by

$$\left(\frac{n^+}{n^o}\right)_E = \left(\frac{n^+}{n^o}\right)_0 \exp\frac{(ex_oE)}{kT} \tag{27}$$

where, $(n^+/n^o)$ is the value of the ratio without an applied field; E is the surface electric field; and $x_o$ is the distance from the surface

where ionization takes place, with reported values on the order of $10^{-6}$ cm. After substitution of Eq. (26) in Eq. (27), the exponential term is given by

$$\frac{-e}{kT} [(I - x_o E) - \phi] \tag{28}$$

Thus, the electric field effectively reduces the ionization potential by an amount given by the term $x_o E$. A lower effective ionization potential increases the probability of ion emission. It can be stated that, since $x_o$ is on the order of $10^{-6}$ cm, fields of $10^6$ V/cm would be required to produce significant enhancement of ion emission. Such fields are achievable if one considers the microstructure of certain surfaces. The electric fields at the peaked structures of surface irregularities could conceivably reach values of $10^6$ V/cm using only moderate applied voltages--even when the average surface field calculated from parallel plate geometry is of the order of $10^3$ to $10^4$ V/cm. It may be that the ion emission observed in our laboratory from silicon surfaces is preferentially emitted from these peaks. This would also suggest that, since more impurity ions leave the peaks compared with the depressions, diffusion of impurities near the surface likewise is predominantly near the peaks.

### 2.6.3 EXPERIMENTAL STUDIES

Experimental observations suggest the feasibility of removing certain impurities from materials by heating the material in the presence of a strong electric field. Accordingly, we carried out the experiment of heating a small slab of silicon using the type of substrate heater discussed in subsection 2.4.3. At a temperature of 750°C, the current voltage curve shown in Figure 39 was obtained. The silicon used was cut from a piece of high purity single crystal material.

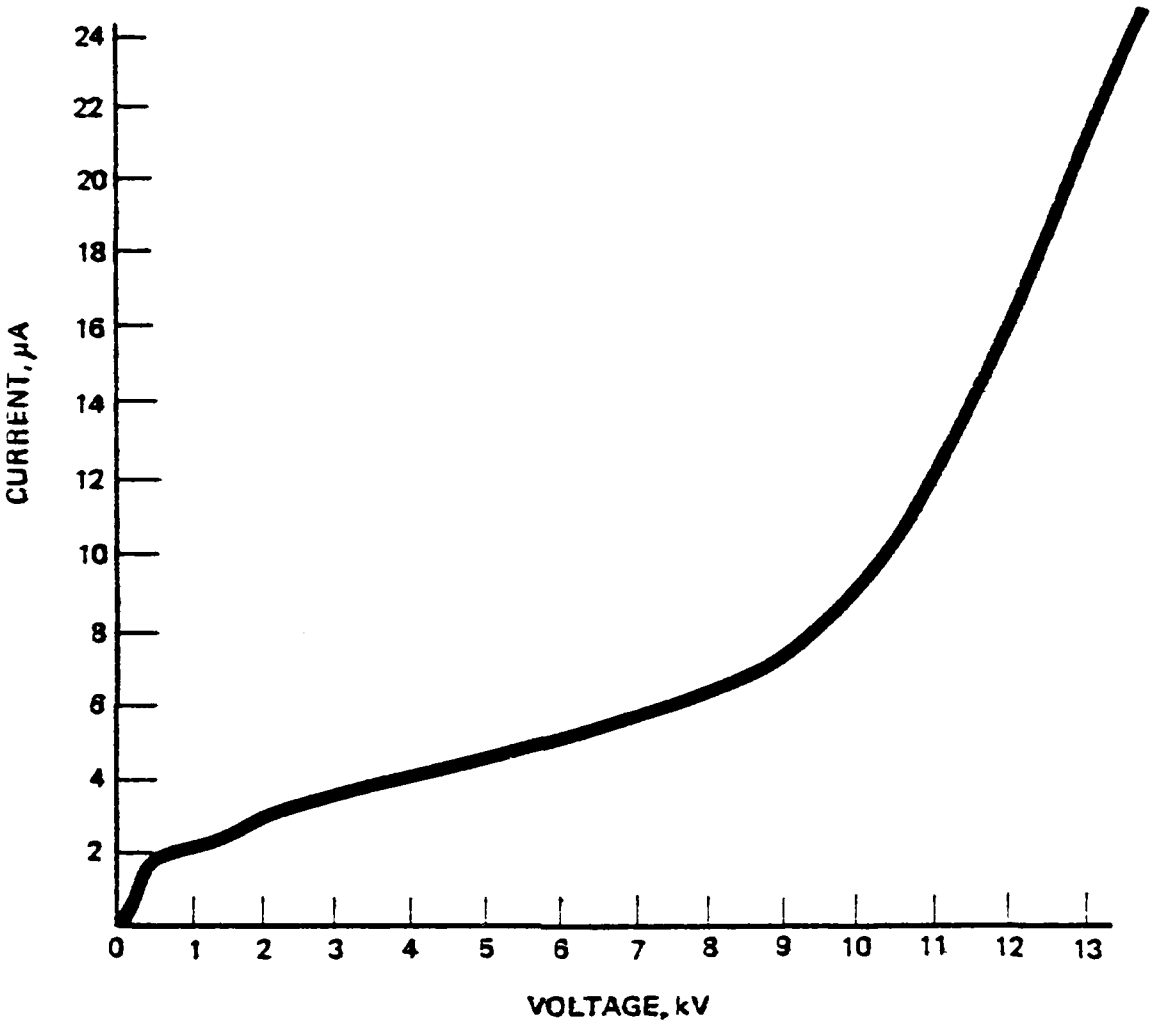


Figure 39. Current-Voltage Characteristics of Ions Leaving Silicon Surface and Electrons Arriving at Silicon Surface at 750°C

The current measured was a sum of the emitted ion current plus the secondary electron loss at the collector. No attempt was made to determine the ionic species, but the emission of ions from the silicon was demonstrated. We observed an ion current of about 1.5 μA at low fields, rising rapidly with fields as shown in Figure 39. About one-half of the rise may be due to secondary electrons from the collector bombarded by the ions. The current remained stable at 10 kV for about one hour with no clear indication that currents were diminishing in this test. The steadiness of the current during this interval implies not only removal of impurity ions, but also the ready diffusion of ions from deep in the material to the surface as well.

Let us note that these currents are substantial in terms of the rate of removal of impurity ions. The silicon atom density in silicon is about $5 \times 10^{22}$ atoms/cm$^3$. If the impurities in the material we had in our test constituted about $10^{-6}$ atom-fraction, we would have $5 \times 10^{16}$ impurity atoms/cm$^3$. A current of 10 μA would correspond, in this setup, to $3.2 \times 10^{-6}$ A/cm$^2$, or $2 \times 10^{13}$ singly charged ions/cm$^2$-second. The current densities observed in the experimental test setup are probably composed of ions representing most, if not all, of the impurity atoms present in the heated sample. The fact that undiminished currents were observed in these tests is thought to be due to the large volume of the silicon sample. As tests are repeated with thin substrates, in the range of 30 to 200 microns, current densities are expected to fall off more rapidly with increasing times. In general, the observed currents are indicative of fast impurity depletion times.

With an impure material, such as metallurgical grade silicon, the impurity level can be expected to be about 1 atom in 100, which is $10^4$ times larger than the 1 part in $10^6$ indicated above. The extracted current would increase accordingly. However, it does not appear that it will become necessary to be concerned about space charge effects.

Altogether, the process appears to be an extremely hopeful one for removing certain impurities from thin sheets of silicon and other materials. High purity foils could be produced by this process. Aluminum that reaches the surface of the silicon sheet is expected to be readily removed by this process because of its low ionization potential (5.96 eV), and because of the observed emission of aluminum ions from other substances. Iron, with its much lower vapor pressure and its higher ionization potential, may not ionize as efficiently but, on the other hand, it diffuses very rapidly in silicon.

Tests were also made on nickel foil having a thickness of $3.2 \times 10^{-3}$ cm (1.25 mil). The foil was heated using the substrate holders and heaters described in subsection 2.4.3. Temperatures up to 820°C were achieved, and voltages up to 10 kV were applied to the heated surfaces using special collector electrodes as the grounded electrode and ion collector. The collector was designed to minimize the back sputtering of atoms discharged from the collector surface during ion bombardment. The current voltage characteristics were found to be similar to that shown in Figure 39. The current increases with decreasing distance between the sample and the collector. It is clear from the data that the current in the range of several hundred microamperes is dependent upon the applied electric field, and the electric field can be varied by changing the voltage or the distance between sample and collector. With the application of 10 kV and a spacing of approximately 1 cm, the parallel plate electric field is $10^4$ V/cm. This is enhanced somewhat because of the use of a segmented collector. Nevertheless, this value is below that predicted in the previous section, which is required to produce significant enhancement of ion emission. But we do see that the experimental ion production of over 400 μA is significant in reducing impurities.

The nickel sample used in one test had a surface area of nearly 25 $cm^2$ with the total number of nickel atoms of $7 \times 10^{21}$ atoms. For a run of 1.5 hours, 0.5 coulombs of charge were extracted from the sample.

Assuming each charge represents an ion extracted, this is equivalent to $3 \times 10^{18}$ ions of impurity removed. A surface analysis of two nickel foil samples was performed by an outside laboratory (Truesdail Laboratories, Inc.) using atomic absorption spectrometry. One sample was treated by the high field impurity depletion technique. The other sample was untreated and removed from the nickel foil immediately adjacent to the treated sample. The results of the analysis are summarized below:

| Element | Treated | Untreated |
|---|---|---|
| Hydrogen | Nearly identical | |
| Boron | Lower | Higher |
| Carbon | None | Trace |
| Oxygen | Higher | Lower |
| Hydroxide | Slightly higher | |
| Sodium | Lower | Very slighltly higher |
| Magnesium | Lower | Very slightly higher |
| Aluminum | Lower | Very slightly higher |
| Silicon | Higher | |
| Potassium | Lower | Higher |
| Calcium | Lower | Higher |
| Titanium | Identical | |
| Chromium | Lower | Higher |
| Manganese | Lower | Very much higher |
| Nickel | Identical | |

The elements depleted from the treated sample were boron, sodium, magnesium, aluminum, potassium, calcium, chromium, and manganese. Results of some of the other impurities were less certain, but indications are that higher temperatures, higher fields, and longer runs are required to give more meaningful results. Apparatuses are being prepared to heat metallurgical grade silicon close to the liquidus point using induction heating to measure the decrease of Aℓ, Fe, and B impurities.

SECTION 3

# EXPERIMENTAL RESULTS: POWDERS AND COATINGS

This section includes the experimental results of interest in metallurgy. EHD is applied toward the production of new material forms in powders and coatings. Its aim is primarily to show the capabilities of this new technique and to suggest to experimenters in material sciences directions that might be pursued. Several accomplishments were reported previously such as single crystal spheres, adherent uniform coatings, etc. (Ref. 3). In this report spherical bicrystals, amorphous powders, and semiconductor coatings and films are described and, in addition, the initiation of a solid solubility study. (Ref. 19).

## 3.1 ALUMINUM ALLOY POWDERS

A wide variety of experiments were performed using pure aluminum and the following aluminum alloys: Aℓ-4.5%Cu, Aℓ, Aℓ-3%Si, Aℓ-6%Si. Results from Aℓ-4.5%Cu were reported previously (Ref.2&3). The pure aluminum and the aluminum-silicon alloys were tested to determine the effects of rapid solidification upon crystalline structure.

The solid solubility limit of silicon in aluminum is approximately 3%. In order to observe possible difference in the subsequent structure due to differences in solubility under such a process as rapid solidification, aluminum alloys with various percentages of silicon ranging from zero to 6% were tested. The investigation consisted of processing each alloy in the Tabletop Powder Generator. Analysis involving SEM and TEM was performed at the University of Illinois (Ref.11 ). The aim was directed at determining the following:

a. The effect of solute content on interface breakdown and solidification morphology in fine spherical powders.

b. The effect of solute content on undercooling and nucleation kinetics, if any.

c. To determine whether increases in solute solubility limit could be obtained in rapidly solidified powders produced by EHD.

It is anticipated that the latter would be observed in the alloy containing 6%Si, which is well above its solid solubility in Aℓ.

Preliminary results from the analysis indicate that increasing solid solubility of Si occurs with decreasing particle size and therefore increasing cooling rates.

Aluminum alloy powders produced in the size range from below 0.1 to about 1 μm were found to be composed largely of single crystals as reported previously (Ref. 3). In addition, particle structures consisting of bicrystals also were found. In some instances, the crystal boundary divides the particle evenly along its diameter. In other particles, the crystal boundaries are less symmetrical. Figure 40 shows a TEM of a submicron bicrystal powder of Aℓ-3%Si and the double electron diffraction pattern indicating two crystals. Figure 41 shows another similar bicrystal and accompanying electron diffraction pattern. In a way, it is not surprising that, at rapid cooling rates, > $10^5$ K/s, nucleation might be initiated in two places almost simultaneously. It would seem that two nucleation sites may occur at the droplet surface, but they do not have to be at opposite sides to result in the crystalline configuration shown in the above two figures.

## 3.2 IRON ALLOY POWDERS

Two iron alloys were tested in the Feasibility Model. One test was recently made using $Fe_{75}Si_{15}B_{10}$ obtained from General Electric Research Laboratory. Powders were collected in bulk and on tape and have been

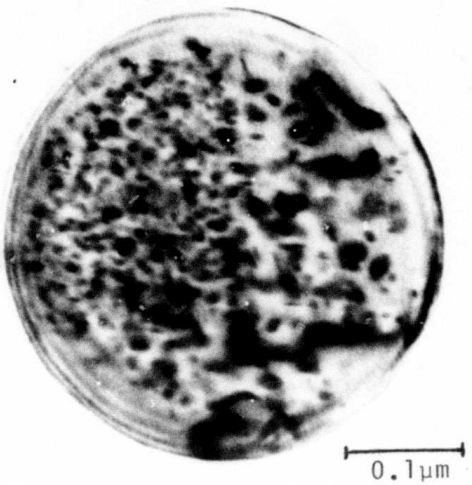


(a)

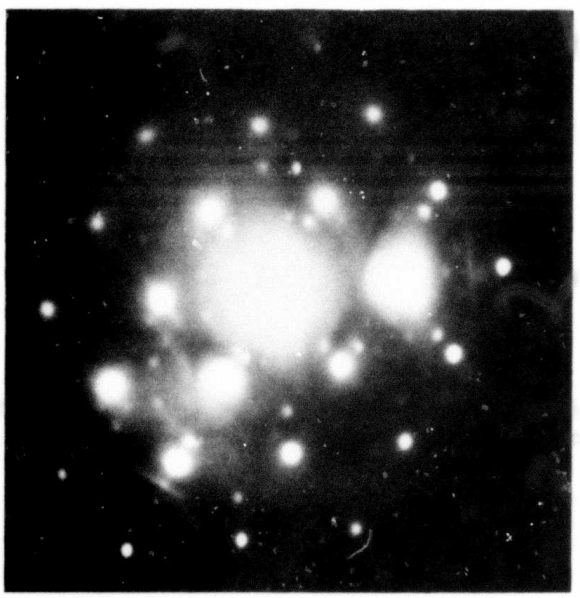

(b)

Figure 40. Transmission Electron Micrograph and Electron Diffraction Pattern of Small Diameter Al - at% Si Alloy Powder Produced in the EHD Apparatur. Magnification 250,000X. Both the selected area diffraction pattern and dark field images indicated that the primary phase was in one orientation. There is also evidence that a second phase precipitated during or subsequent to solidification.

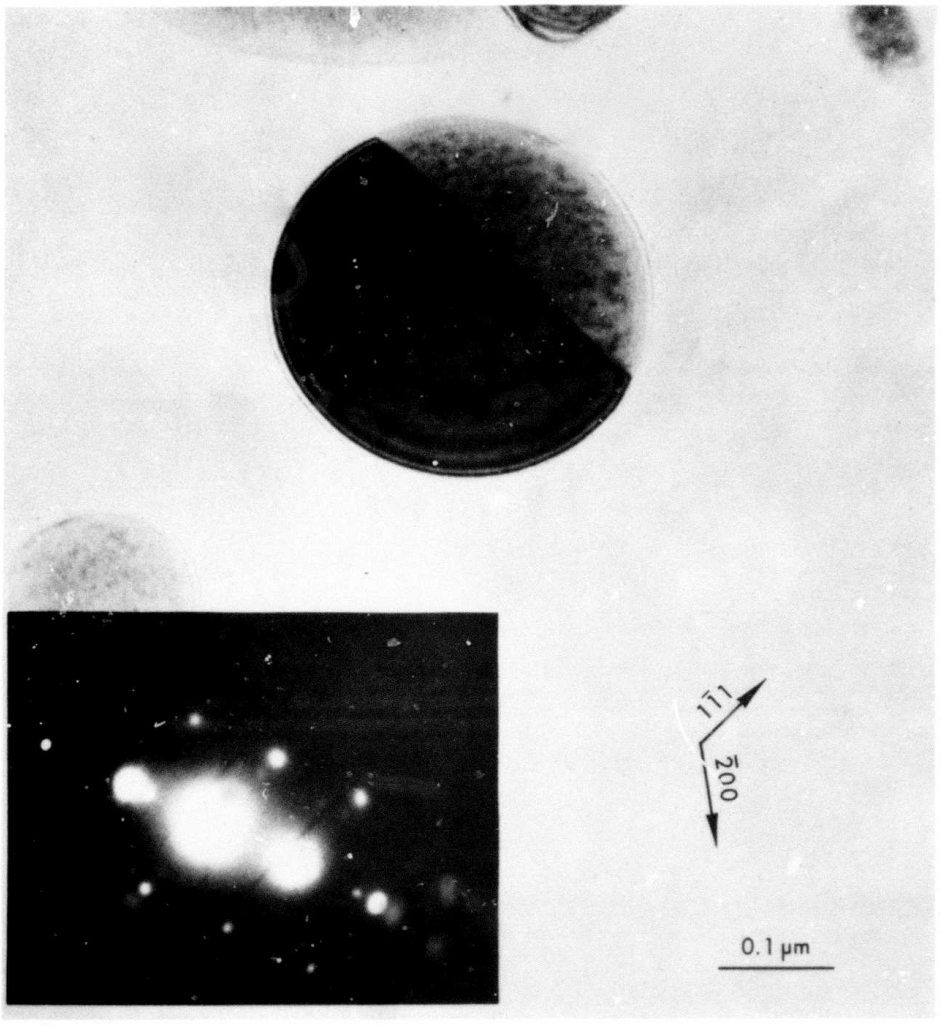


Figure 41. TEM of 0.35 Micron Al 3%Si Bicrystal Alloy Pwoder with Accompanying Double Diffraction Pattern

sent for analysis. No results of the test have yet been obtained but will be presented in the next quarterly report.

Alloy composition and cooling rate prior to solidification are the most important variables affecting formation of noncrystalline structures. The alloy, $Fe_{40}Ni_{40}P_{14}B_6$ with a melting temperature of close to 1000°C, was tested which is known to make amorphous powders at the low cooling rates of $10^4$ k/s. Powders were collected on replicating tape and prepared using the method described in subsection 2.4.3 for TEM analysis. Coarse powders were also collected and filtered with a sieve to eliminate those particles greater than 400 mesh. The rest were analyzed by X-ray diffraction.

Microstructural Analysis of $Fe_{40}Ni_{40}P_{14}B_6$

The deposits of the high temperature alloy droplets, splats, and continuous "matrix" film were collected on aluminum, copper, and vinyl cellulose collectors. Scanning and transmission electron microscope techniques were used to study the microstructure of the deposits to determine whether they were noncrystalline.

Figures 42(a) and (b) show secondary electron images of the fine to intermediate size ($\sim 10^{-2}$ μm to $\sim$ 5 μm) powders collected on vinyl cellulose and aluminum substrates, respectively. From the geometry of these particles, it is evident that they solidified in flight before striking the targets. The finer particles in these figures are difficult to discern even at this magnification and were studied via transmission electron microscope techniques as noted below.

Figure 43 shows secondary electron images of the intermediate to coarse powders and splats ($\sim$ 5 μm to $\sim$ 50 μm) collected on an aluminum substrate. Splats as large as 50 μm are noted in these micrographs. It appears that

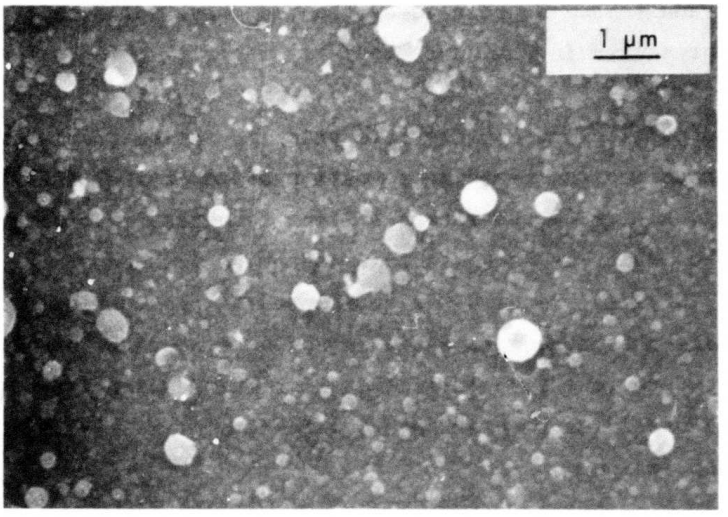


(a)

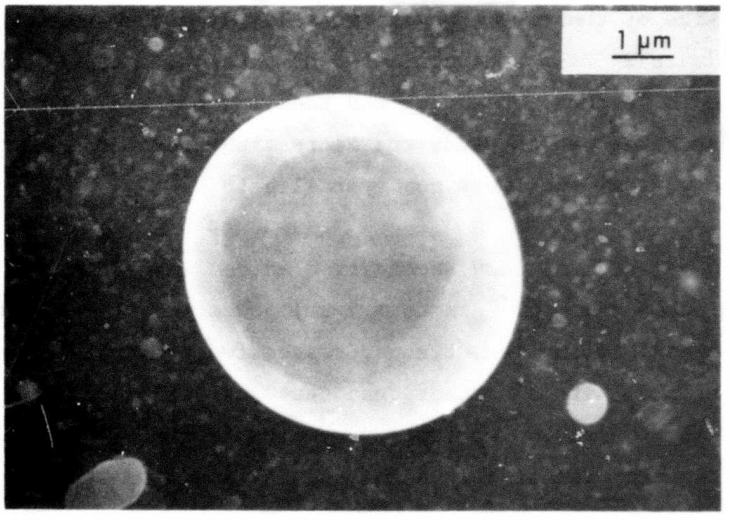


(b)

Figure 42. Secondary Electron Images of the Fine Atomized Powders of Fe-Ni-B-P Metallic Glass Alloy Produced by the EHD Technique at 10,000X. The collectors in (a) and (b) were vinyl cellulose and aluminum, respectively.

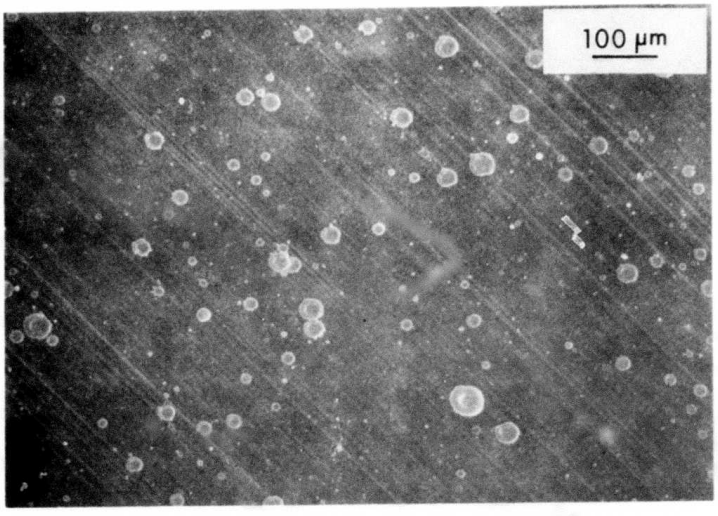


(a)

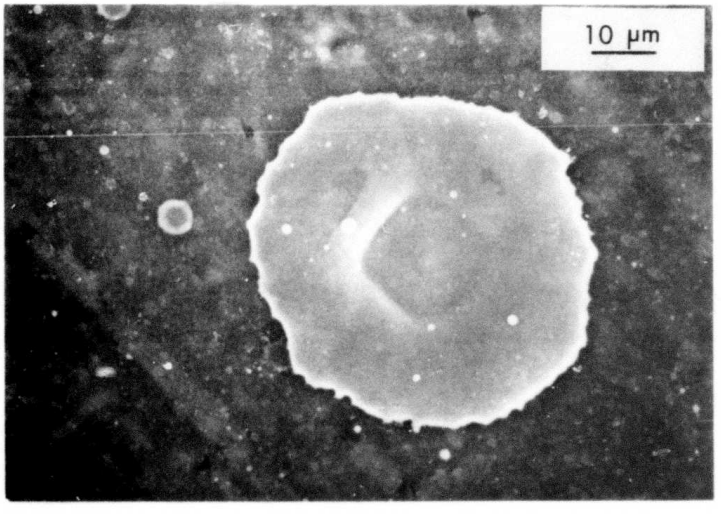


(b)

Figure 43. Secondary Electron Images of the Coarse Atomized and Splatted Droplets of Fe-Ni-B-P Metallic Glass Alloy Produced by the EHD Technique. (a) is at 100X; (b) is at 1000X.

most of the coarse droplets arrived at the target in the liquid state and splatted on impact. Note the flattened particle (splat) shown in Figure 43(b).

Transmission electron microscope specimens were prepared by cutting 3 mm discs from the vinyl cellulose films, dissolving the plastic substrate in acetone, and mounting the resulting sample on a copper grid. Since there is a relatively continuous deposit of metallic glass on the substrate and it had embedded the powders and splats, there was no need to coat the samples with carbon as in the analysis carried out on the aluminum alloy specimens.

Figure 44 shows a TEM image of a portion of a specimen deposited on the vinyl cellulose substrate. The specimen is composed of very fine powders in the size range of less than $10^{-2}$ μm to ∿ 0.3 μm. In addition, it was found that these particles rest on or are entrapped in a continuous "matrix" film of the alloy which was deposited almost uniformly on the substrate. The film thickness was measured to be of the order of ∿ $10^{-2}$ μm. It is postulated that this film was produced by continuous deposition of extremely fine droplets and ions of the elements in the alloy.

Figure 45 shows an electron diffraction pattern of an area of the continuous "matrix" film ∿ 0.3 μm in diameter. The diffuse rings indicate that the structure is amorphous. Similar patterns were obtained from other areas of the specimens.

Higher magnification images of some of the coarser powders in Figure 44 are shown in Figures 46 and 47. A selected area electron diffraction pattern of the region denoted A in Figure 46 is shown in Figure 48. Again, the diffuse rings are indicative of the absence of crystallinity in the powder particle and the "matrix" film contained in this area. Figure 47 shows a higher magnification image of the selected area in Figure 46, which indicates that the powder particle examined was indeed

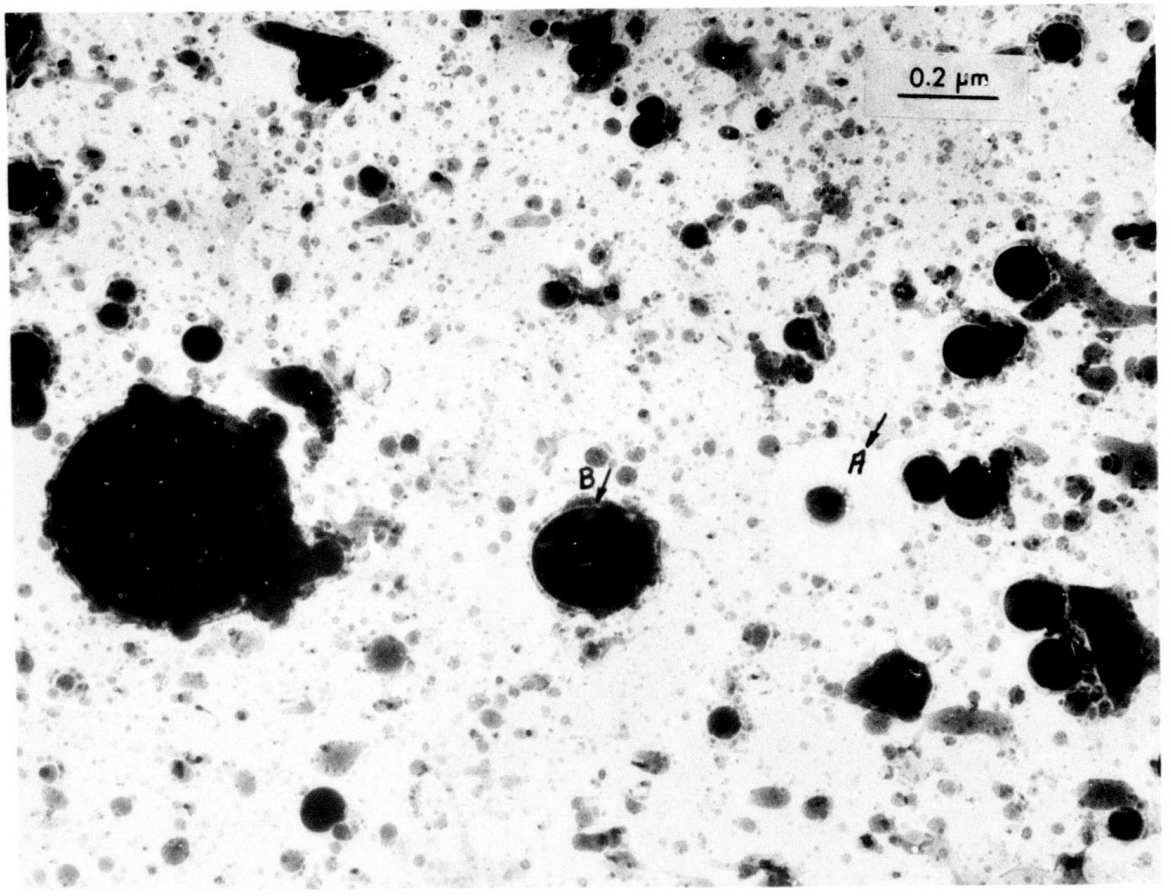


Figure 46. Transmission Electron Microscope Image of a Deposit, Fine Powders, and "Matrix" Film, of Fe-Ni-B-P Metallic Glass Alloy Produced by the EHD Technique and Collected on a Vinyl Cellulose Substrate at 74,000X.

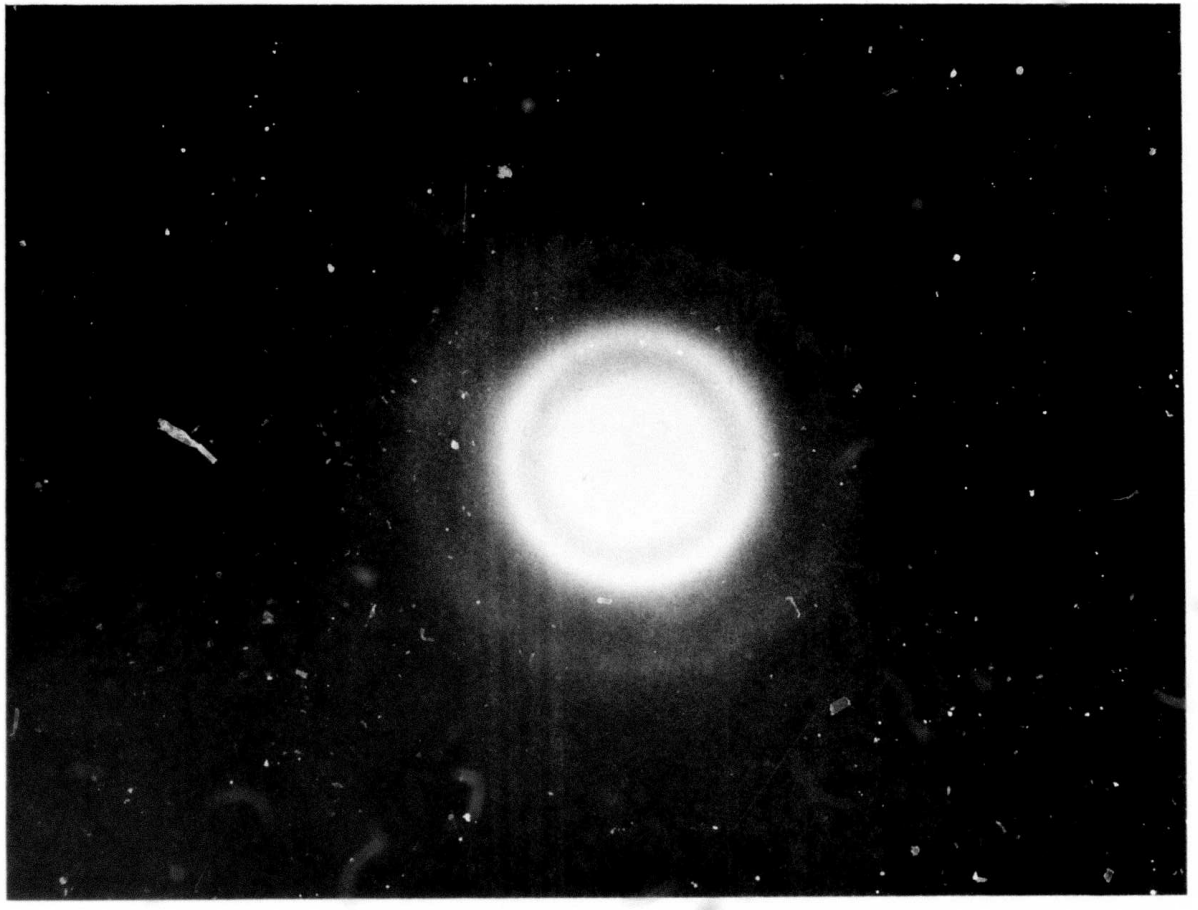

Figure 45. Selected Area Electron Diffraction Pattern, 0.3 μm in Diameter, of the Continuous "Matrix" Film Deposit of Fe-Ni-B-P Metallic Glass Alloy Produced by the EHD Technique on a Vinyl Cellulose Substrate

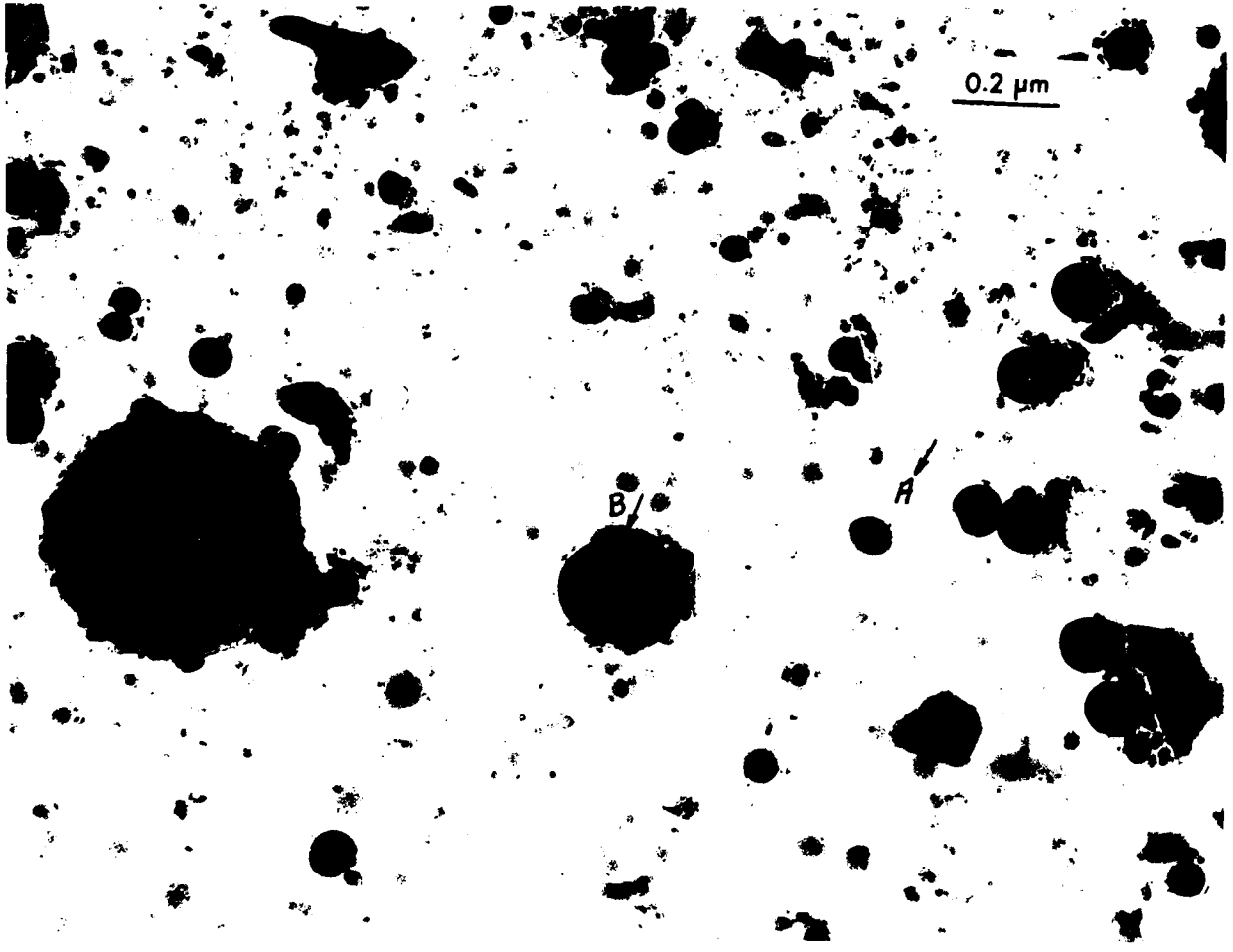


Figure 46. Transmission Electron Microscope Image of a Deposit, Fine Powders, and "Matrix" Film, of Fe-Ni-B-P Metallic Glass Alloy Produced by the EHD Technique and Collected on a Vinyl Cellulose Substrate at 74,000X.

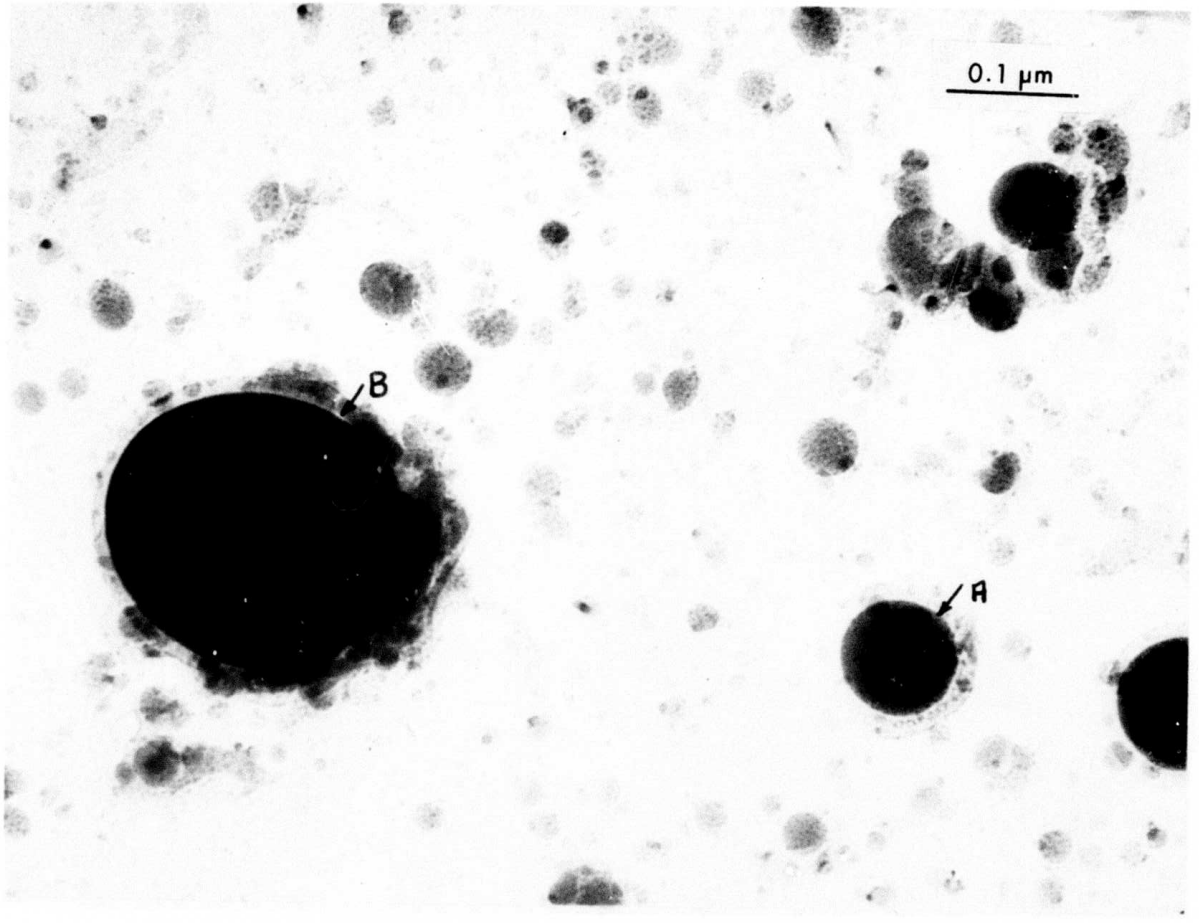


Figure 47. Transmission Electron Microscope Image of a Deposit, Fine Powders, and "Matrix" Film, of Fe-Ni-B-P Metallic Glass Alloy Produced by the EHD Technique and Collected on a Vinyl Cellulose Substrate at 200,000X

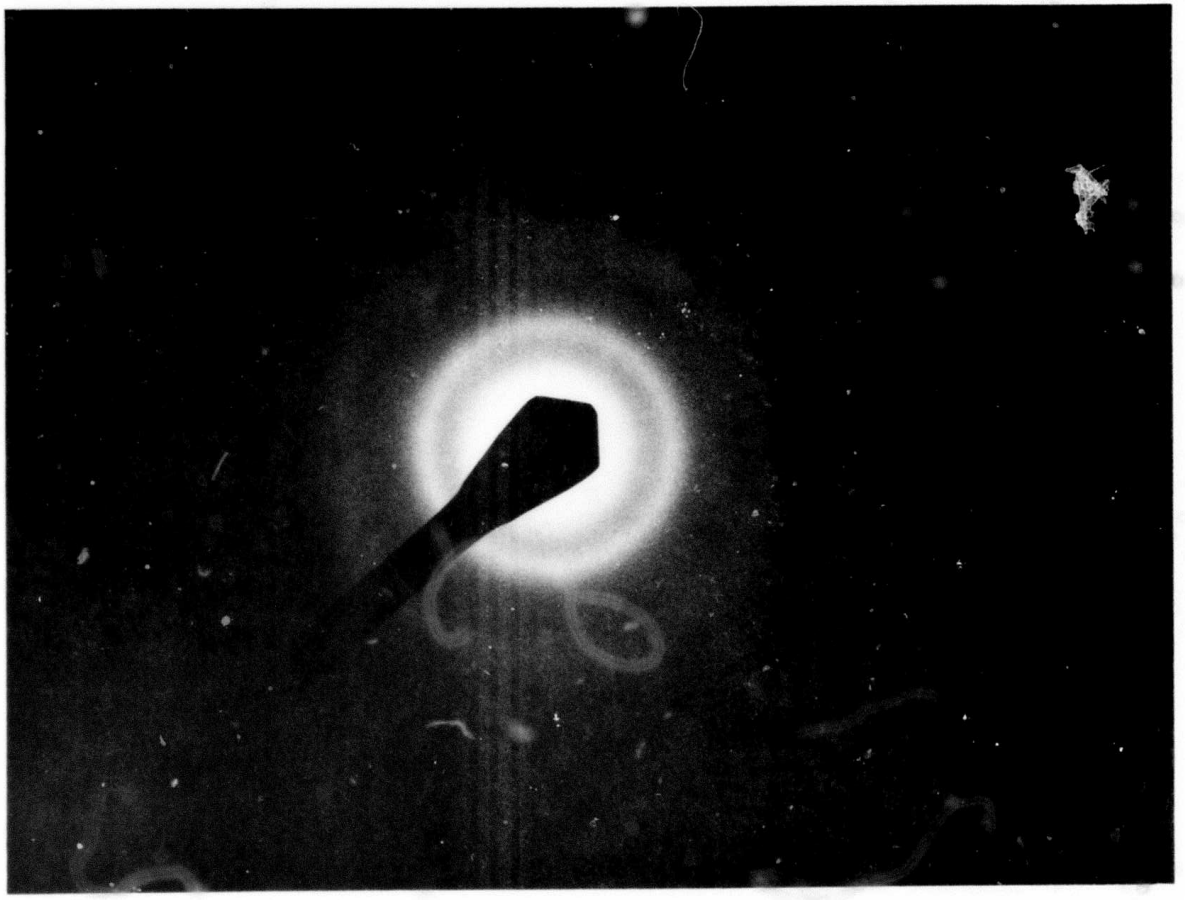

Figure 48. Selected Area Electron Diffraction Pattern, Area Denoted as A in Figures 46 and 47 of a Powder Particle and the "Matrix" Film Deposit of Fe-Ni-B-P Metallic Glass Alloy Produced by the EHD Technique

electron transparent and noncrystalline as evidenced in Figure 48. On the other hand, the larger powder particle in Figure 47, denoted B, is too coarse to be electron transparent, and therefore no direct evidence of its noncrystallinity could be obtained via electron diffraction.

Figures 49 and 50 show other examples of fine powders and "matrix" film collected on a viny cellulose target. The two figures are identical except for their exposure during printing. This was done to show that all the particles in the size ranges shown in Figure 49 are electron transparent. Note the presence of finer particles on and under the large particles of Figure 50. Electron diffraction studies showed all these electron transparent particles to be noncrystalline.

Powder samples collected in the vacuum chamber after the run were sorted to analyze those particles with diameters below 40 μm. A Norelco Diffractometer was used to produce the diffraction pattern of this sample which is shown in Figure 51. The Diffractometer radiation was from a Mo anode X-ray tube and monochromated by a LiF crystal on the diffracted beam so that only Kα with a wave length of 0.1710Å reached the powder specimen. The vertical scale is the intensity in counts per second, and full scale on the graph corresponds to 500 counts per second. The horizontal scale is the 2θ Bragg angle.

The diffraction pattern consists of a variable background indicated by the smooth line, to which are superimposed a series of maxima which indicate the presence of crystals. The smoothly variable background with a broad maximum located slightly below 20° in the 2θ angle shows that there is some amorphous phase in the powder - perhaps 50%. The various peaks corresponding to the crystalline phase or phases are relatively broad, and this indicates that these crystals are very small, probably less than 1 micron. This broadening of crystalline peaks is the so-called Debye broadening. A transmission electron diffraction pattern should consist of an amorphous matrix (without any contrast) in

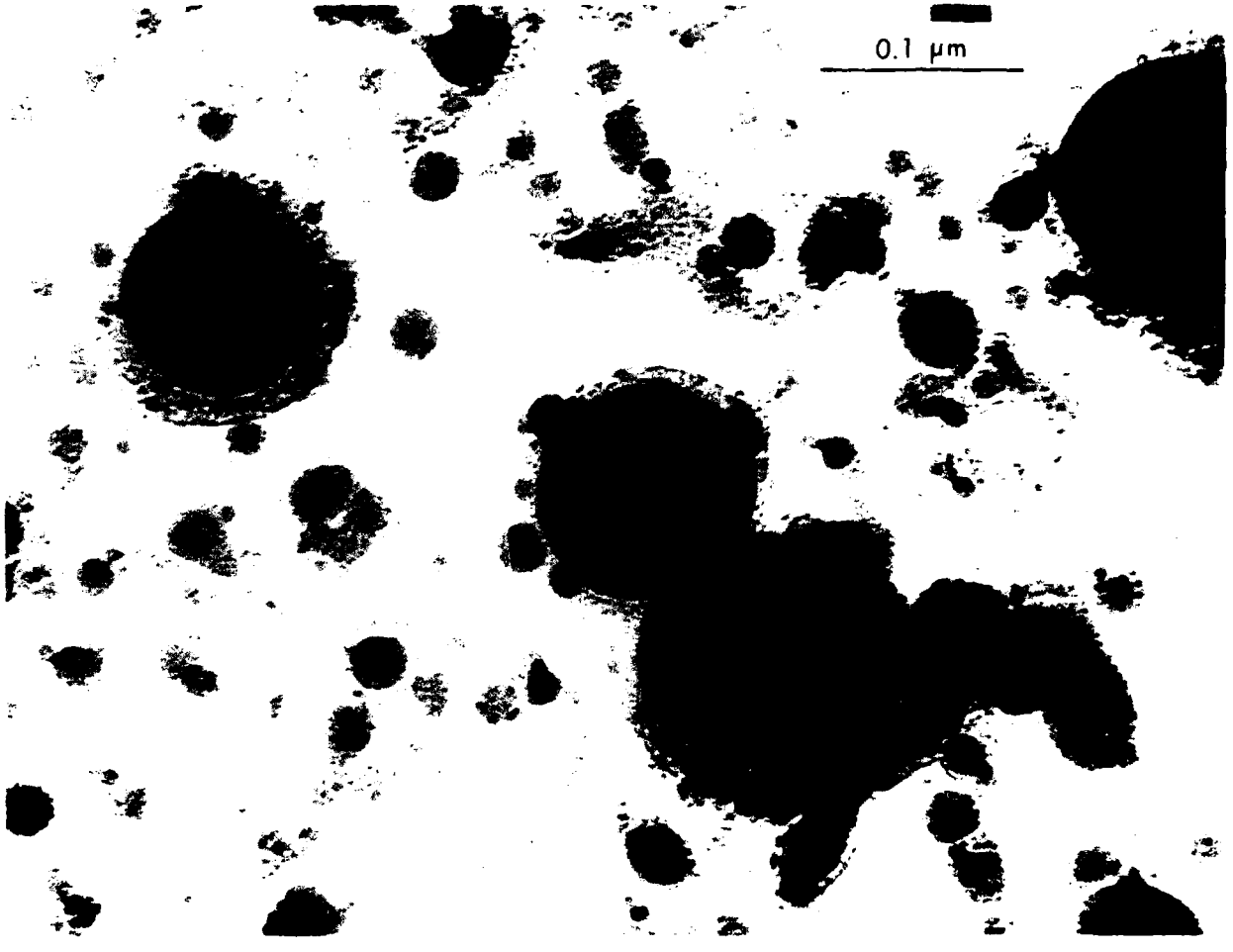


Figure 49. Transmission Electron Microscope Image of a Deposit, Fine Powders, and "Matrix" Film of Fe-Ni-B-P Metallic Glass Alloy Produced by the EHD Technique and Collected on a Vinyl Cellulose Substrate at 300,000X

Figure 50. Transmission Electron Microscope Image of a Deposit, Fine Powders, and "Matrix" Film of Fe-Ni-B-P Metallic Glass Alloy Produced by the EHD Technique and Collected on a Vinyl Cellulose Substrate at 300,000X.

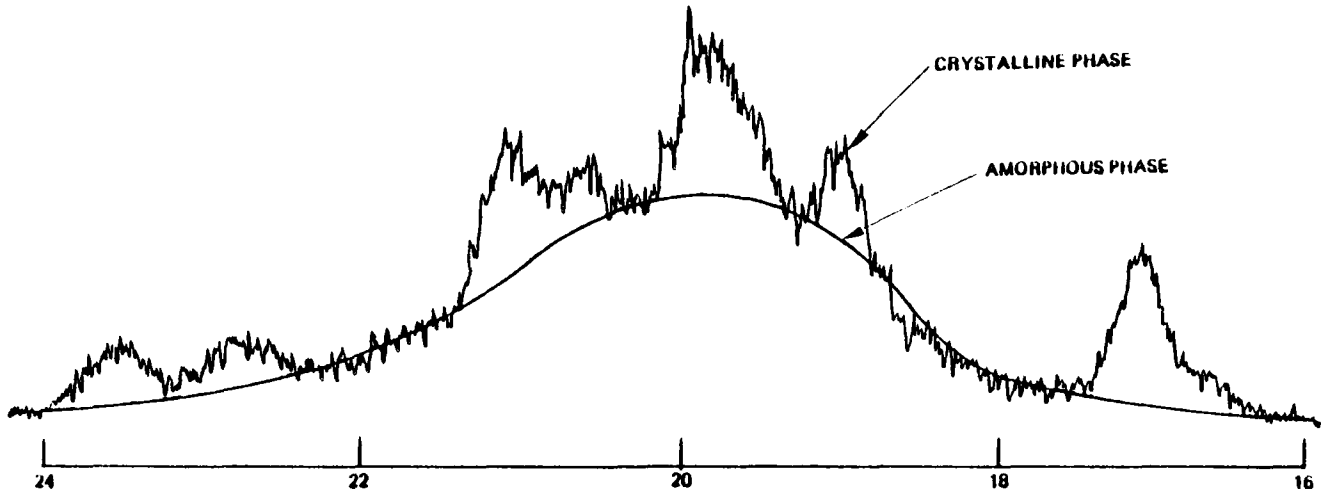


Figure 51. X-ray Diffraction of Fe-Ni-B-P Alloy Showing Crystalline Peaks and Amorphous Envelope

which are embedded very small crystals. From the X-ray diffraction pattern, it is not possible to identify the crystalline phase or phases because too few diffraction peaks are observed, and also because of the complexity of the alloy used in these experiments.

It is also not clear whether the crystalline phase is associated with the amorphous phase in a given particle, or if some of the particles are completely amorphous and the others are crystalline. It should be recalled that no evidence of crystalline phases was found in the electron-transparent submicron powders. It is then concluded that the presence of the crystalline phase in the larger particles can be ascribed to the decrease in cooling rate with increasing particle size.

The calculated cooling rate of the particle, whose diameter is just below 0.1 micron, is about $2 \times 10^6$ K/s for radiative cooling. This is sufficient, by over two orders of magnitude, to assure the production of amorphous powder. The calculated solidification time for this powder is comparable to its time of flight of about $10^{-4}$ seconds. Powders with diameters of 0.01 micron, also seen in Figure 49, have calculated cooling rates exceeding $10^7$ K/s. Powder B in the same figure, whose diameter is greater than 0.2 micron, is too coarse to be electron transparent and, therefore, no direct evidence of its noncrystallinity could be obtained via electron diffraction. However, calculations indicate that powders whose diameters are below 20 microns should have cooling rates greater than $10^4$ K/s and are expected to be amorphous. This is consistent with the results of mixed microcrystalline and amorphous material obtained from the X-ray diffraction tests. If the time of flight is too short to assure solidification in flight, then splat cooling will even increase the cooling rate above the calculated value, assuming radiative cooling only.

## 3.3 COATINGS

Coatings and thin films are made with the substrate close to the droplet source and the source operated to generate droplets sufficiently large so as not to solidify in the time-of-flight. A substrate holder is used with a heater that is able to maintain the substrate at temperatures up to 1300K. Castings have also been made by collecting splat cooled droplets in a mold to obtain a part that is large, fits the mold, and yet is composed of rapidly solidified alloys.

### 3.3.1 ALUMINUM COATINGS

#### Aℓ on Titanium

A motivation for investigating the coating of aluminum on titanium is derived from aircraft construction and from many other engineering applications. Aircraft parts should be as light and as strong as possible. At low temperature, aluminum is used; at higher temperatures titanium is used, which is somewhat more dense. But Ti is subject to oxygen embrittlement at higher temperatures (> 300°C), so that stainless steel is used. Aℓ and SS are not subject to embrittlement, because they form a coating ($\sim$ 50Å of $A\ell_2O_3$ for aluminum) that protects them. $TiO_2$ on titanium surfaces diffuses into the body at high temperature.

Titanium and Ti alloys have a relatively low density of 4.5, which is between Aℓ (2.7) and steel (7.8) and is one of its most important advantages. On a strength-to-weight ratio and at room temperature, Ti alloys compare favorably with both aluminum alloys and steels. Aℓ alloys are age hardened in the 100-200°C range and cannot be used at higher temperatures without losing their strength. A serious drawback for the use of Ti alloys at high temperature is their reactivity with oxygen. Oxygen atoms diffuse readily into the Ti lattice and occupy the interstitial sites. As much as 33 atomic percent oxygen can dissolve into

Ti before the compound $Ti_3O_2$ starts to form. The presence of oxygen in the Ti lattice renders the metal extremely brittle and must be avoided at all cost. One obvious way to prevent oxygen diffusion in Ti at high temperature is to cover it with a protective layer impermeable to oxygen. A large effort has been devoted at other laboratories to finding a ceramic coating to protect Ti in an oxidizing high temperature environment, and no satisfactory solution was found. It is practically impossible to provide a satisfactory bond between an oxide ceramic coating and a metal, except if an oxide layer is formed first on the metal. Such an oxide layer will eventually form on Ti but not before an unacceptable quantity of oxygen has penetrated the titanium part and rendered it extremely brittle. Metallic coatings on Ti have also been tried without success. First, it is very difficult, if not impossible, to deposit a coating by electrolysis. The difficulty seems to be in the lack of a good bonding between Ti and, for example, a Ni coating.

A promising high temperature oxidation resistant coating might be an intermetallic compound in the tatanium aluminde family. To produce this coating, Aℓ would first be deposted on Ti and this would be followed by a diffusion heat treatment to react Aℓ with Ti. This idea is not new, but no satisfactory technique exists to deposit Aℓ with good atomic bonding. The first step in the process would be to build up an adherent coating of Aℓ having a thickness of at least 1 or 2 μm. The Ti part could be heated for a sufficient time at a temperature to be determined in the range of 400 to perhaps 1000°C in high vacuum or in pure inert gas. The oxidation resistance of the coating can be tested on a coated side and uncoated side of Ti to provide a direct measurement of the quality of the coating.

A coating of aluminum was sprayed, using EHD in our laboratory, on one side of a sample of commercial titanium. The substrate was maintained at a temperature of 700°C during the deposition process to insure that

the impinging particles would remain molten during the formation of a continuous film. Figure 52 shows a cross section of the resulting coating on the Ti substrate. By X-ray analysis, the coating was found to be composed of $TiAl_3$. Exposure of the sample to air at a temperature of 650°C for 48 hours resulted in large grain growth in the crystalline structure at the unprotected side shown in Figure 53(b), but not on the coated side, Figure 53(a). This indicates that the protected (coated) side of the substrate did not allow penetration of any oxygen from the heat treatment in air. The visible demarcation (Figure 52) between the "as deposited" coating and substrate disappeared after the heat treatment seen in Figure 53(a). Furthermore, the apparent cracks in the original coating, postulated to be a result of the brittleness of $TiAl_3$, were alleviated by further reaction between the substrate and coating.

Al on SS

During the process of microparticle deposition on sample collectors, beam shutters and chamber surfaces in the experimental area are also coated. Depending upon the droplet size and exposure time, coatings ranging from well below a micron to millimeters in thickness have been formed. Splat cooled thin aluminum coatings show good adherence to SS and copper surfaces. Thick coatings have a tendency to peel off the substrates. The SS surface shown in Figure 54(a) is coated with layers of Al 4.5%Cu with good adherence in the thinly coated areas (< 0.1 cm). The thick coating in the center separated from the substrate and shows the qualities of a coating in Figure 54(b). Surface scratches on the substrate are reproduced in the coating which is 4 mm thick at the thickest part. Some granular quality is seen where the particles were large. This could be developed into a method for making relatively large castings composed of splat cooled material.

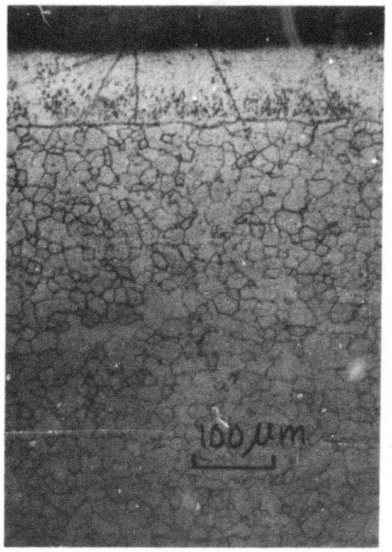


Figure 52. Cross Section of Ti Sample Coated with Aℓ. Coating composed of $TiAℓ_3$

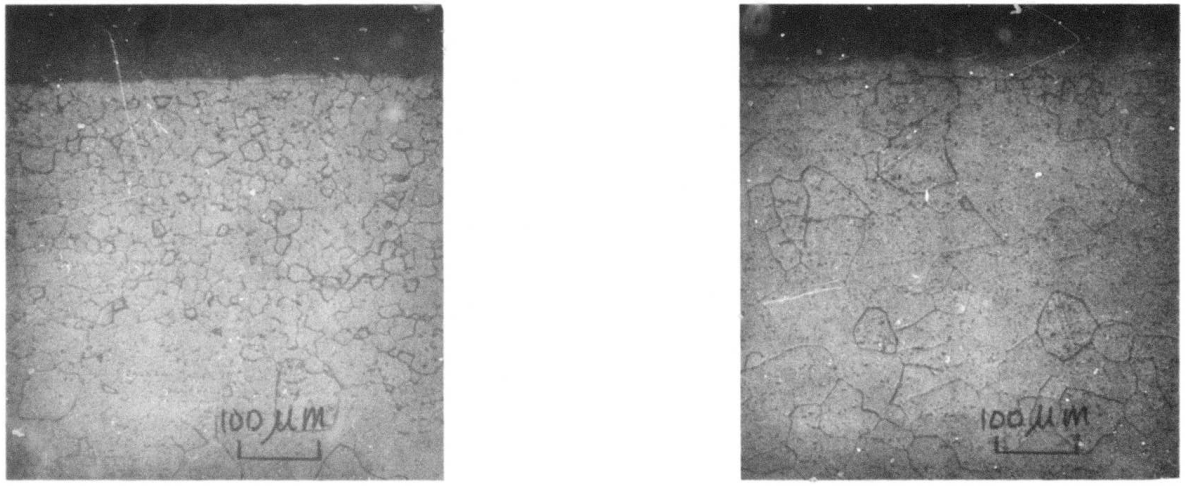


(a) (b)

Figure 53. Al Coated Ti Sample after Heat and Exposure Treatment. (a) Coated Side; (b) Uncoated Side

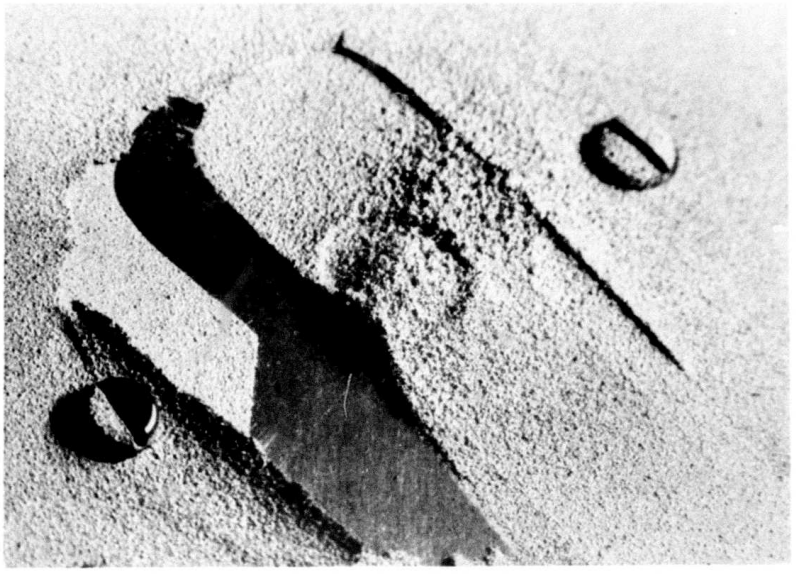

Figure 54(a) Shows an Aℓ 4.5%Cu Coating on SS

Figure 54(b). Shows the "Casting" Obtained from Coating of Figure 54(a)

Aℓ on Plastic

Several types of plastic materials were coated with Aℓ (Aℓ4.5%Cu). The initial droplets imbed into the plastic by a combination of impact and melting. The subsequent droplets solidify on previously deposited particles and form an adherent coating. The surface of the coating is rough with a texture related to the droplet size. This surface could be polished to whatever finish desired. Figure 55 is a photograph of the coated plastic. The sample measured 10 cm on a side and showed a somewhat thicker buildup in the center (bright spot in photo) due to electrostatic focusing of the droplet beam. Figure 56 shows a cross sectional view of an Aℓ coating on a different sample of plastic material. The coating is nearly 0.5 mm at the thickest part and shows good adherence.

### 3.3.2 SEMICONDUCTOR FILMS

Germanium

It has been suggested that germanium would be a good substrate for GaAs because of the excellent epitaxial match. But the high cost of germanium makes it desirable to minimize the amount of material used and clearly precludes it being both the epitaxial and structural substrate. As an experiment, a thin coating of germanium was formed on an alumina substrate.

Germanium did not wet either vitreous carbon or alumina crucibles which were typically heated close to 1000°C to achieve the melt (melt temperature of 960°C). No visible erosion was found on the ceramic cement (Dylon, Grade C-5) used to hold the nozzle to the feed tube, or graphite nozzles. However, BeO nozzles were found to erode, with the nozzle orifice doubling in size from an original $5 \times 10^{-3}$ cm diameter. The spray did not adhere to graphite substrates, but a fine splat droplet

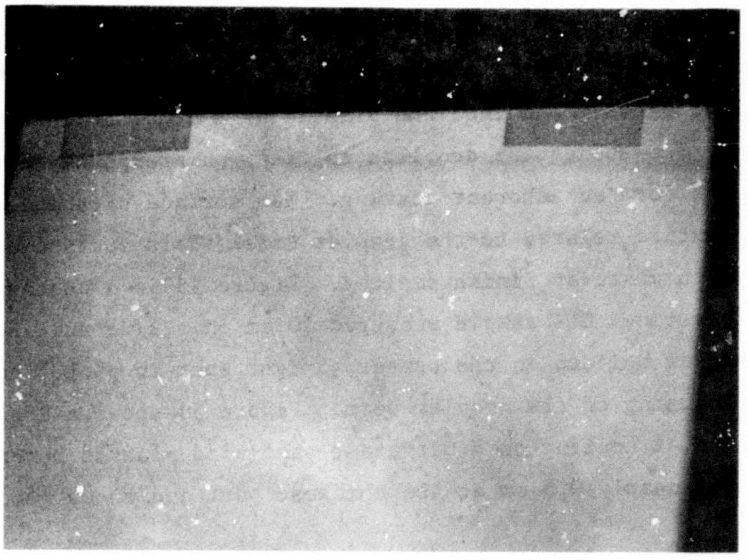

Figure 55. Plastic Coated with Aℓ 4.5%Cu. The sample measures 10 cm on each side.

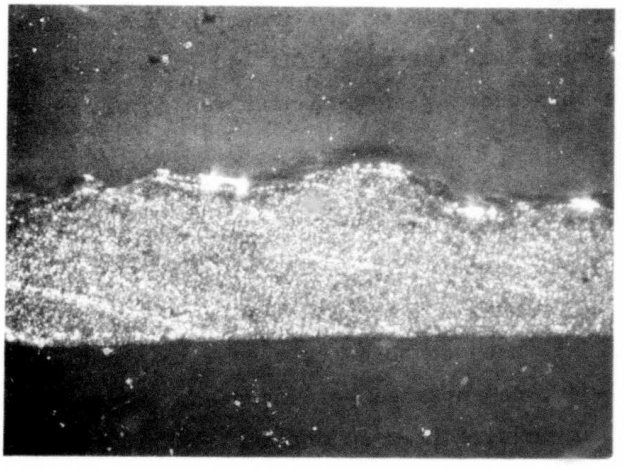


Figure 56. Coating of Aℓ 4.5%Cu on Plastic Cross Sectional View

coating was made on a large alumina sample as shown in Figure 57, where it is compared to an alumina sample that was not coated.

Silicon

Interest in silicon films stems from the need to develop low-cost methods for producing photovoltaic devices. The present day solar cell is close to 400 μm thick to preserve mechanical integrity and is sliced from a single crystal boule. The growth of a large single crystal made from solar grade silicon and sliced are some of the more expensive steps in the processes involved in solar cell production. The slicing causes a material wastage close to 50% of the material used. Since the operational part of the cell is limited to a depth between 50 and 100 μm, the material loss in slicing and the required cell thickness introduce a material loss of an order of magnitude above that needed for cell operation only. This loss could be avoided if a film of silicon is placed on an inexpensive substrate. This was the motivation to deposit a 50 μm film of silicon on various substrates to determine if EHD could be further developed to produce economical solar cells.

A source developed to operate above 1800K to assure melting silicon is described in subsection 2.2. The source nozzle was composed of graphite and had an orifice of 130 μm (5 mil). At the tip of the nozzle, where radiation losses are large, a small tantalum shield is placed on the nozzle to achieve the necessary temperatures to assure that silicon remains liquid at the tip (see Figure 20). It was found that, since silicon wets graphite, capillary action is sufficient to deliver the liquid to the nozzle tip. The mass flow rate is dependent upon the electric field at the tip (controlled by high voltage). In this, the wetting mode, discussed in subsection 2.3, the current rises rapidly over a small range of voltage as seen in Figure 27 of subsection 2.3. Spray is easily turned off by lowering the voltage below the onset and

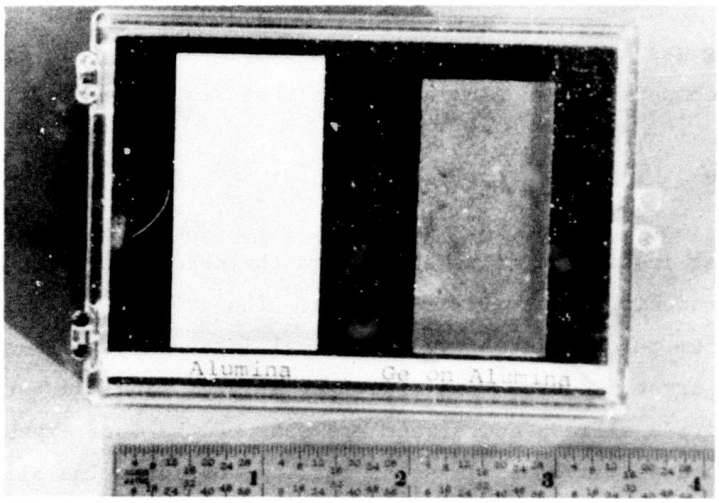


Figure 57. Adherent Coating of Germanium on Alumina Compared with an Uncoated Substrate

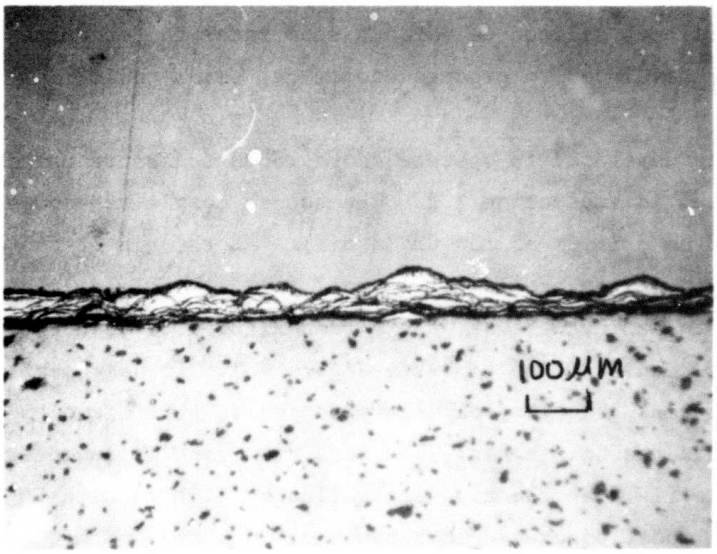


Figure 58. Cross Section of a Coating of Silicon on Mullite

then easily restarted by raising the voltage. There is a small hysteresis, however. Under these conditions, the source can be turned off and cooled down then restarted by heating and applying voltage at a later time. When operated at a temperature of a couple of hundred degrees below the melt temperature, an ion beam is generated, perhaps fed by the silicon vapor. It has been verified that a vapor or gas at the nozzle will generate ion beam current.

Silicon droplet spray has been sustained for about an hour, and both heated and ambient substrates composed of graphite and mullite were coated with silicon films. Figure 58 shows a 50 μm film of silicon adhered to a mullite substrate. The fact that the surface is rough is not a disadvantage in the process toward making a thick film solar cell. The crystalline structure of the film is yet to be analyzed.

## SECTION 4

## APPLICATION OF EHD DROPLET GENERATION: TABLETOP POWDER GENERATOR

The development of a Tabletop Powder Generator is proceeding through a number of stages. First, the development of an Engineering Model will initially be used as an automated data acquisition system. Control functions will then be introduced and tested. Finally, computer control will be implemented over the total system. Once the above techniques are finalized, they will be incorporated into the Production Prototype Model. The Engineering Model, which is being used to further explore the EHD technique for materials processing, is shown in Figure 59. Commercial components are used wherever available, such as the basic vacuum system and console, power supplies, pressure gauges, etc. In addition to the droplet source and collection system discussed in detail earlier, several new features have been developed in our laboratory. These include an isolated digital thermometer to measure the temperature of sources that are maintained at high voltage. The signal from the thermometer is used to control the source heater so that the desired temperature can be selected and maintained. Beam current control is also being automated in conjunction with source feed pressure. The entire system will be controlled by a microcomputer that measures the required parameters, maintains the automatic systems, and collects and stores data. It will be able to perform calculations and display the results in almost any desired form.

The Engineering Model, developed initially as a data acquisition system, will be used to design the Production Prototype Model. This later model will have the capability of producing large quantities of data and will be designed for ease of operation. It will enable the laboratory scientist who is not trained in the art of EHD to perform experiments that produce powders of various alloy combinations, including many not available by other processes.


Figure 59. Engineering Model

The Prototype Model of the Tabletop Powder Generator will be computer controlled and should be installable in a relatively small space in any modern laboratory. This model will be similar in appearance to the Engineering Model but will also incorporate keyboard and CRT readout. The generator should be able to produce more than 20 grams of fine powder in a couple of hours and a much greater quantity of coarse powders.

## 4.1 ENGINEERING MODEL

### 4.1.1 PRESENT SYSTEM

The basic Engineering Model consists of the following subsystems: a vacuum system, microparticle source, current meters, source temperature measurement and control system, source feed pressure supply system, high voltage power supplies, microparticle collector, and associated electronics necessary to operate the above. The commercially built vacuum system, the Varian 3118, shown in Figure 59, consists of a 10.8 cfm roughing pump, 6 inch oil diffusion pump, $LN_2$ cold trap, hot cathode ionization gauge and thermocouple gauges, manually operated vacuum valves, metal bell jar with electromechanical hoist, and electrical feedthroughs.

The current meters mentioned above will be used to measure various electric currents occurring during the powder generation, such as beam current, extractor current, etc. The meters will amplify the signals which range from 100 μA to 10 mA, so that they can either be read manually or by computer. These meters will reside in the Analog Bus (described later) as a signal module.

Source Temperature Measurement and Control System

In order to operate the source at the proper temperatures for a particular alloy material, a temperature measurement and control system has

been developed. Thermocouples are used to measure the temperatures of both nozzle and reservoir with their respective heaters individually controlled. Since the source can be operated up to 20 kV, the heater circuits must have appropriate electrical isolation. A functional block diagram of the source temperature measurement and control system is shown in Figure 60.

The thermocouple amplifier accepts a low level signal from a thermocouple, provides amplification, signal conditioning, isolation, and linearization. The high voltage isolation characteristics are obtained by frequency modulating the analog signal and transferring it across an air gap utilizing an infrared emitter and photodetector. An analog output voltage is provided that linearly represents the measured temperature. The calibrated output produces one millivolt per degree C measured. This signal is used as input to the controller which compares it to the desired setpoint temperature and regulates the power to the heater by means of a solid state relay. The amplitude of the voltage that powers the heater is controlled by an autotransformer. A 20 kV isolation transformer isolates the low voltage part of the system from the source. Referring to the block diagram of Figure 61, a general description of the amplifier follows.

The input signal obtained from the thermocouple floating at high voltage is applied to a stable, precision amplifier with a low temperature coefficient of offset drift. This amplifier (A1) amplifies the thermocouple signal to a level of approximately one millivolt per degree input. A $0^{o}C$ cold reference junction is included in the circuit that compensates for ambient temperature drift at the junction formed by the thermocouple wire connections to the amplifier input. The amplified analog signal is applied to the input of a voltage-to-frequency converter whose output is 6.667 Hz per millivolt (= $1^{o}C$) input. The frequency output of the V-to-F converter drives a current switch, Q1, that

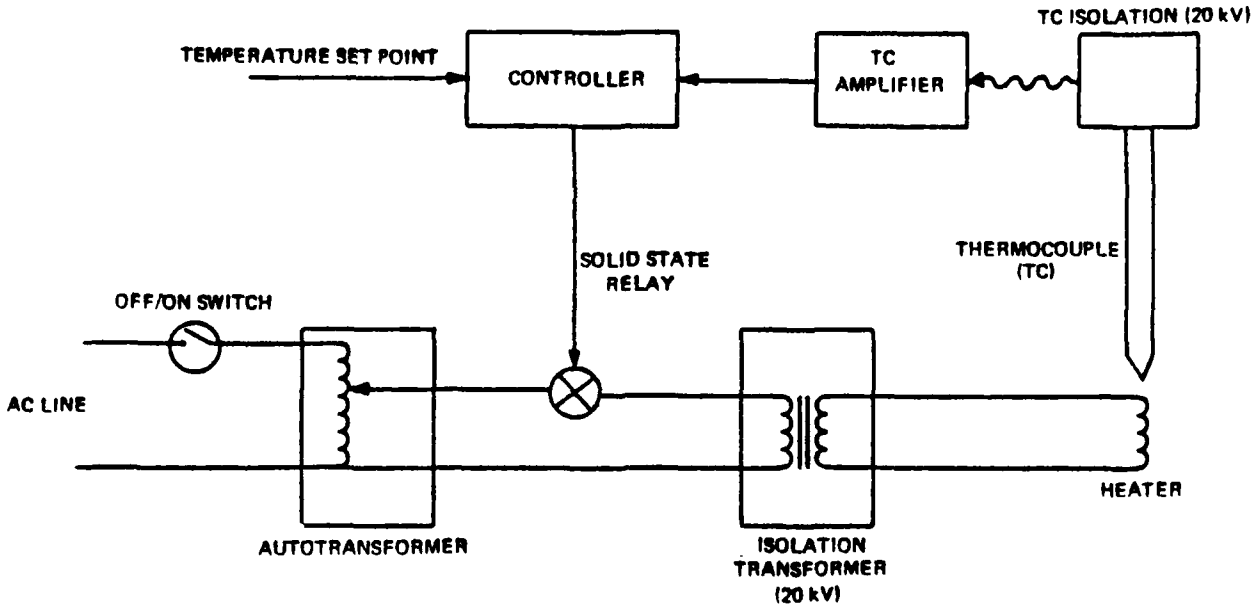


Figure 60. Temperature Measurement Control Functional Block Diagram

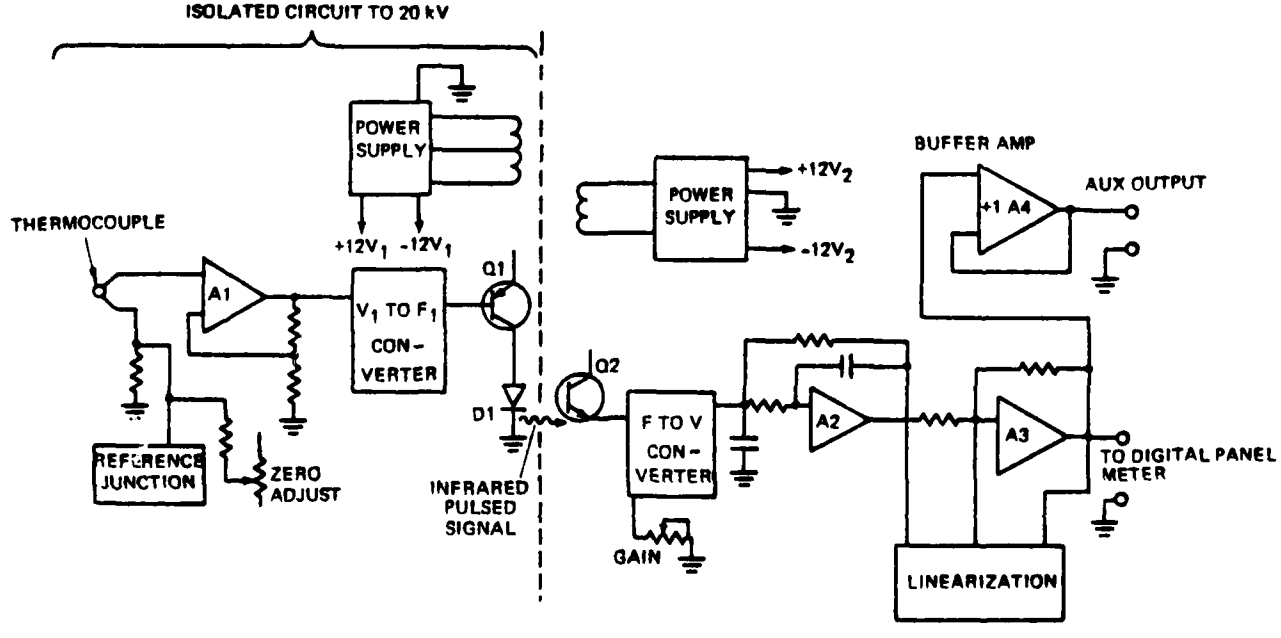


Figure 61. Isolated Thermocouple Amplifier Block Diagram

provides approximately 50 mA current pulses to the infrared emitting diode, D1. An input zero control is provided that removes all the offset voltages referred to the input of the amplifier, in addition to compensating for any offset in the V-to-F converter. (A scaling adjustment and output zero controls are provided in the output section of the amplifier.) Power is supplied to this isolated input section of the amplifier by a power transformer whose breakdown voltage is in excess of 20 kV. Regulated voltages are supplied by a dual plus and minus 12V regulator. The input section is totally isolated from power lines, earth ground, and the output section. It also has the capability to "float" to positive or negative potentials with respect to the output section or earth ground.

The frequency modulated pulses emitted by the infrared light emitting diode are sensed by a photodetector transistor, Q2, connected in tandem with a common base configuration of PNP transistor amplifier to maximize the system frequency response. The amplified pulses are applied to a frequency-to-voltage converter whose nominal output is one millivolt per 6.667 Hz input. An output of one millivolt from the F-to-V converter represents approximately $1^{\circ}C$ of the measured temperature. The current output pulses of the F-to-V converter are filtered by the two-pole filter comprised of A2 and its associated components.

Linearization for Types C and K thermocouples is accomplished at amplifier A3 and at the switchable linearization components utilizing a five segment approximation for the desired nonlinear curves. Gain and offset adjustments are made at amplifier A3 at each linearization break point. The linear output of A3 is one millivolt per $^{\circ}C$. Component A4 is a buffer amplifier with a gain of +1, providing an auxiliary output that may be used to drive a strip chart recorder. The full scale capabilities of the system (maximum accuracy) are $1350^{\circ}C$ for Type K, chromel/alumel, and $1650^{\circ}C$ for Type C, tungsten-5% rhenium/tungsten-26% rhenium, thermocouples.

The temperature controller operates in a time proportioning mode which regulates the controller's duty cycle (ratio of time on to the total time) by the deviation between the measured and setpoint temperature. The operation of the controller is described below with the aid of Figure 62. The dc level voltage of a triangle wave is proportioned to the measured temperature. An operational amplifier compares the triangle wave to the setpoint temperature voltage. This comparator instructs a solid state relay (SSR) to turn on the voltage to the heater whenever the triangle wave voltage falls below the setpoint. The SSR will start passing heater current on the next zero crossing of the 60 Hz ac voltage. When the triangle wave voltage is greater than the setpoint, the comparator signals the SSR to turn off heater power, which occurs when the 60 Hz current becomes zero.

The source heater controller tested under operating conditions has held the source temperature of 800°C stable to ±1°C, with rare excursions of ±2°C.

High Voltage Power Supplies

Commercially purchased Spellman high voltage power supplies are used to bias the source and extractor. These supplies allow for remote programming of the voltage from 0 to 20 kV, so that computer control can be implemented. The supplies are internally regulating to ±0.02% and, therefore, do not require external close loop control.

Power supplies for various biasing functions have been constructed. Power supply modules are located in the Analog Bus and supply voltages of up to 1500V dc.

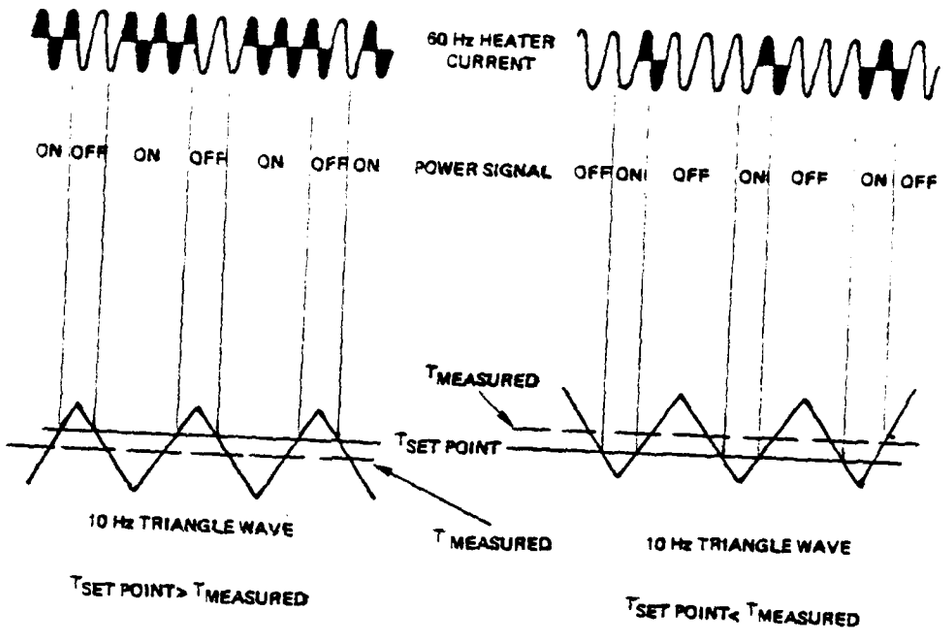


Figure 62. Operation of Heater Controller. The dark cycles of the 60 Hz heater current refer to current being passed by the SSR. The power signal refers to the signal sent by the comparator (see text).

Source Feed Pressure Supply System

The flow of molten material through the nozzle is controlled by both the high voltage and the feed pressure applied to the reservoir. At present, the feed pressure, manually controlled, is measured by a Baratron capacitive pressure gauge. An automation of the feed pressure control system is under development (subsection 4.1.2).

Particle Collectors

The microparticles generated are generally collected on Eastman Chemical TA401 Cellulos Triacetate Tape (replicating tape). The tape is soluble in acetone, allowing the removal of the particles from the tape for examination. At present, strips of tape are rigidly mounted to an electrically isolated copper disc which can be connected to ground or a current meter along with various metal collectors.

Analog Bus

The connection of analog signals throughout the Engineering Model is accomplished by means of an Analog Bus shown in Figure 63. Each electrical signal is wired to the same pin of each connector on the bus so that all signals are available to each electronic module. This allows for a more flexible system that is easily expanded as new modules are needed. The modules contain the circuits and components, discussed above, that were designed and fabricated in the Phrasor Scientific Laboratory specifically for the Engineering Model. These modules are the measurement and control systems needed for the operation of a Tabletop Powder Generator. The Analog Bus is so configured that one or two connectors will interface it for control and data acquisition by the computer. The modules observed in Figure 63 are:

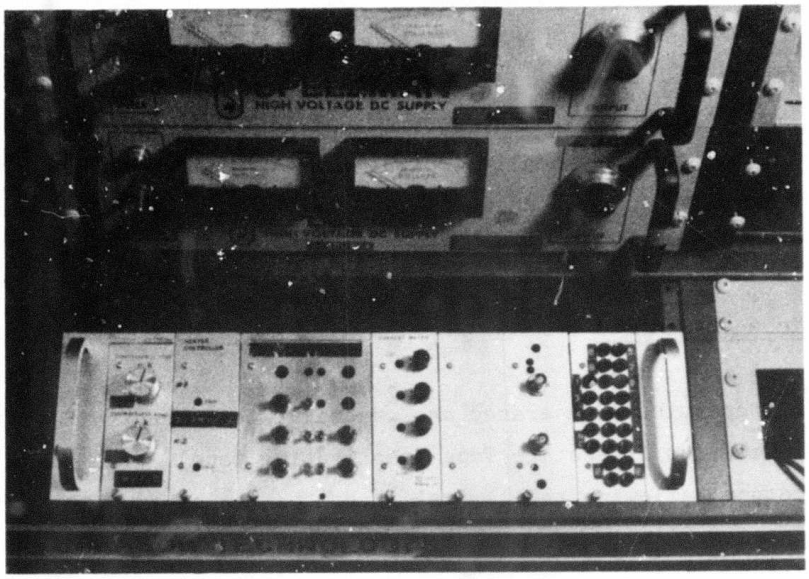


Figure 63. Analog Bus Composed of Several Modules in a Card Cage

- Temperature Gauge (low voltage circuits)
- Heater Controllers
- Interface and Manual Control Module
- Current Meters
- 1.5 kV Power Supplies
- External Bus Line Interface

The bus allows for manual (i.e., noncomputer) setting of input voltages for control of source temperature, nozzle voltage, and measurement of operating parameters.

### 4.1.2 PLANNED MODIFICATIONS TO THE ENGINEERING MODEL

The basic control philosophy adopted on the Engineering Model has been to allow the fundamental control parameters of the EHD process (high voltage, temperature, and feed pressure) to be set by the computer after measurement of the microparticle beam characteristics. The regulation of the parameter, however, will be under close loop control of dedicated hardware controllers. As described in subsection 4.1.1, much of the work on the controller is complete. Below we will discuss planned modifications to some of the systems. Figure 64 is an illustration of the projected complete Engineering Model.

#### Source Temperature Control

In subsection 4.1.1, the temperature controller was described. The amplitude of the heater voltage has been set by an autotransformer (Figure 60). In order that the system be controllable by a computer, this autotransformer will be replaced by a constant ratio transformer with three output taps. The necessary tap for a specific temperature will be either manual or computer selectable. The manual switch, as well as interfacing to the computer, will be accomplished through a digital bus which will be discussed below.

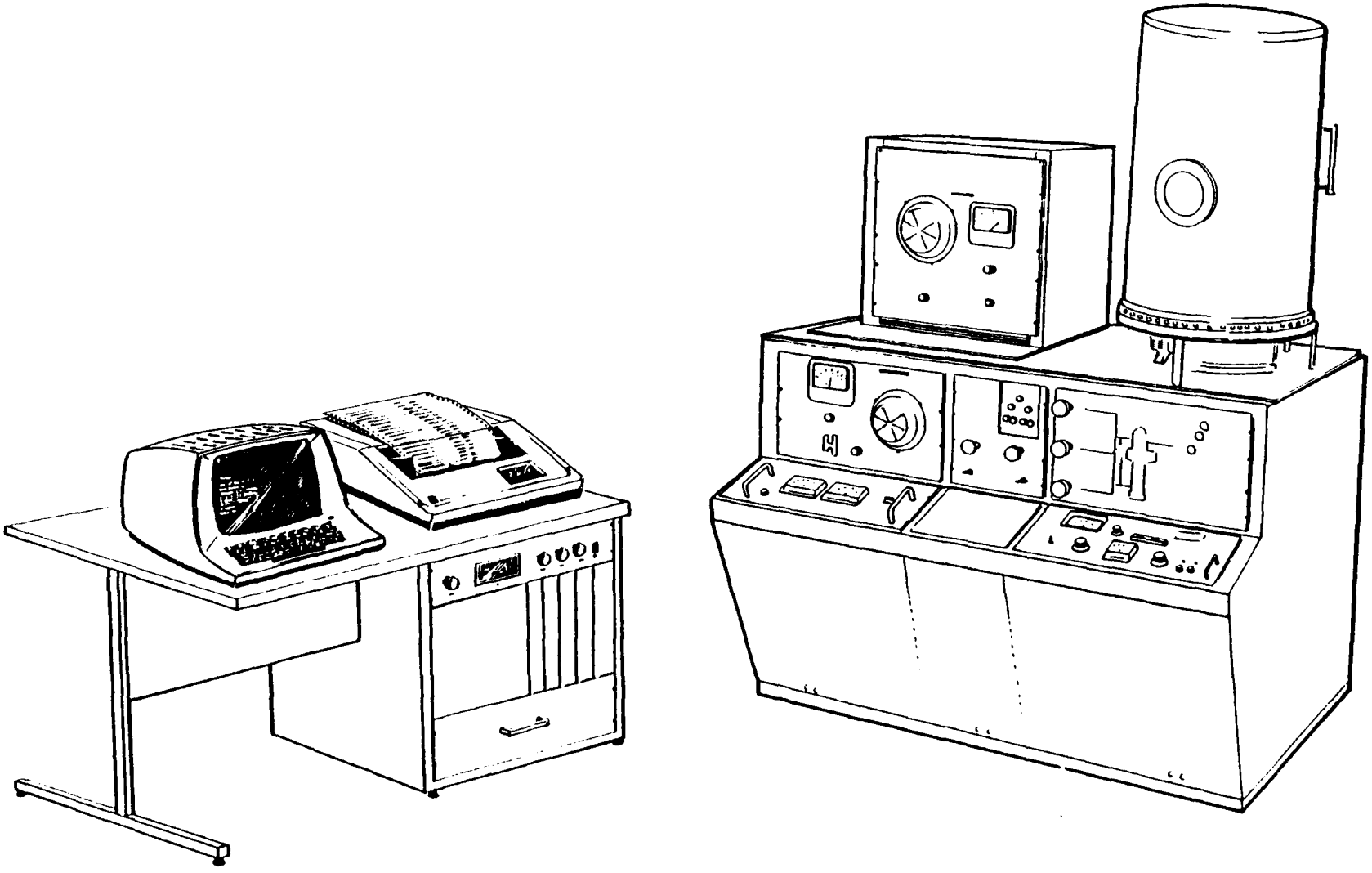

Figure 64. Engineering Model with Computer Control and Readout System

## Source Feed Pressure Supply System

The feed pressure control system will be automated. A block diagram of the proposed system is shown in Figure 65. The controller and pressure gauge are a commercial MKS Baratron Pressure/Flow Controller and Baratron capacitive pressure gauge, respectively. The electrical control valve is operated by the controller, while the needle valve will be manually operated. Eventually, it will be electrically controlled by the computer. The shutoff valves are used to isolate the system for safety and cleanliness.

For a set pressure, the needle valve will allow a small leak from the reservoir to the vacuum pump. If pressure variations occur, the controller will compensate by regulating the control valve. If the pressure is to be increased, the needle valve setting remains unchanged and the control valve will be set to allow greater gas flow. If the pressure is to be decreased, both needle and control valves will be reset. The exact algorithm will be determined during development of the system.

## Computer System

A microcomputer system has been purchased and is scheduled for delivery soon. Initially, the computer system will be used as a data acquisition system (DAS) without any control responsibilities. Once the probe requirements and physical relationships between particle beam characteristics and control parameters are well established, the computer will be given more control responsibility. This will continue until the Engineering Model is under complete computer control, at which time the knowledge obtained during development of the Engineering Model will be incorporated into the Production Prototype.

The purchased computer is based on a DEC LSI 11/2 CPU with 32K-16 bit words of RAM and two double density floppy diskette drives, video

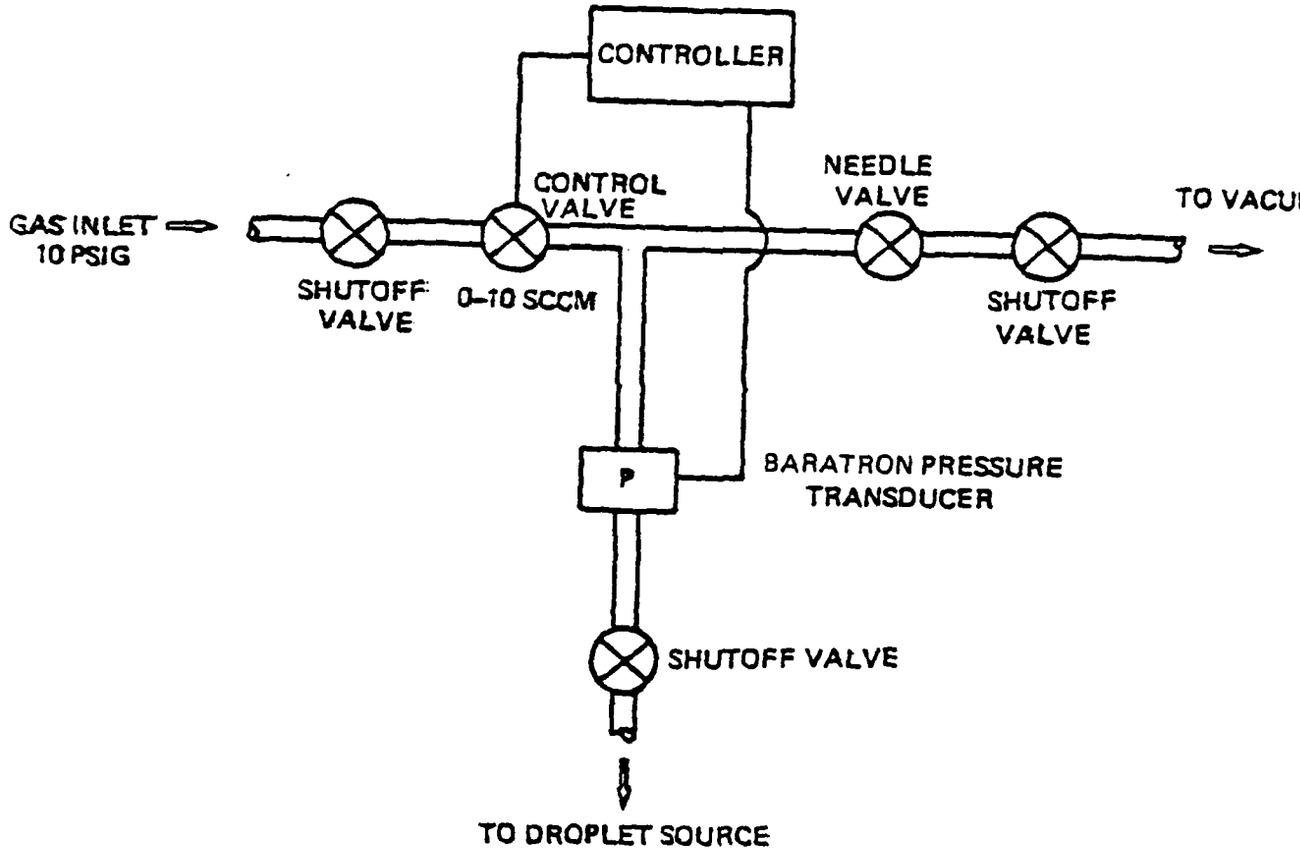


Figure 65. Schematic Diagram of Feed Pressure Control System

terminal with graphics capability, 32 channels of analog input, 8 channels of analog output, 64 channels of digital input and output, and a graphics printer. The hardware has been purchased from a "turnkey" computer company, which will allow rapid integration of the computer system into the Engineering Model. This very flexible system should allow rapid progress in the development of the Engineering Model toward the goal of manufacturing the Production Prototype. It is believed that a less flexible and extensive computer system will be needed for the Production Prototype; however, most of the software should be transferable.

Digital Bus

The same reasons given in subsection 4.1.1 for implementing the analog bus are valid for implementing a digital bus that will be used to interface digital signals from the computer to the Engineering Model. Digital signals will be used to choose taps on the transformers in the source temperature controller, open and close vacuum valves, determine various switch closings which monitor operation of the system, and operate other relays. The modules for the digital bus will be designed to allow either manual or computer control.

Microparticle Collection

As described in subsection 4.1.1, the microparticles will be collected on cellulose triacetate film tape. To allow extended operation and to collect a variety of powders produced under different operating conditions, a tape transport system is being designed. The tape transport system will alow the movement of the tape past a collection aperture at a speed of the order of 2 cm/minute on a take-up reel. Another reel will feed tape to cover the deposited powder. At the completion of the run, the tape-powder-tape combination is removed from the system and will be well correlated with the operating data and conditions during which the powders were generated.

Probes

Several diagnostic probes have been examined and evaluated for use in the Engineering Model. Some of these were discussed in subsection 2.5.2. The beam current was found to be an unsatisfactory method for determining mass flowrate, because of the alteration of charge on droplets, and this precluded the use of time-of-flight techniques for the measurement of particle sizes and distribution. An alternate technique being tested at the present time is discussed in subsection 2.5.2.

## 4.2 PRODUCTION PROTOTYPE

The projected end result of this program is the manufacture of a compact laboratory type microparticle generator for material research. It should be easily operated by those with no training in electrohydrodynamics, require minimal operator involvement in the choosing of operating parameters, yet be flexible enough to generate powders of various compositions. Since it is to be a laboratory unit, it should be compact and should not have any special power or location requirements. As with any other laboratory equipment, it should be self diagnostic for ease of maintenance and repair.

### 4.2.1 DESIGN PHILOSOPHY

The basic design procedure will be to develop and test these systems on the very flexible and complex Engineering Model, after with they will be incorporated into the Production Prototype. This will allow for the elimination of redundant modules, the reliability testing of the major assemblies, and a reduction in cost of the complete system. A dedicated microcomputer will handle operator-to-system interfacing, supervise all close-loop hardware controllers (feed pressure, source temperature, high voltage) and probe inputs, test for safety, and operate self-diagnostic functions.

Of critical importance are ease of operation, maintenance, and repair. A complete documentation package will be supplied with each particle generator. This will include principles of operation, operating instructions, required drawings and diagrams, and lists of major assemblies and their manuals. The computer self-diagnostic capability will allow rapid isolation of problem areas, and the modularity of the major assemblies will allow rapid replacement of any malfunctioning module.

The above is the design philosophy adopted at the present time. As the Engineering Model is developed, it is expected that better approaches will be forthcoming. Two production prototype units are scheduled for delivery, and any needed changes discovered from actual use of the first laboratory model will be incorporated in the second one.

### 4.2.2 SYSTEM DESCRIPTION

The preliminary design of the Production Prototype contains the following major assemblies: vacuum pumps, gauges and chamber; feed pressure gas handling and control system; source powder collection system, shutters and baffles; high voltage power supplies; microcomputer, displays, and interfacing electronics; heater power and control electronics; and operating software. The system will be housed in an enclosure that is expected to be less than 8 feet high above the floor, about 6 feet wide, and 4 feet deep. Water will be required for diffusion pump cooling, and the projected electrical power requirements are 230V ac at 25A for the vacuum system and 2 lines of 120V ac at 15A each.

The preliminary specifications for the powders generated include cooling rates of up to $10^8$K/s. The powders range in size from less than 0.01 μm to over 100 μm. The reservoir capacity is presently designed to produce approximately 20 gm of fine powders using test alloys with melting points up to 1850K that are compatible with the materials used in the source.

A possible operating sequence would be the following: The system power is applied, automatically loading the operating software into the computer. Once the vacuum pumps are at operating temperature, the operator will instruct the system to enter either an automatic or manual mode of operation. In the automatic mode, the operator answers a series of questions prompted by the computer, loads the source material in a reservoir, and loads the reservoir into the source. The feed pressure line will then be connected to the source. The operator also loads the particle collector with appropriate substrates, secures the vacuum chamber, and indicates that the system is ready. The computer automatically proceeds with the supervision of the generation of powders, determining operating parameters from the answers to the prompted questions and input signals from probes. Upon completion of the run, the computer displays a completion signal and the operator unloads the collected powder after the vacuum chamber is vented. In order to produce powders of unusual materials, the manual mode allows the operator to monitor and control operating parameters directly but with computer assistance.

### 4.2.3 OPTIONAL SYSTEMS

The description given above for the Production Prototype is only one possible configuration for a commercial powder generator based on EHD principles. For special applications, the specifications for temperature, voltage, and size can be modified. It is also possible to exceed the specified operating temperature by employing special source materials and heaters other than those discussed in this report. Voltages higher than 20 kV may be required for special applications, and throughputs greater than 20 gm in a couple of couple of hours could be generated using modified components. During the development of both the Engineering and Production Prototype Models, the extension of the nominal specifications will be studied to develop a set of options that may be desired in the dynamic area of materials research.

## SECTION 5

## CONCLUSIONS

In May 1977, the ARPA initiated a program with Phrasor Scientific, Inc., to (1) develop the method of high temperature electrohydrodynamics, (2) apply this technology to rapid solidification and other materials oriented areas, and (3) produce a unique laboratory instrument capable of producing micron and submicron particles of various alloy systems. Before the initiation of this contract, no information existed in the technical literature to draw upon the experience of previous data bases or state-of-the-art development of high temperature EHD. This program has succeeded in introducing into Materials Science a unique material processing and research tool based on advances made in the understanding and construction of molten metal EHD devices during the past few years. The integration of these two very distinct and separate technologies, EHD and Materials Science, has stimulated an interest in this program by various government laboratories, private industry, and universities. The nature of these outside inquiries (foreign and domestic) cover such diverse applications as rapid solidification, nucleation studies, magnetic properties of fine powders, powders composed of refractory metal and ceramic materials, rare earth and precious metal applications, copper powders for dispersion in inks used with hybrid circuits, and others.

As with many new technology developments (and this program is no exception), the transfer of new concepts to other fields has been rewarding. The capability of the EHD process to deposit thin films and coatings is presently being exploited in a process that could produce low-cost polycrystalline silicon sheet for solar photovoltaic applications. A new technology is now being explored for the purification of thin

metallic foils and thin sheets comprised of semiconducting materials such as silicon and germanium. Perhaps a lower cost method of producing detector grade silicon will emerge from this purification process.

A listing of the major results obtained on the program is provided in the Introduction to this report. Along with the reported success in demonstrating the capability of producing rapidly solidified materials and other novel structures, any program of this type will also raise new questions. The program is continuing the investigation of these and, in the process, developing the integrated technology necessary for the design and construction of a Tabletop Powder Generator. Among the questions raised on this program is the in-situ determination of average cooling rates. Although cooling rates are not directly measurable at present, they can, of course, be determined by a post-examination of the particles produced in the process. Nevertheless, we have made several contributions toward solving the in-situ measurement problem as discussed in this report. We have also identified a problem related to high surface tension alloy systems which results in a low yield of micro-size particles.

To facilitate the research needed to resolve the above questions and to design the modules necessary for a successful Tabletop Powder Generator, automation and modern computer techniques have been introduced into the design of the Engineering Model. The Engineering Model will serve as an automated data acquisition system, allowing concentration on the problems associated with the integration of EHD and material science. As circuits and systems are developed for the Powder Generator, they will be tested on the Engineering Model. We conclude that great progress has been made in integrating these distinct technologies and in resolving the fundamental questions raised above. As the program continues, the integrated technology will allow for the design and construction of the successful Tabletop Powder Generator.

REFERENCES


1. C. G. Levi and R. Mehrabian, "Heat Flow in Atomized Metal Droplets," submitted for publication in Metall. Trans.

2. J. Perel, J. F. Mahoney, B. E. Kalensher, K. E. Vickers, and R. Mehrabian, Rapid Solidification Processing; Principles and Technologies, edited by R. Mehrabian, B. H. Kear, M. Cohen (Claitor's Publishing Division, Baton Rouge, Louisiana, 1978) p. 258.

3. J. Perel, J. F. Mahoney, B. E. Kalensher, and R. Mehrabian, "Electrohydrodynamic Techniques in Metal Processing," Twenty-fifth Sagamore Army Materials Conference on: Recent Advances in Metal Processing, Bolton Landing, New York (17-21 July 1978).

4. J. Mahoney, et al, "Development of a Tabletop Model for the Generation of Amorphous/Microcrystalline Metal Powders," Interim Report, April 1978, ONR N00014-77-C-0373, Phrasor Scientific, Inc.

5. R. Gomer, Field Emission and Field Ionization, (Harvard University Press, 1961.)

6. C. D. Hendricks, R. S. Carson, J. J. Hogan, and J. M. Schneider, "Photomicrography of Electrically Sprayed Heavy Particles," AIAA J., V. 2, p. 733 (April 1964).

7. J. A. Champion, B. J. Keene, J. M. Sillwood, "Wetting of Aluminum Oxide by Molten Aluminum and Other Metals," J. Mat. Sci., V. 4, p. 39 (1969).

8. N. R. Lindblad and J. M. Schneider, "Production of Uniform-sized Liquid Droplets," J. Sci. Instr., V. 42, p. 635 (August 1965).

9. J. Mahoney, A. T. Forrester, J. Perel, and B. Kalensher, "Electron Capture in Charged Microdroplet Beams," IEEE/IAS 1980 Annual Meeting; Electrostatic Spraying of Liquids Session, Cincinnati, Ohio (28 September 1980).

10. S. Dushman, "Scientific Foundations of Vacuum Techniques," (John Wiley & Sons, 1962), p. 390.

11. Private communication from C. Levi from Doctoral Thesis, University of Illinois, Urbana, Illinois.

12. J. J. Thomson, Cambridge Phil. Proc., 15, 64 (1908).

13. L. P. Smith, Phys, Rev., 35, 381 (1930).

14. J. B. Taylor and I. Langmuir, Phys. Rev., 44, 423 (1933).

15. L. N. Dobrezow, Physik. Z. Sowjetunion, 11, 647 (1937).

16. J. R. Hiskes and A. Kaor, Proc. of the Symp. in Production and Naturalization of Negative Hydrogen Ions and Beams, September 26-30, 1977, Brookhaven National Laboratory. BNL 50727, UC-349 Physics-Atomic and Molecular TID-4500.

17. J. P. Blewett and E. J. Jones, Phys. Rev., 50, 464 (1936).

18. R. G. Hills and P. Gibbs, J. of Appl. Phys., 37, 2075 (1966).

19. J. Perel, J. F. Mahoney, P. Duwez, B. E. Kalensher, and R. Mehrabian, "Application of Electrohydrodynamics to Rapid Solidification of Fine Atomized Droplets and Splats," Second International Conference on Rapid Solidification Processing Principles and Technologies, Reston (March 1980).

APPENDIX A

# ELECTRON CAPTURE IN CHARGED MICRODROPLET BEAMS

BY

J. MAHONEY, A. T. FORRESTER, J. PEREL AND B. KALENSHER

PAPER PRESENTED AT:

IEEE/IAS 1980 ANNUAL MEETING
SESSION 2: ELECTROSTATIC SPRAYING OF LIQUIDS

SEPTEMBER 28 - OCTOBER 2, 1980

STOUFFER'S CINCINNATI TOWERS, CINCINNATI, OHIO

**Phrasor Scientific, Inc.**

1536 HIGHLAND AVENUE
DUARTE, CALIFORNIA 91010
(213) 357-3201

# ELECTRON CAPTURE IN CHARGED MICRODROPLET BEAMS*

J. Mahoney, A. T. Forrester, [a] J. Perel, and B. Kalensher

Phrasor Scientific, Incorporated, Duarte, California 91010

Directed beams of positively charged, micro-size droplets formed by electrostatic spraying are observed to undergo post-acceleration alteration of their initial charge state. The effect is attributed to the capture of electrons existent in beams. Neutralization times are predicted to vary inversely with the droplet size and electron density. Experimental evidence, including measurements of electron densities and temperatures, is provided to support the proposed model for negative charge accumulation on positively charged droplets. Possible mechanisms for electron production and implications of negative charging on conventional beam diagnostics are discussed.

## I. INTRODUCTION

Beams of charged droplets are generated by applying an intense electric field of positive polarity to the tip of a fine capillary containing a liquid or molten material. Such beams have been studied as a possible basis for electric propulsion.[1] In our laboratory, we are using molten droplets generated at high temperatures to study the properties of amorphous, crystalline, and other novel structures produced by the rapid cooling of microspheres composed of aluminum alloys, iron-nickel alloys, and many other materials.[2]

While making measurements on beams of charged droplets to determine such important parameters as the spread in charge-to-mass ratios, we encountered effects that suggest alteration in the charges on the droplets, especially from observations that many droplets were found to be negative although generated from a nozzle maintained at a positive potential. It became necessary to consider that positively charged beam droplets were absorbing electrons that are released in our vacuum system when the particle beam is present.

Recently Anestos and Hendricks[3] have studied the charge acquired by microscopic particles injected into a plasma as a diagnostic technique to determine plasma parameters. The particle source in their experiments consisted of a uniform stream of neutral droplets generated by the electromechanical breakup of a liquid jet. The particles were then ejected into an argon plasma formed inside a coaxial cylindrical system. Their results showed that the charge acquired by particles passing through a plasma is directly dependent on the electron temperature. Prior to this work, Rosen[4] in 1962 reported on a method for reducing the free-electron concentration in a gas plasma based on absorption of electrons by uniformly distributed micro-size dust particles. Other workers have also investigated the trapping of electrons by micro-size particles in space[5] in flames[6], and in rocket exhausts[7].

The work described herein is directed toward an understanding of the interaction of electrons with directed beams of positively charged, conducting droplets. The beam particles, generated by electrohydrodynamic methods, can range in diameter from less than 0.1μ to 100μ. It will be shown that application of Langmuir probe theory to spherical beam particles predicts that the time required to discharge particles is inversely proportional to the droplet radii and electron density. The mechanism for electron production in our test chamber is not well understood at present. However, it is known that electron concentrations are initiated and sustained by operation of the charged particle beam. Possible sources of electrons are discussed in a later section.

## II. DROPLET NEUTRALIZATION BY ELECTRON CAPTURE

Among the previous investigators of electron capture by small particles, only Anestos and Hendricks applied spherical Langmuir probe theory to determine the charging characteristics of droplets. We are in complete agreement with this approach. The typical droplet velocity in our investigations is quite slow compared to electron speeds, and the droplets can be considered to be at rest in the electron gas. As such, they are ideal probes, and the electron current arriving at the droplets is a fraction of the current reaching the Debye sphere. A portion of the electrons orbit the droplets and pass out of the region of influence of the droplet fields. The affinity of positively charged droplets for electron capture is not surprising since some beam droplets can initially acquire potentials of several hundred

* Sponsored by Advanced Research Projects Agency and monitored by Office of Naval Research under Contract No. N00014-77-C-0373.

a) Present address: University of California at Los Angeles

volts or more during their formation stages.

For the range of droplet sizes encountered in our studies, the sheath radius is large compared to the particle radius and, according to I. Langmuir[3], the probe current for accelerating potentials is given by

$$i = \pi r^2 nev \left(1 + \frac{eV}{kT}\right) \qquad (1)$$

where r is the particle radius, n is the electron density, e is the electron charge, $v = (8kT/\pi m)^{1/2}$ is the average velocity of the electrons from kinetic theory, V is the droplet potential, k is the Boltzmann constant and T is the electron temperature. By letting $i = (-dq/dt)$ and the droplet surface potential $V = q/4\pi\varepsilon_o r$, equation (1) can be solved for the time required to neutralize the original charge on the droplet, $\tau_n$. The boundary conditions are that, at time $t = 0$, $q = Q$, the initial or undisturbed charge on the droplets at formation, and at $t = \tau_n$, $q = 0$. The time required to completely neutralize a positively charged droplet by electron capture is then given by

$$\tau_n = \frac{4\varepsilon_o}{\pi nev}\left(\frac{kT}{e}\right) \ln\left[1 + \left(\frac{e}{kT}\right)\frac{Q}{4\pi\varepsilon_o r}\right] \quad . \qquad (2)$$

Since $\tau_n$ is a weak function of the droplet potential, neutralization times are found to be inversely proportional to droplet radii and electron density. Thus, larger beam particles will discharge more rapidly than smaller beam particles for a given electron density.

For certain applications or beam measurements, it may be of interest to note how neutralization distances compare to typical dimensions of laboratory experimental apparatus. The distance required to neutralize positive droplets is given by

$$d_n = \tau_n \left(2\frac{Q}{m} V_a\right)^{1/2} \qquad (3)$$

where Q/m is the charge-to-mass ratio of the droplets at formation and $V_a$ is the potential through which the droplets are accelerated. For simplicity it is assumed that the beam droplets do not accumulate negative charge during their acceleration phase. If the initial charge on the droplets diminishes during this period, the droplet velocity, $v_p = (2QV_a/m)^{1/2}$, will be affected accordingly. Neutralization distances would then be correspondingly smaller than those predicted by Eq. (3). In the next section, data based on experimental determinations of electron densities and temperatures is used to calculate neutralization times for a range of droplet sizes. The results indicate that for typical values of n and T measured in our apparatus, particles greater than 0.5μ will neutralize in distances that are short compared to the distances traversed before collection (~0.3m)

For distances traversed greater than the neutralization distance, the droplets will begin to accumulate negative charges. For spherical probes with retarding potentials (negatively charged), Langmuir states that the probe current is governed by the relation

$$i = \pi r^2 nev \exp(eV/kT) \qquad V < 0 \qquad (4)$$

where V is the droplet potential given by $V = q/4\pi\varepsilon_o r$. In the absence of a random ion current density, electrons will continue to arrive at droplets until the droplet surface potential reaches the value $V' = -(kT/e)$. Electrons in the velocity distribution with energies equal to or less than kT will not have sufficient energy to carry them to the droplet. The time $\tau_e$ required after neutralization to charge the droplets to the potential V' can be determined from Eq. (4) for the boundary conditions: at $t = 0$, $q = 0$ and at $t = \tau_e$, $q = -(kT/e)4\pi\varepsilon_o r$. The result is

$$\tau_e = \frac{6.87\varepsilon_o}{nevr}\left(kT/e\right) \quad . \qquad (5)$$

Similar to the discharging characteristics, times required to negatively charge droplets are inversely proportional to the electron density and particle size. Negative charging times are plotted in the next section for measured values of n and kT/e.

## III. MEASUREMENT OF ELECTRON DENSITY AND TEMPERATURE IN CHARGED PARTICLE BEAM

The experimental arrangement used to measure the electron density and temperatures in a charged microdroplet beam is illustrated in Fig. 1. A

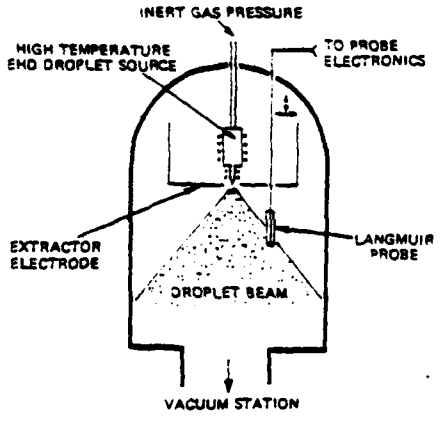


Fig.1 EHD Spray Apparatus With Langmuir Probe Measurement

high temperature electrohydrodynamic (EHD) droplet source was used for these experiments. The source consisted of a cylindrical alumina ceramic reservoir and nozzle heated by a coaxial, resistive oven. Molten aluminum is delivered to the ceramic ($Al_2O_3$) nozzle tip by pressurizing the reservoir with argon gas. An aluminum microparticle beam is established when the molten material reaches the capillary orifice. A potential of 8 - 10kV applied to the material in the nozzle provides the high fields required for electrostatic dispersion.

A circular plane Langmuir probe was installed in the test chamber as shown in Fig. 1 to obtain the current-voltage characteristics from which the electron temperatures and densities are deduced. The probe was enclosed by a shield to prevent droplets from depositing on the surface of the probe. In order to measure the electron density and temperature at various locations in the chamber, the probe assembly was traversed axially and radially. An X-Y recorder was used to plot the current-voltage characteristics of the probe. Typical results of the measurements yield values for the electron density of $n = 10^{13} m^{-3}$ and electron temperatures of $T = 5.62 \times 10^5$ °K ($kT/e$ = 48.4 volts). Measured values of n and T depend on the operating conditions of the microparticle source e.g. source current and voltage. Variations in n and T are also seen as a function of probe position in the test chamber. The values measured for the electron temperatures were higher than expected. This observation is attributed to low energy electrons which have gained energy from the influence of positive droplet fields.

The above measured values of n and T were inserted into Eq. (2) to calculate neutralization times predicted by the model. For these calculations, values of Q as a function of droplet radius were computed using the basic Rayleigh formulation for the maximum allowable charge on conducting liquid droplets. The final value of Q was assumed to be a factor of two below the maximum allowable charge. It seems appropriate to suppose that charged droplets formed by high field extraction from a capillary nozzle will not be far below the Rayleigh criterion.[9] For aluminum droplets, the charge will have a value given by

$$Q = 4\pi(\varepsilon_o \gamma)^{\frac{1}{2}} r^{3/2} \qquad (6)$$

where $\gamma$ is the surface tension. Neutralization times and distances are shown in Fig. 2 as a function of particle diameter for droplets generated at 10kV. For electron densities and temperatures described above, droplets, say in the range 5u to 100u, will completely discharge in less than 100 microseconds. This corresponds to flight paths of less than $10^{-3}$ meters for particles initially accelerated through a potential of 10kV.

Fig. 3 graphically depicts the negative charging times computed from Eq. (5) as a function of particle size to reach a potential of $V = -(kT/e)$ for positive droplets which have undergone neutralization by electron capture. Just as for neutralization times, the negative charging time for large droplets is less than those for smaller particles. Note that for particles in the range

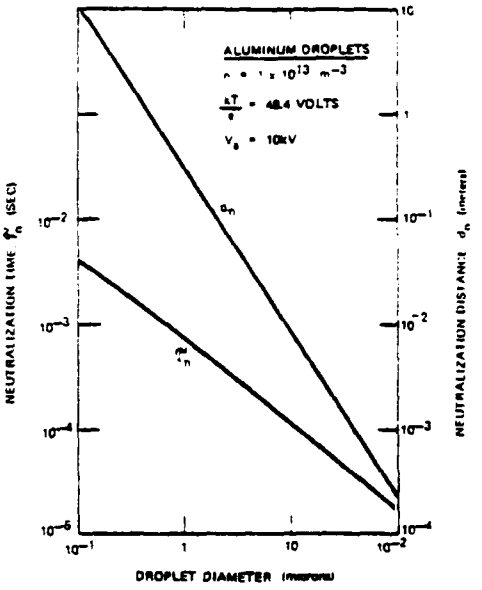


Fig.2 Neutralization Parameters Versus Droplet Size

10 to 100 micron in diameter, negative charging times less than 60 microseconds are involved. The additional distances traversed by these particles from their neutralization sites, also shown in

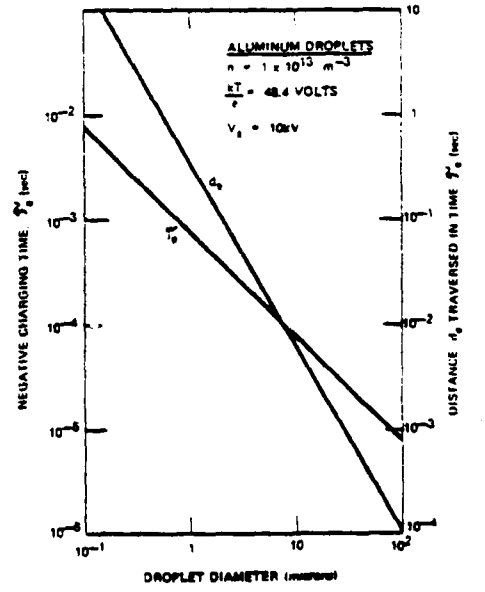


Fig.3 Negative Charging Parameters Versus Droplet Size

Fig. 3, amounts to less than $6 \times 10^{-3}$ meters. The distances were computed from $d_e = v_D \tau_e$. Thus for a wide range of microparticle sizes, charge reversal can occur over small distances compared with typical dimensions of most laboratory apparatus.

Experimental evidence to support the model predictions that charge reversal will occur in directed beams of positive droplets was obtained from a simple particle deflection experiment. The experiment consisted of placing a pair of deflection plates below a plate containing a rectangular slit, shown in Fig. 4. The slotted plate was

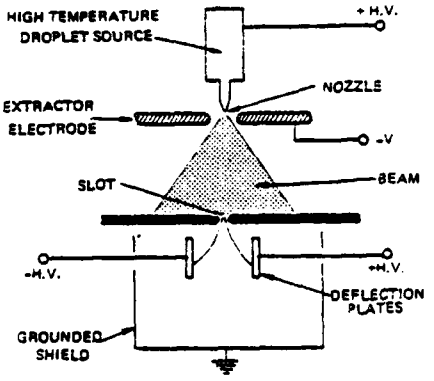


Fig.4 Droplet Deflection Experiment

located .05m from the source of positive droplet emission. Choice of slit dimension was made to ensure the passage of the largest droplets expected in the beam. Deflection potentials were selected to permit the collection of positive and negative particles on the plates as they passed through the slit. Examination of the collected particles on the negative and positive plates for a 10kV generated beam showed conclusively that negative particles were formed in the region between the source and the slotted plate. The higher density of particle deposits observed on the deflection plate held at positive potential is evidence that a significant portion of the positive beam droplets became negatively charged after traversing a distance of approximately .05m from the source.

## IV. POSSIBLE SOURCES OF ELECTRONS

Quantitative information is lacking on the mechanisms responsible for the electrons detected during the electrohydrodynamic generation of charged particle beams. Several competing processes may be involved and brief mention will be made here of what is currently thought as the most probable electron sources operative. Generation of droplet beams are often accompanied by ions formed during the electrostatic spraying process. These primary beam ions could easily release secondary electrons upon impact with surfaces or electrodes.

SEM analysis of particle depositions on various substrates reveal the presence of submicron droplets, many with diameters less than 0.1u. For typical acceleration potentials applied in our experiments, particles of these dimensions will reach velocities in excess of 1 km/sec. Plasmas, formed by the energetic collisions of these hypervelocity particles with surfaces, could contribute to the electrons measured in our droplet beams.[10] For the velocity ranges under consideration, these plasmas generally consist of ionized droplet materials.

Collisions of primary beam ions with slower moving droplets may eject electrons, provided that the surface potentials of the droplets do not prohibit the electrons from escaping.

Electrons liberated by any of these possible mechanisms can generate additional electrons created by ionizing collisions with neutral gas atoms or molecules in the chamber. The 50 volt electrons measured in our apparatus correspond to the near maximum in the ionization cross-sections for collisions of this type. This effect can be estimated by computing the number of ion pairs/$cm^3$-sec, $S = n_a n \sigma_i v$ produced by these collisions. Here $n_a$ is the atom density, n the electron density, $\sigma_i$ is the ionization cross-section and v is the electron velocity. For $n_a = 10^{22}/cm^3$ (corresponding to a background pressure of $\simeq 2.8 \times 10^{-5}$ torr), $n = 10^7/cm^3$, $\sigma_i = 10^{-16} cm^2$ and $v = 4.7 \times 10^8 cm/sec$, the result is $4.7 \times 10^{11}$ ions/$cm^3$-sec produced. For a 15cm radius sphere (approximate dimensions of our apparatus), this yields a flow of electron current of about 1 mA.

No data has been found in the literature for secondary electron yields involving micro-size charged droplets impacting with solid surfaces. Some data exists[11] for metal cluster ions of the type $M_n^+$ for values of n up to and including n=6. If ions can be formed in the EHD process, it is conceivable that charged clusters composed of a small number of individual atoms are also present in the distribution. These cluster species might be expected to produce secondary electrons by the kinetic emission process described by Kaminsky.[12] As the size and number of atoms comprising the charged droplets increases in the distribution, the eV/atom becomes very small. The equivalent ion velocity is small also and below the threshold velocity for kinetic emission of secondary electrons. A potential emission process may be effective for secondary yields as the bombarding particle size increases.

The phenomena of secondary electron emission for micro-size particles and the characteristics

of emission over the entire droplet distribution is undoubtedly very complex. Experiments designed to measure the emission processes for positive, negative and neutral droplets would certainly contribute some interesting data to this area of particle physics.

## V. CONCLUSION

A model for describing electron capture by positively charged droplets in a directed beam has been presented. The basic predictions of the model have been verified by the detection of negative droplets. Measurements of the electron densities and temperatures in EHD beams are of sufficient magnitude to account for the negative charging of droplets observed by various methods. The implication of charge alteration in beam droplets poses some challenging questions for conventional beam diagnostics and control. Several diagnostic techniques applied to charged droplet beams rely on an invariant particle charge as an important parameter. The possible errors introduced into these measurements should be examined whenever an electron source exists for discharging or altering the droplet charge. For example, the errors associated with measurements of charge-to-mass ratios would be expected to increase with increasing droplet size. Ultimately we hope to gain sufficient insight into the electron production and absorption processes in order to implement suitable beam diagnostic measurements. In some instances, one may have no alternative but to seek measurement parameters other than droplet charge to characterize beam behavior.

## REFERENCES


1. V. E. Krohn, Jr., Progress in Astronautics and Rocketry, Vol. 5, Electrostatic Propulsion (Academic Press, New York, 1961), p. 73.
2. J. Perel, J.F. Mahoney, B. E. Kalensher, K. Vickers, and R. Mehrabian, "Rapid Solidification Processing Principles and Technologies" (Claitor's Publishing Division, Baton Rouge, 1978), p. 258.
3. T. C. Anestos and C. D. Hendricks, J. Appl. Phys. 45, 1176 (1974).
4. G. Rosen, Phys. Fluids 5, 737 (1962).
5. M. S. Sodha, Brit. J. Appl. Phys. 14, 172 (1963).
6. C. C. Johnson and C. K. Bullock, J. Appl. Phys. 35, 2804 (1964).
7. S. L. Soo, J. Appl. Phys. 34, 1689 (1963).
8. I. Langmuir and H. M. Mott-Smith, Phys. Rev. 28, 727 (1926).
9. R. J. Pfeifer and C. H. Hendricks, Phys. Fluids 10, 2149 (1967).
10. D. Smith and N. G. Adams, J. Phys. D: Appl. Phys. 6, 700 (1973).
11. G. Standenmair, W. O. Hofer and H. Liebl, Int. J. Mass Spectrom. Ion Phys. 11, 103 (1976)
12. M. Kaminsky, Atomic and Ionic Impact Phenomena on Metal Surfaces (Academic Press, New York, 1965).